Doctoral Thesis

Development and Evaluation of a Control Unit for the Coupled Dark State Magnetometer

DI Andreas Pollinger

Graz University of Technology
Institute of Microwave and Photonic Engineering

in cooperation with

Space Research Institute, Austrian Academy of Sciences
Institute of Experimental Physics, Graz University of Technology

Advisor:

Prof. Erich Leitgeb
Institute of Microwave and Photonic Engineering
Graz University of Technology

Co-Advisors:

Dr. Werner Magnes
Space Research Institute
Austrian Academy of Sciences

Dr. Roland Lammegger
Institute of Experimental Physics
Graz University of Technology

Graz, June 2013

Eidesstattliche Erklärung

Ich erkläre an Eides statt, dass ich die vorliegende Arbeit selbstständig verfasst, andere als die angegebenen Quellen/Hilfsmittel nicht benutzt und die den benutzten Quellen wörtlich und inhaltlich entnommenen Stellen als solche kenntlich gemacht habe.

Graz, am 19. Juni 2013

Unterschrift

Statutory Declaration

I declare that I have authored this thesis independently, that I have not used other than the declared sources / resources and that I have explicitly marked all material which has been quoted either literally or by content from the used sources.

Graz, June 19th, 2013

Signature

Abstract

The Coupled Dark State Magnetometer (CDSM) is a new type of scalar magnetometer based on two-photon spectroscopy of free alkali atoms. A quantum interference effect called Coherent Population Trapping (CPT) leads to narrow optical resonance features, that enable a precise determination of the magnetic field dependent Zeeman energy level shifts. Systematic errors which usually degrade the accuracy of single CPT magnetometers are cancelled or at least minimized by the use of several CPT resonances in parallel.

It was the main objective of this thesis to identify and design the control loops which are required to enable an accurate and reliable magnetic field measurement based on the CDSM principle. All identified control loops should be implemented in a control unit with reduced mass and power consumption in order to enable measurements outside of the laboratory environment, e.g. absolute measurements at a geomagnetic observatory. Furthermore, the unit should be entirely implementable with space grade components and compliant with the resource and interface requirements of the Electro-Magnetic Satellite (EMS) mission. The Chinese low Earth orbit EMS mission is the first flight opportunity of the CDSM aboard a spacecraft.

In total five control loops were identified to enable a reliable operation. A prototype was developed as an Engineering Model (EM) for the EMS mission in which all electronic components are available with a space qualified grade. The sensitivity of 40 to 80 pT at 1 s integration time does not depend on the selectable instrument bandwidth. The dynamic range spans from demonstrated 25 nT up to extrapolated 1 mT with identical performance. The instrument has a mass of 774 g and the measured power consumption for the EMS power interface is 5267 mW in air and 3498 mW in vacuum. For an optimized power interface the calculated power consumption is 2515 mW in air and 1427 mW in vacuum.

This development is equivalent to a raise of the Technology Readiness Level (TRL) of the CDSM instrument for the EMS mission from 1 (basic principles observed and reported) to 5 (component and/or breadboard validation in relevant environment).

Kurzfassung

Das Coupled Dark State Magnetometer (CDSM) ist ein neuartiges Skalarmagnetometer, das auf dem Prinzip der Zweiphotonen-Spektroskopie von freien Alkaliatomen basiert. Der verwendete quantenmechanische Coherent Population Trapping (CPT) Effekt führt zu sehr schmalen optischen Linienbreiten und ermöglicht eine präzise Bestimmung des Magnetfelds anhand der Zeeman-Verschiebung von Energieniveaus. Systematische Fehler, wie sie bei Magnetometern basiered auf der Auswertung einzelner CPT Resonanzen auftreten, werden beim CDSM durch die gleichzeitige Verwendung mehrerer optischer Resonanzen aufgehoben oder zumindest minimiert.

Diese Arbeit beschreibt die Identifizierung aller systemrelevanten Parameter sowie den Entwurf von Regelmechnismen, die eine zuverlässige Magnetfeldmessung durch das CDSM ermöglichen. Alle notwendigen Funktionsblöcke sollen in einer gewichts- und leistungsverbrauchsoptimierten Kontrolleinheit implementiert werden, um Vergleichsmessungen außerhalb des Labors, z.B. in einem geomagnetischen Observatorium, zu ermöglichen. Das entworfene Gerät soll vollständig mit weltraumqualifizierten Bauteilen implementierbar sein und den Vorgaben der Electro-Magnetic Satellite (EMS) Mission entsprechen. EMS ist ein chinesischer Satellit in niedriger Erdumlaufbahn (low Earth orbit) an Bord dessen die Weltraumtauglichkeit des CDSM erstmals demonstriert werden soll.

Insgesamt wurden fünf Regelkreise identifiziert und realisiert. Der implementierte Prototyp entspricht den Vorgaben der EMS-Mission und kann vollständig mit weltraumqualifizierten Bauteilen aufgebaut werden. Die gemessene Empfindlichkeit beträgt 40 bis 80 pT bei einer Integrationszeit von 1 s und ist unabhängig von der Bandbreite. Der dynamische Messbereich erstreckt sich von gemessenen 25 nT bis errechneten 1 mT bei gleichbleibender Messqualität. Das Gewicht und der Leistungsverbrauch des für die EMS-Mission entwickelten Instruments betragen 774 g, sowie 5267 mW in Luft und 3498 mW in Vakuum. Für eine effiziente Spannungsversorgung wurden 2515 mW in Luft und 1427 mW in Vakuum errechnet.

Die in dieser Arbeit beschriebene Entwicklung entspricht einer Anhebung des Reifegrads der Technologie (technology readiness level) für die EMS Mission von Stufe 1 (Beobachtung und Beschreibung des Funktionsprinzips) auf 5 (Versuchsaufbau in Einsatzumgebung).

I would like to thank everyone who made this work possible and helped me in a professional and personal way.

Contents

1 Introduction **1**

2 Measurement Principle **6**

3 Detection Techniques **11**
3.1 Frequency Modulation Spectroscopy 11
3.2 Direct Digital Synthesis 16

4 Control Unit Design and Evaluation **19**
4.1 Control Loop to Track Zeeman Resonances 21
4.1.1 Overview 21
4.1.2 Synthesis of the Zeeman Frequency f_B 25
4.1.3 R-2R Digital-to-Analogue Converter 26
4.1.4 Photodiode, Pre-amplifier and Analogue-to-Digital Converter . 29
4.1.5 Lock-in Amplifier 35
4.1.6 Controller 42
4.1.7 Processing of Vector Magnetometer Data 44
4.2 Control Loops to Track Fine Structure Transition 47
4.2.1 Control Loop to Set Laser Temperature 48
4.2.1.1 Overview 48
4.2.1.2 Synthesis of Duty Cycle 49
4.2.1.3 Output Structure 50
4.2.1.4 Temperature Measurement 54
4.2.1.5 Controller 56
4.2.2 Control Loop to Set Laser Current 59
4.2.2.1 Overview 60
4.2.2.2 Mapping of Actuating Variable 62
4.2.2.3 Current Generator 63
4.3 Control Loop to Track Hyperfine Structure Transition 66
4.3.1 Overview 66
4.3.2 Analogue Output Circuit 69

4.4 Control Loop to Set Rubidium Temperature 71
4.4.1 Overview 71
4.4.2 Synthesis of Duty Cycle 72
4.4.3 Temperature Measurement 72
4.4.4 Controller 75

5 Instrument Performance **78**
5.1 Required Resources 78
5.2 Measurement Characteristics 79

6 Conclusion and Outlook **83**

List of Figures **85**

List of Tables **87**

List of Abbrevations **88**

References **91**

Author's Publications **96**

1 Introduction

Most magnetometers used for scientific space missions in the last 20 years have been based on the fluxgate principle [1] [2] [3]. The main reasons for this are the extensive heritage and reliability over several decades and the low power and mass requirements. Fluxgates produce a three-component vector output proportional to the magnitude and direction of the magnetic field with an absolute error which is dominated by inherent uncertainties, in particular the sensor offsets. In several scientific space missions, full science return can only be achieved by an additional scalar magnetometer which measures the magnitude of the magnetic field with a low absolute error ($< 1\,\mathrm{nT}$) [1].

In the last few decades, scalar magnetometers used in scientific space applications have been based either on the Overhauser effect [1] [2] [3] (e.g. onboard Ørsted [4] [5] and CHAMP) or the optically pumped helium technique [1] [2] [3] (e.g. onboard Cassini [6] and under development for Swarm [7]).

Both types require a complex sensor design in order to guarantee isotropic, "dead zone free" measurements. This is achieved, for example, by a double cell unit in which

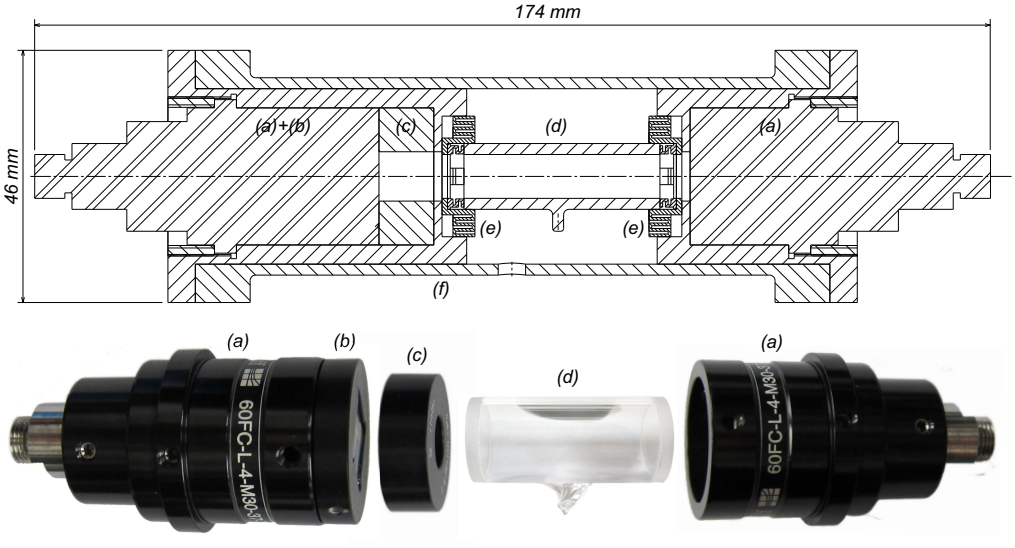

Figure 1.1: Cross section of CDSM sensor and pictures of implemented components.

Table 1.1: Main orbit parameters of the EMS satellite [18].

Orbit type	Sun synchronous, circular and polar orbit
Altitude/km	500
Inclination/°	98
Local time of descending node	14 p.m.
Revisiting cycle/d	5

one cell compensates the dead zone of the other, or a piezo-electric motor which is used to change the polarization of the exciting light field according to the magnetic field direction. Moreover, artificial magnetic fields or radio frequency signals are needed for the excitation of the medium used in the sensor cell.

The Coupled Dark State Magnetometer (CDSM) is a scalar magnetometer which is based on two-photon spectroscopy of free alkali atoms [8]. As for other types of optically pumped magnetometers the magnetic field measurement is based on the Zeeman effect. In the presence of an external magnetic field the degeneracy of hyperfine structure energy levels is lifted and results in a splitting of the levels as a function of the magnetic field strength. Additionally, a quantum interference effect called Coherent Population Trapping (CPT) [9] [10] [11] [12] leads to narrow resonance features and thus enables a precise determination of the magnetic field dependent Zeeman energy level shifts [13] [14] [15].

Thus far CPT is the only known effect used in optical magnetometry which inherently enables omni-directional measurements [13] [16]. This leads to a simple all-optical sensor design without double cell units, excitation coils or electro-mechanical parts. The CDSM sensor unit shown in Figure 1.1 consists of two fibre couplers (a), a polarizer (b), a quarter-wave plate (c), a rubidium-filled glass cell (d) mounted between meander-shaped damping elements (e) and the sensor housing made of Polyether Ether Ketone (PEEK) (f).

Furthermore, the CDSM uses a combination of several CPT resonances which ideally reduces the dependence on the sensor temperature to zero [8] [17] and leads to a high dynamic range from 25 nT up to 1 mT with identical performance [14] [15].

The CDSM measurement principle was discovered by Roland Lammegger, a senior scientist at the Institute of Experimental Physics (IEP), Graz University of Technology in 2007 [8]. In the same year a cooperation with the Space Research Institute (IWF), Austrian Academy of Sciences was started in order to evaluate the measurement principle for space applications and to develop the first prototype.

At the time of writing this thesis, the CDSM has been selected for a first flight

Table 1.2: CDSM interface and performance requirements for the EMS mission[a].

Power interface	±12 V, 5 V (unregulated)
Dynamic range and resolution	10^3 - 10^5 nT, 12 pT
Sensitivity	100 pT at 1 s integration time
Data rates	30 Hz and 1 Hz
Operating temperature ranges	
Electronics box	-15 to 50°C
Sensor unit	-70 to 80°C
Expected total ionizing dose	$<$ 10 krad(Si)

[a]Extracted from Technical Plan document set up by the NSSC and the IWF, not published.

aboard the Electro-Magnetic Satellite (EMS) mission. Furthermore, it is under consideration for the JUpiter ICy Moon Explorer (JUICE) mission of the European Space Agency (ESA) to visit the Jovian system, focused on the study of the Jupiter's moons Ganymede, Callisto, and Europa [19]. The EMS mission is scheduled for launch in 2016 and will be the first Chinese platform for the investigation of natural electromagnetic phenomena with a major emphasis on earthquake monitoring from space in a polar Low Earth Orbit (LEO) [18]. The main orbit parameters of the EMS satellite are listed in Table 1.1. In order to fulfil the scientific objectives, the EMS measures various physical parameters including electric field, magnetic field, ionospheric plasma and high energy particle disturbances.

The magnetometer instrument should cover a frequency range from DC to 60 Hz. It is developed in a cooperation between the National Space Science Center (NSSC) of the Chinese Academy of Sciences, the IWF and the IEP. The NSSC is responsible for the dual sensor fluxgate magnetometer, the instrument processor and the power supply unit, while IWF and IEP joinly develop the CDSM. An absolute magnetometer is important for full science return, since the satellite is flying in low Earth orbit. The required accuracy of 0.2 nT can only be achieved with a combined measurement of both the relative vector and the absolute scalar field due to the high terrestrial background field. The interface and performance requirements of CDSM for the EMS mission are summarized in Table 1.2. The mission also serves as an opportunity to demonstrate the CDSM measurement principle and the developed instrument design in space for the first time.

The objectives of the work covered by this thesis are

- to identify all control loops required to enable an accurate and reliable magnetic field measurement based on the CDSM principle,
- to design and implement all identified control loops in a single unit with reduced mass and power consumption in order to enable measurements outside the laboratory environment, e.g. absolute measurements at a geomagnetic observatory,
- to design the control unit for an implementation with space grade components,
- to design the control unit compliant with the interface and performance requirements for the EMS mission (see Table 1.2).

The development of the control unit as above is equivalent to raising the Technology Readiness Level (TRL)[1] from 1 (basic principles observed and reported) to 5 (component and/or breadboard validation in relevant environment).

The content of this thesis can be summarized as follows: Chapter 1 gives an introduction of high accuracy magnetometers which have already been used for scientific space missions and lists the possible advantages of the CDSM in comparison. It also introduces the requirements for the Electro-Magnetic Satellite mission which is the first flight opportunity of the CDSM aboard a spacecraft. In Chapter 2, the CDSM measurement principle is presented, the characteristics of the magnetic field dependent CPT resonance features are discussed and the method used to compensate possible systematic errors is outlined. In Chapter 3, two important detection techniques are introduced which are essential for the instrument design: Frequency Modulation Spectroscopy (FMS) is a method capable of sensitive and rapid measurement of weak spectral features and Direct Digital Synthesis (DDS) is a technique to generate periodic signals and control precisely the output frequency and phase. Chapter 4 discusses the instrument design. In total five control loops are identified as necessary for a reliable and accurate operation of the CDSM. A physical justification and an overview of the control loop design is given for each control loop. Furthermore, all function blocks which are part of the control unit are discussed in detail. Chapter 5 presents the resource requirements which were measured at the implemented prototype for the EMS mission and calculated for a power interface optimized implementation. Performance metrics such as accuracy, characteristics of the power

[1] Technology Readiness Level (TRL) is a measure used to assess the maturity of evolving technologies during its development and in some cases during early operations. ESA classification. Retrieved from http://en.wikipedia.org/wiki/Technology_readiness_level on May 29, 2013.

spectral density of detection noise, temperature dependence and dynamic range are given. Chapter 6 summarizes the work accomplished and the results achieved within this thesis and gives an outlook on upcoming development and evaluation steps.

2 Measurement Principle

This chapter gives an overview of the CDSM measurement principle, discusses the resulting magnetic field dependent resonance features and the method used to compensate possible systematic errors.

In 1992, *Scully* and *Fleischhauer* showed theoretically that CPT resonances could be applied as a sensitive magnetometer device [20] [21]. The first experimental realization of a single CPT dark state magnetometer was reported in 1998 [13]. Even though a variety of potential applications on ground and in space are given for a magnetometer based on the CPT effect [22] [13] [12] [23] [24] [25], there are still non-trivial problems of systematic measurement errors which significantly degrade the performance of a single Dark State Magnetometer (DSM).

In the presence of magnetic fields several CPT resonances in the form of a spectrum arise [12] [16]. Ideally, the frequency difference of each component of this spectrum is determined by the Breit-Rabi formula [26] [23] [27] here expressed as a Taylor series expansion [15]

$$\nu_B = \frac{\mu_B}{(2I+1)h}[n(g_J - g_I) + 8\Delta m g_I]B + [...]B^2 \tag{2.1}$$

where μ_B refers to the Bohr magneton, I to the nuclear spin, h to the Planck

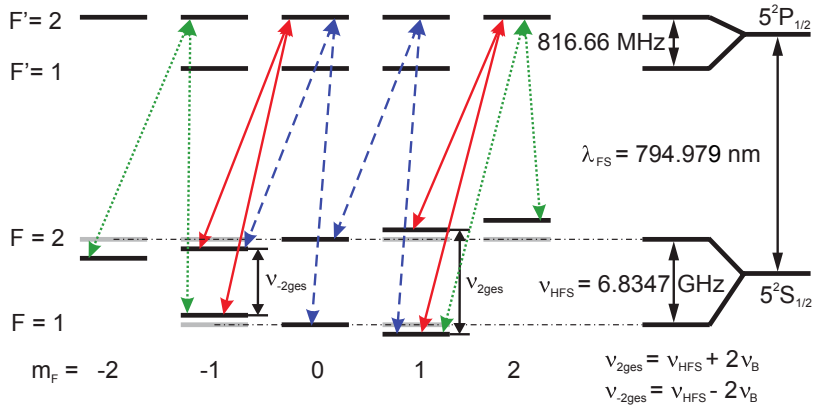

Figure 2.1: D_1 spectral line excitation scheme within the hyperfine structure of ^{87}Rb.

constant, n to the sum of the total magnetic quantum numbers m_{F_1} and m_{F_2}, g_J and g_I to the Landé g-factors, Δm to the difference of m_{F_1} and m_{F_2} and B to the magnetic flux density.

Figure 2.1 shows the D_1 excitation scheme within the hyperfine structure of ^{87}Rb. The total angular momentum quantum numbers and the magnetic quantum numbers of the $5^2S_{1/2}$ ground state are denoted by F and, correspondingly, by m_F while for the $5^2P_{1/2}$ excited states the labels are primed. The vacuum-wavelength λ_{FS} corresponds to the fine structure transition $5^2S_{1/2} \rightarrow 5^2P_{1/2}$. The hyperfine ground state splitting frequency is denoted by ν_{HFS}. Each pair of arrows builds up a so called Λ-system which causes a magnetic field dependent CPT resonance. The energy shift introduced by the magnetic field is expressed by ν_B. According to the selection rules of two photon transition [16], one Λ-system with $n = 0$ (not shown), four Λ-systems with $n = \pm 1$ (blue, dashed, only two of them are shown), two with $n = \pm 2$ (red, solid) and two with $n = \pm 3$ (green, dotted) are possible.

For high sensitivity magnetometry, an additional buffer gas is required in the rubidium-filled glass cell [12] [14] (see Figure 1.1) which introduces temperature and pressure dependent frequency shifts [8] [17] of the hyperfine ground state splitting frequency ν_{HFS} (see Figure 2.1). In the case of a single CPT resonance this cannot be distinguished from magnetic field changes [8]. Therefore, the temperature of the sensor cell must be precisely controlled to enable useful absolute magnetic field measurements. As an example, for caesium and 8 kPa of the buffer gas neon the temperature must be controlled with a precision of 10 mK in order to keep the sensor temperature dependent drift below 10 pT [23].

Additionally, the AC Stark effect [27] causes shifts of the relative position of the ground states $F = 1$ and $F = 2$ which are proportional to the applied light intensity and to the strength of the CPT transition [28]. Therefore, the total frequency of CPT resonance features in the presence of external magnetic fields is given by

$$\nu_{total} = \nu_B + \nu_T + \nu_P + \nu_L + \nu_{HFS'} \tag{2.2}$$

where ν_B depends on the magnetic field, ν_T on the buffer gas temperature, ν_P on the buffer gas pressure, ν_L on the light shift and $\nu_{HFS'}$ is the frequency of the unperturbed electric dipole forbidden transition $5^2S_{1/2}$, $F = 1$, $m_F = 0 \leftrightarrow 5^2S_{1/2}$, $F = 2$, $m_F = 0$ [29] [27].

Systematic errors are also introduced by the limited long-term frequency stability of the commercial high performance microwave oscillators used to generate the coherent frequency components of the laser excitation field [22].

The CDSM principle was discovered in 2007 [8]. It simultaneously probes two or more CPT resonances which are almost symmetric with respect to the electric dipole forbidden transition $5^2S_{1/2}$, F = 1, $m_F = 0 \leftrightarrow 5^2S_{1/2}$, F = 2, $m_F = 0$ (see Figure 2.1). The crucial idea is to separate the microwave frequency ν_{HFS} used to bridge the ground state hyperfine splitting and the frequency ν_B (up to several MHz) needed to couple and detect the Zeeman-shifted CPT resonances. Consequently, the systematic frequency shifts introduced by the microwave oscillator, the light shift or the shift due to buffer gas pressure and temperature are virtually the same for detected single CPT spectral features with respect to the ground states $F = 1, m_F = 0$ and $F = 2, m_F = 0$ [8]. These systematic errors cancel due to the superposition of CPT resonances, since in the CDSM approach only the frequency difference of the resonances is measured.

In this way, the measurement of the magnetic field is reduced to a frequency measurement which can be converted to a magnetic flux density B by applying the Breit-Rabi formula discussed in Equation 2.1, where only fundamental natural constants are contained.

According to [16], derived under the assumption of negligible influence of optical pumping, the relative strength of the CPT resonances follows

$$S_{rel} \propto cos^2\theta \quad for \quad n = 0, \pm 2 \tag{2.3}$$

$$S_{rel} \propto sin^2\theta \quad for \quad n = \pm 1, \pm 3 \tag{2.4}$$

where S_{rel} is the relative strength of the CPT resonance and θ is the angle between the direction of the laser field propagation and the magnetic field. Therefore, CPT resonances with even-numbered indices n reach their maxima at magnetic field directions longitudinal with respect to the light field propagation direction in the sensor and scale in their relative strength with $\cos^2(\theta)$ while resonances with odd-numbered indices have peaks at the transverse magnetic field direction and scale with $\sin^2(\theta)$. This was demonstrated for CPT resonance superpositions with ^{87}Rb atoms in [30].

In Figure 2.2, the Zeeman frequency sweeps extracted from [30] show the absorption (red, dashed) and dispersion (blue, solid) signals of three CPT resonance superpositions (n = ±1, ±2, ±3) obtained by frequency modulation spectroscopy methods (see Section 3.1) at different angles of the magnetic field with respect to the light field propagation direction in the sensor (0° to 90°). The applied field is approximately 6500 nT while the Zeeman-shifting factors [15] [23] of the magnetic field dependent resonances are approximately 7, 14 and 21 Hz/nT, respectively. Here, the optical pumping of the CPT resonances is not entirely negligible and causes a deviation in the predicted resonance amplitudes compared with the model developed in [16]. However, for every angle at least one of the three CPT resonance superpositions n = ±1, ±2, ±3

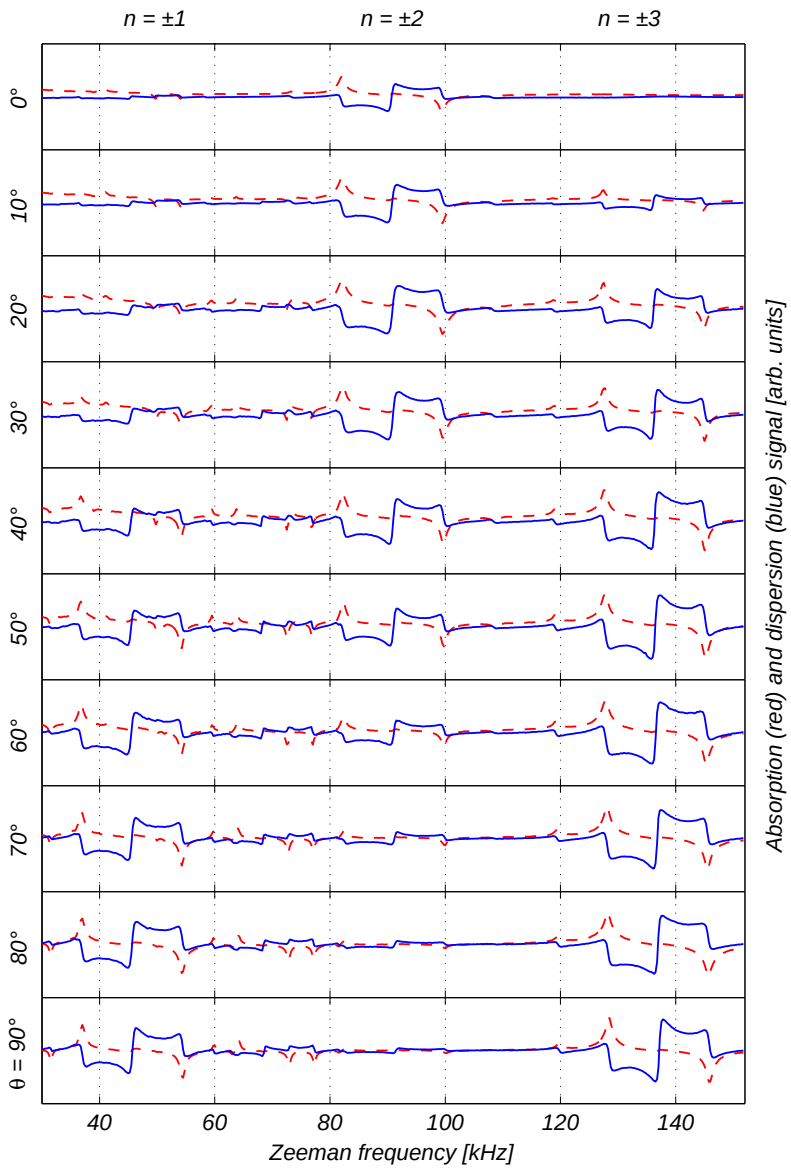

Figure 2.2: Dependence of the CPT resonance superpositions on the angle θ [30].

is always detectable and, by a proper selection, omni-directional measurements are possible without the need of a complex sensor design, for example additional moving parts or excitation coils at the sensor [30].

The Zeeman-shifting factors listed in Table 2.1 are determined by calculation. The

Table 2.1: Zeeman-shifting factors determined by calculation.

CPT resonance superposition index n	Zeeman-shifting factor (Hz/nT)
±1a	6.9958
±1b	7.0237
±2	14.0195
±3	21.0154

thus far defined resonance superposition $n = \pm 1$ is actually a simplified model for the overlay of four Λ-systems. However, the Zeeman-shifting factors are pairwise different for the Λ-systems which is a consequence of different quantum numbers applied in the Breit-Rabi formula in Equation 2.1. This results in two resonance superpositions $n = \pm 1a$ and $n = \pm 1b$ which overlap for small fields ($< 5000\,\mathrm{nT}$ which corresponds to a frequency separation of approximately 35000 Hz) [31]. A heading error is possible since the superposition of $n = \pm 1a$ and $n = \pm 1b$ can be asymmetric. For the Earth's field both superpositions are well separated and no heading error occurs since the instrument is locked to one of both.

In practice, the resonance superposition $n = \pm 3$ is preferred over $n = \pm 1a$ or $n = \pm 1b$. This derive from the fact that there is no heading error for $n = \pm 3$ even for small fields. Additionally, the higher Zeeman-shifting factor leads to a lower magnetic field strength detection noise.

3 Detection Techniques

Frequency Modulation (FM) spectroscopy is introduced in Section 3.1 which is a technique for the detection of the CPT resonance features. Section 3.2 discusses the principle and the characteristics of Direct Digital Synthesis (DDS) which is a method to generate periodic signals and precisely control the frequency and phase. It is e.g. used to generate the signal with the magnetic field dependent frequency information f_B.

3.1 Frequency Modulation Spectroscopy

In 1983, *Bjorklund*, *Levenson*, *Lenth* and *Ortiz* introduced FM spectroscopy which is a method capable of sensitive and rapid measurement of narrow and weak spectral features [32], e.g. CPT resonances [22]. The basic setup is shown in Figure 3.1. To enable FM spectroscopy, the laser carrier signal

$$E_0(t) = E_0 cos(\omega_0 t) \tag{3.1}$$

with the amplitude E_0 and the angular frequency ω_0 is frequency modulated with a sinusoidal signal with the frequency ω_{ref}.

Theoretically, the FM creates an infinite set of discrete frequency sidebands at frequencies $\omega_0 \pm n\,\omega_{ref}$ (n = 1, 2, ...) symmetric to the carrier [33]. For $M \approx 1$, the frequency modulated signal E(t) can be written in a simplified form as

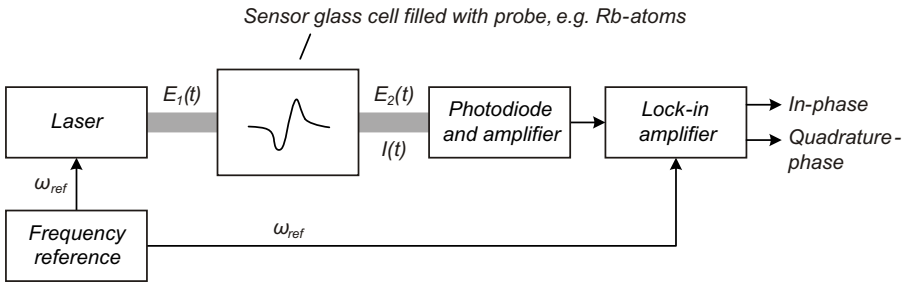

Figure 3.1: Block diagram to enable frequency modulation spectroscopy.

$$E_1(t) = E_0 J_0 \, cos(\omega_0 t) - \\ - E_0 J_1(M) \, cos\left[(\omega_0 - \omega_{ref})t\right] + E_0 J_1(M) \, cos\left[(\omega_0 + \omega_{ref})t\right] \tag{3.2}$$

where M = $\frac{\Delta\omega}{\omega_{ref}}$ is called the modulation index. The frequency deviation $\Delta\omega$ is defined as maximum deviation of the instantaneous frequency to the carrier frequency and depends on the amplitude of the modulation signal. According to Equation 3.2, the amplitudes of the carrier and the n-th order sidebands are given by n-th order Bessel functions J_n(M) [33]. For M $\approx$ 1, most energy is contained in the carrier and the first order sidebands. Therefore, the simplified form of Equation 3.2 is applicable.

In consequence, the electric field E_1 of the FM laser field can be written as

$$E_1(t) = E_0 \left[J_{-1} e^{i(\omega_0 - \omega_{ref})t} + J_0 e^{i\omega_0 t} + J_{+1} e^{i(\omega_0 + \omega_{ref})t} \right] \tag{3.3}$$

and is guided through the rubidium-filled glass cell. The indices -1, 0, $+1$ correspond to the lower sideband, the carrier and the upper sideband, respectively.

Based on Beer's law, the interaction of the multi-chromatic light field with rubidium atoms in a glass cell can be described by a frequency-dependent transfer function T(ω) for the E-field amplitude

$$T(\omega) = e^{-\delta(\omega) - i\phi(\omega)} \tag{3.4}$$

where the attenuation factor $\delta(\omega)$ is related to the frequency dependent absorption coefficient $\alpha(\omega)$ by

$$\delta(\omega) = \frac{\alpha(\omega) L}{2} \tag{3.5}$$

with the cell length L. The phase shift $\phi(\omega)$ is related to the refractive index n(ω) by

$$\phi(\omega) = n(\omega) \frac{L\omega}{c} \tag{3.6}$$

where c refers to the speed of light [32]. Thus, the transmitted beam after the interaction in the cell is given by

$$E_2(t) = E_0 \left[T_{-1} J_{-1} e^{i(\omega_0 - \omega_{ref})t} + T_0 J_0 e^{i\omega_0 t} + T_{+1} J_{+1} e^{i(\omega_0 + \omega_{ref})t} \right]. \tag{3.7}$$

The electric field E_2 is detected e.g. by a photodiode which is sensitive to the intensity of the light field beam[1] with

$$I = \frac{c|E_2|^2}{8\pi}\,. \tag{3.8}$$

For small arguments of M the Bessel functions can be approximated by $J_n \approx \frac{1}{2^n n!}M^n$ and because of the symmetry property $J_{-n}(M) = (-1)^n J_n(M)$ it can be assumed that $J_0 \approx 1$ and $J_{\pm 1} \approx \pm\frac{M}{2}$. Under the assumption of weak attenuation/absorption ($|\delta_0 - \delta_{+1}|$ and $|\delta_0 - \delta_{-1}| \ll 1$) and small phase changes ($|\phi_0 - \phi_{+1}|$ and $|\phi_0 - \phi_{-1}| \ll 1$) the received intensity of the light field results in

$$I = \frac{cE_0^2}{8\pi}e^{-2\delta_0}\left[1 + (\delta_{-1} - \delta_{+1})\,M\cos\omega_{ref}t + (\phi_{+1} + \phi_{-1} - 2\phi_0)\,M\sin\omega_{ref}t\right]. \tag{3.9}$$

An amplifier converts the modulated photodiode current into an input voltage for the lock-in amplifier. The modulation signal with the frequency ω_{ref} is additionally provided to the lock-in amplifier as reference signal to enable a coherent demodulation of the voltage detected by the photodiode and amplifier. It is shifted in phase in order to consider different propagation paths.

In general, the in-phase signal, or cosine component, of a dual-phase lock-in amplifier is the result of the demodulation of the input voltage with the unchanged reference signal, while for the quadrature-phase signal, or sine component, the input is mixed with a 90 ° phase-shifted version of the reference signal. According to Equation 3.9, the cosine component can be interpreted as the difference between the absorption of the light in the medium (here the ^{87}Rb-filled glass cell) which is experienced by both first order sidebands. The sine component is proportional to the difference of the phase shifts relative to the phase of the modulation signal ω_{ref} which is experienced by the carrier to the average of the phase shifts of the two sidebands [32].

The attenuation factor $\delta(\omega)$ in Equation 3.5 and the refractive index n(ω) in Equation 3.6 are a measure for the interaction of multi-chromatic light field with rubidium atoms in the glass cell. In order to visualize $\phi(\omega)$ and n(ω), the in-phase and quadrature-phase outputs of the lock-in amplifier are recorded for a sweep of the carrier frequency ω_0 of the FM over the resonance feature (see Figure 3.2 and Figure 3.3). The interaction unbalances the sidebands of the light field. This results in an amplitude modulation of the transmitted laser light intensity I(t) at the modula-

[1] The derivation presented here follows the treatment in [32] where cgs-units are used for the electromagnetic quantities $\vec{E}$ and $\vec{B}$ of the light field.

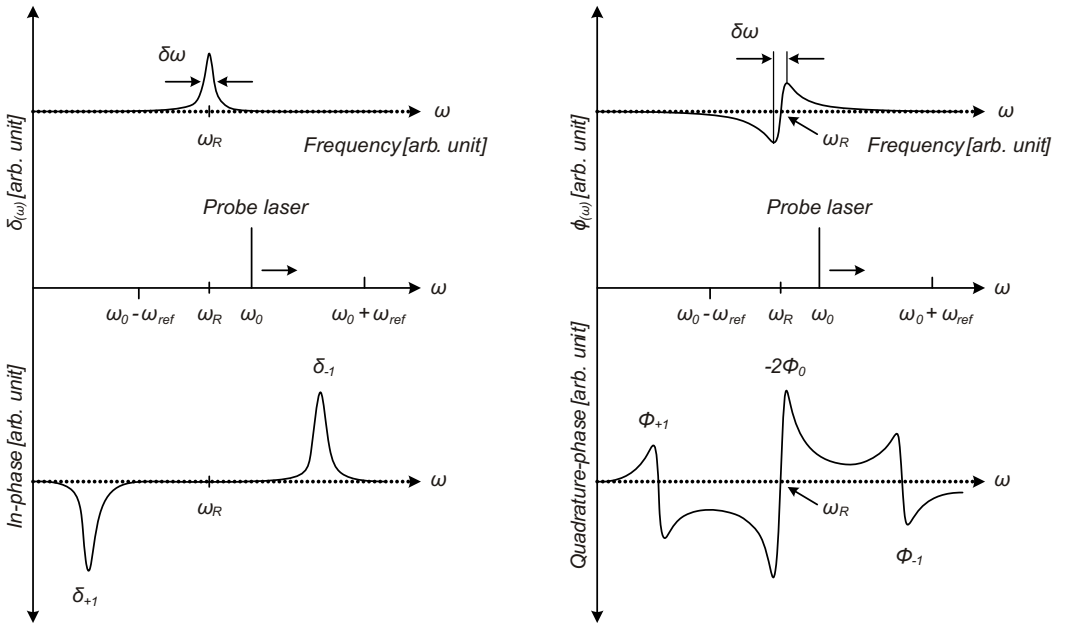

Figure 3.2: Spectra for frequencies ω_{ref} larger than the probed resonance linewidth $\delta\omega$.

tion frequency ω_{ref} with the amplitude depending on the absorption $\delta(\omega)$, the phase shift $\phi(\omega) \sim \mathrm{n}(\omega)$ of the carrier and the sidebands.

Two different cases are applied for the CDSM instrument. In Figure 3.2 the modulation frequency ω_{ref} is larger than the linewidth of the CPT resonance and, therefore, it is probed mostly by a single sideband. During a sweep of the FM light field spectrum over the resonance, first the upper sideband, then the carrier and finally the lower sideband are interacting with the resonance feature individually. Far from resonance, the two sidebands and the carrier experience the same absorption and phase shift. Hence, the resulting in-phase and quadrature-phase signals of the lock-in amplifier are zero. When the upper sideband comes to resonance, it is absorbed and phase shifted while the carrier and the lower sideband are not influenced. The shape of in-phase signal over the spectrum reproduces the shape of the resonance, while the quadrature-phase signal is equivalent to its dispersion relative to the average dispersion far off the resonance. In case of the carrier is in resonance ($\omega_0 = \omega_R$), the in-phase signal spectrum remains zero, while the quadrature-phase signal continues reproducing the dispersion of the resonance. This is due to the fact that the absorption, and consequently the in-phase signal, is a function of the difference of the upper and lower sidebands. Both are symmetric and cancel each other for $\omega_0 = \omega_R$.

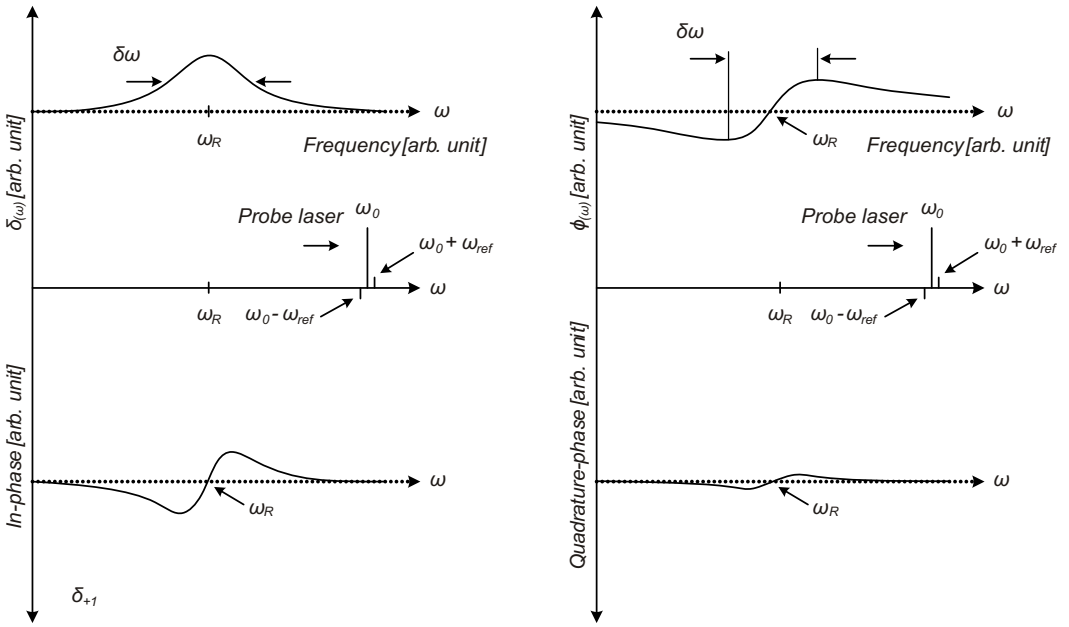

Figure 3.3: Spectra for frequencies ω_{ref} smaller than the probed resonance linewidth $\delta\omega$.

The in-phase signal of the lower sideband in resonance points in opposite direction compared to the upper sideband due to the phase shift of 180 °.

In Figure 3.3 the modulation frequency ω_{ref} is smaller than the linewidth of the resonance and both sidebands experience absorption and phase shifts at the same time. Assuming again a sweep of the FM light field spectrum over the resonance, the upper sideband is more absorbed than the lower sideband when the carrier frequency is smaller than the resonance frequency. The difference of the sideband amplitudes determines the amplitude of the in-phase signal. When the carrier is in exact resonance with the spectral feature ($\omega_0 = \omega_R$), both sidebands are absorbed equally which results in an in-phase signal of zero. When the frequency of the carrier is larger than the one of the resonance, the upper sideband is less absorbed than the lower sideband. The difference of sideband amplitudes results in an in-phase signal with inverse sign. Consequently, the overall in-phase spectrum is proportional to the first derivative of the absorption. The quadrature-phase signal is related to the second derivative of the dispersion. For small modulation frequencies compared to the linewidth of the spectral feature, the amplitude of the quadrature-phase signal is much smaller than the in-phase signal and it can be ignored in most cases.

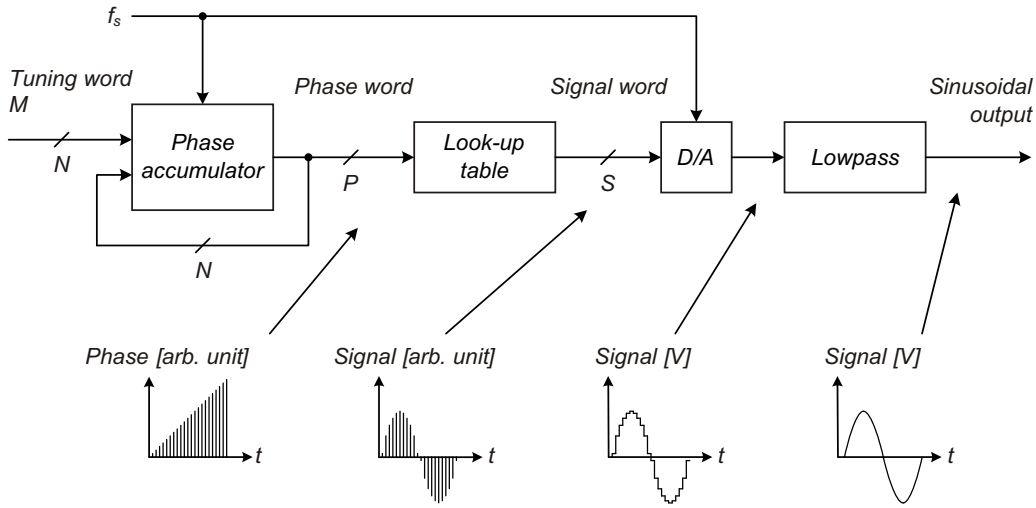

Figure 3.4: Signal flow of the direct digital synthesizer.

3.2 Direct Digital Synthesis

In 1971, *Tierney*, *Rader* and *Gold* introduced the DDS technique for using digital data processing blocks to generate frequency- and phase-tuneable periodic output signals referenced to a fixed-frequency precision clock [34].

The main characteristics are improved phase noise compared to the analogue oscillator solutions as well as instant and phase-continuous switching and arbitrarily[2] small tuning resolution of the output frequency. No manual analogue system tuning is required and, in principle, aging is limited to a single component, the reference oscillator [35].

The implementation of a DDS can be divided into two main parts as shown in Figure 3.4. The discrete-time phase accumulator generates the phase information while the phase-to-amplitude converter, for instance a Look-Up Table (LUT), outputs the desired signal word which is converted by a Digital-to-Analogue Converter (DAC) into a sinusoidal signal. The architecture relies on integer arithmetic. The width of the accumulator is N bit and, therefore, the maximum phase 2π is represented by the integer number 2^N. With every clock sample, the phase increases by the tuning word M. It takes T_0 samples to reach the maximum phase and, hence, a full period. The corresponding frequency is given by

$$f_0 = \frac{f_s}{2^N} M \tag{3.10}$$

[2]The resolution depends on the width N of the phase accumulator calculated in Equation 3.12.

where f_s is the sampling frequency of the accumulator. Derived from Equation 3.10 the minimum possible output frequency $f_{0\,min}$, which is equivalent to the smallest tuning step in frequency Δf, that the DDS can achieve:

$$f_{0\,min} = \Delta f = \frac{f_s}{2^N}\,. \tag{3.11}$$

With Equation 3.10 one can also determine the number of bits N of the phase accumulator in order to achieve a desired frequency resolution

$$N = \left\lfloor \log_2 \frac{f_s}{\Delta f} + 0.5 \right\rfloor . \tag{3.12}$$

Theoretically, the maximum frequency of a DDS is given by the Nyquist-Shannon uniform sampling theorem

$$f_{0\,max} = \frac{f_s}{2}\,. \tag{3.13}$$

From a practical point of view a lower $f_{0\,max}$ is often preferred, for instance $f_{0\,max} = 0.4$ [35] or 0.25 [36] of f_s. The lower $f_{0\,max}$ is, the easier the implementation of the low pass filter is. The filter is required to suppress the effects of the image responses in the output spectrum.

Periodic phase errors are introduced by truncating the N bit phase information of the accumulator to a P bit phase word for the phase-to-amplitude converter. The reason for the quantization is to keep the memory demands of the LUT reasonable. The truncation results in amplitude errors during the phase-to-amplitude conversion process and produces unwanted spectral components, also called spurs, in the DDS output signals [35]. A simplified formula to estimate the maximum level of spurs S_{max} assuming a carrier level of 0 dB is given by

$$S_{max} = -SFDR = -6.02\,P + 3.92\,dB \tag{3.14}$$

where SFDR is the Spurious Free Dynamic Range in decibels. A detailed discussion on the exact formulas including the frequencies and the SFDR of spurs can be found in [37], [38] and [39].

The SFDR can be improved by sine wave compression based on symmetry or on waveform approximation. For example, instead of storing the entire sine waveform $f(\phi) = \sin(\phi)$ for $0 \leq \phi \leq 2\pi$, one can store the same function for $0 \leq \phi \leq \pi/2$ and use symmetry to get the complete 2π waveform range. This approach only uses 2^{P-2} entries in the LUT, leading to a compression ratio of 8:1 [36]. The full sine wave can be reconstructed at the expense of some hardware [40], [41] and [42].

For a full-scale sine wave output signal, the Signal-to-Noise Ratio (SNR) of a DAC due to quantization errors can be approximated by

$$SNR = 6.02\,Q + 1.76\,dB \tag{3.15}$$

where Q refers to the bit resolution of the DAC. It also limits the performance of the DDS, as the output spectrum will exhibit the same noise floor. From Equations 3.14 and 3.15, the limit

$$P = Q + 1 \tag{3.16}$$

can be derived in order to ensure that unwanted signals are caused by the amplitude quantization and not by the phase truncation.

Additional spurs arise due to the imperfectness of the DAC. The non-linearity of a DAC leads to harmonic distortions. The result is harmonically related spurs in the output spectrum. The amplitude of the spurs is not readily predictable as it is a function of the DAC linearity. However, the location of such spurs is predictable, since they are harmonically related to the output frequency f_0 of the DDS [35]. Furthermore, switching transients arise within the internal physical architecture of the DAC and can cause ringing on rising and/or falling edges of the DAC output waveform. Non-symmetrical switching characteristics such as unequal rise and fall times will also contribute to harmonic distortion. The amount of distortion is determined by the effective AC or dynamic transfer function [35].

In general, the wideband spurious performance of a DDS system depends on the quality of both the DAC and the architecture of the phase truncation of the DDS core. Narrowband spurious performance depends mostly on the purity of the DDS system clock generated by an external reference oscillator [35].

The spectral characteristics of the reference clock directly impact those of the output. Timing jitter is caused by coupling noise and thermal noise which is the ultimately limiting factor for reducing timing jitter. Coupled noise can be in the form of locally coupled noise caused by crosstalk or ground loops. Sinusoidal jitter in the reference clock causes modulation sidebands to appear in the spectrum. The spectral line is unchanged. Random jitter results in an increase of the noise floor level and cause broadening of the fundamental which is known as phase noise [35]. Due to the DDS principle, the output phase noise is reduced by $20\log(R)$, expressed in decibels, where R is the ratio of the input to the output frequency [43].

4 Control Unit Design and Evaluation

The CDSM prototype is equivalent to the Engineering Model (EM) design for the Chinese scientific low Earth orbit EMS mission (see Chapter 1 and Table 1.2). The block diagram and a picture of the instrument are shown in Figure 4.1 and Figure 4.2. It consists of the mixed signal electronics board (a) with microwave and control subunits, the laser unit (b) mounted on the side of the instrument box, the sensor unit (c), the inbound and outbound fibres (d) and two twisted pair cables (e) for the sensor

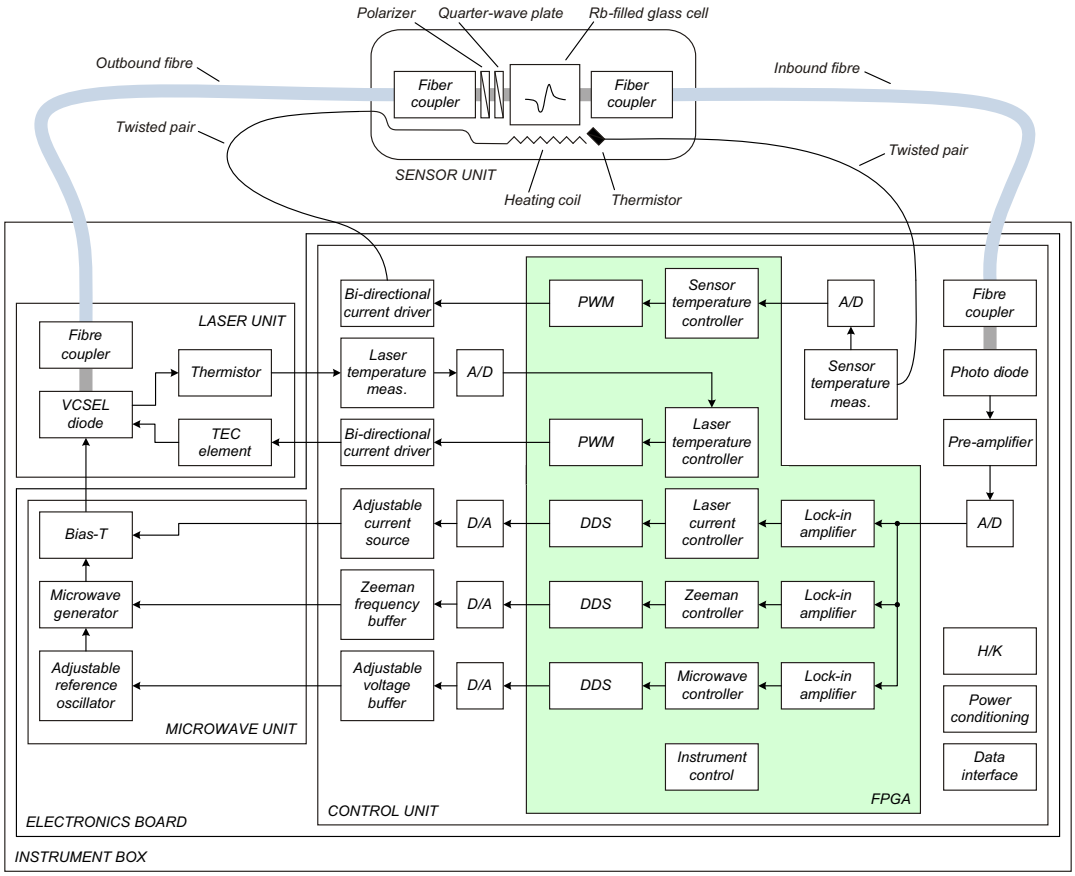

Figure 4.1: Block diagram of instrument design.

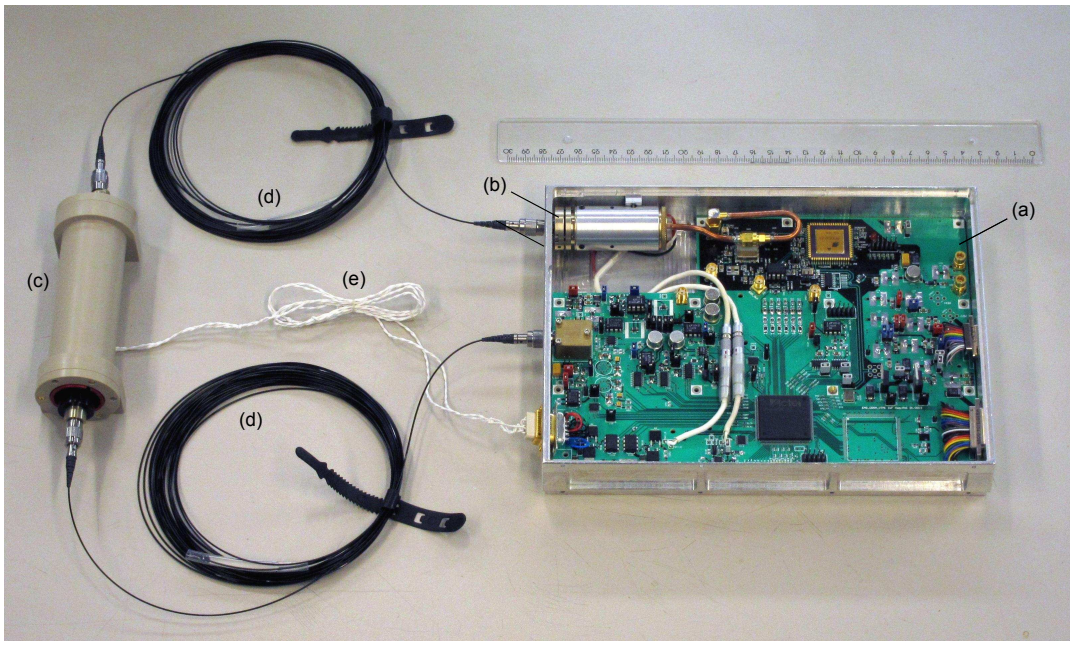

Figure 4.2: Picture of CDSM prototype equivalent to the EM for the EMS mission.

temperature measurement and the optional sensor heating in case of environmental temperatures below 15°C. A cross section of the sensor unit with pictures of the implemented components is shown in Figure 1.1.

The prototype is jointly developed by the IWF, Austrian Academy of Sciences and the IEP, Graz University of Technology. The IWF is responsible for the control unit which is part of the mixed signal board and the overall project management. The liability of the IEP covers the microwave unit of the mixed signal board, the laser unit, the sensor unit with heating coils and the sensor harness.

The design includes five control loops which are developed to track the magnetic field dependent Zeeman resonances (Section 4.1), to stabilize the laser frequency to the fine structure transition frequency $5^2S_{1/2} \rightarrow 5^2P_{1/2}$ (Section 4.2), to track the hyperfine structure transition $5^2S_{1/2}$, $F = 1$, $m_F = 0 \leftrightarrow 5^2S_{1/2}$, $F = 2$, $m_F = 0$ with the microwave generator (Section 4.3) and to adjust the temperature of the rubidium atoms in the sensor cell (Section 4.4).

4.1 Control Loop to Track Zeeman Resonances

The Zeeman control loop is established in order to track the magnetic field dependent CPT resonance superpositions $n = \pm 1$, ± 2 or ± 3 by the variable DDS generated frequency f_B which is a direct measure of the magnetic flux density B. In Section 4.1.1, a general overview on the control loop design is given. Section 4.1.2 to Section 4.1.7 discuss selected functional blocks in detail.

4.1.1 Overview

The coupled dark state magnetometer excites two or more magnetic field dependent CPT resonances in parallel to determine the surrounding magnetic field [8]. To fulfil the criteria of CPT resonance excitation [12] [22] [11] and for simplicity, this is established by a double modulated light field [15]. A third modulation is required to enable the detection with frequency modulation spectroscopy techniques [8] [32].

The Vertical-Cavity Surface-Emitting Laser (VCSEL) diode (vacuum-wavelength $\lambda_{VCSEL} = \lambda_{FS} = 794.979\,\text{nm}$) is frequency modulated by a microwave signal ($f_{MW} = \frac{1}{2}\,\nu_{HFS} = 3.417\,\text{GHz}$). Both first-order sidebands of this FM spectrum fit the hyperfine structure energy levels $F = 1, m_F = 0$ and $F = 2, m_F = 0$ of the $5^2S_{1/2}$ ground state of the rubidium D_1 line in Figure 2.1. According to the Zeeman effect [31], the energy levels with the magnetic quantum numbers $m_F = -2$, -1, $+1$, $+2$ are dependent on the magnetic field. In Figure 2.1 this is indicated by the shifted black lines while grey lines mean zero magnetic field. In order to establish permanent CPT resonances in presence of a magnetic field, the microwave frequency f_{MW} is used as carrier for a Phase Modulation (PM) whose sidebands fit and excite the magnetic field dependent energy levels.

The modulation frequency f_B of this PM is limited to 2.1 MHz by the current design which corresponds to a detectable magnetic flux density B of approx. $300\,\mu\text{T}$ for $n = \pm 1$, $150\,\mu\text{T}$ for $n = \pm 2$ and $100\,\mu\text{T}$ for $n = \pm 3$ via the corresponding Zeeman-shifting factors of approx. 7, 14 and 21 Hz/nT (see Table 2.1). It is generated in the Field Programmable Gate Array (FPGA)[1] using the DDS technique (see Sec-

[1] The radiation-tolerant Actel RT ProASIC RT3PE3000L target device is mounted in a hermetically-sealed ceramic package but is export restricted. The commercial Actel ProASIC A3PE3000L has the same silicon design and the same 0.13 μm process at United Microelectronics Corporation (UMC) as its radiation-tolerant equivalent. The ProASIC3 devices have been extensively tested for a variety of radiation effects and are expected to fit the low radiation environment in the EMS mission. Information retrieved from http://www.actel.com/products/milaero/rtpa3/default.aspx on May 29, 2013.

tion 4.1.2). The frequency component f_B is carrier for an additional third modulation of the light field with the modulation frequency f_{ref_1} which enables FM spectroscopy.

The digital FM output of the DDS is transformed to the analogue domain with a parallel DAC and is fed as modulation signal to the microwave generator in order to establish the PM. The implementation of the DAC is discussed in Section 4.1.3.

In the bias-T (see Figure 4.1) the modulated microwave signal is superposed with the signal of the current source which for now is assumed to be constant. The output is fed to the VCSEL diode as injection current in which the DC-AC superposition is transformed to the first FM via the displacement coefficient of the diode (see Section 4.2).

The result is an overall triple modulated light field spectrum whose spectral components fit to the appropriate transitions as indicated by either the blue, red or green arrows in Figure 2.1. In this way a permanent excitation of one of the magnetic field dependent CPT resonance superpositions $n = \pm 1$, ± 2 or ± 3 is achieved. The light is guided through a gradient index fibre to the sensor unit where a polarizer and a quarter-wave plate assure a circular polarized excitation field.

The CPT resonances are acting as frequency discriminator in the rubidium-filled glass cell and convert the DDS generated FM (f_{ref_1}) of the multi-chromatic light field spectrum into an amplitude modulation of the transmitted laser intensity [8] [12]. Further discussion on the interaction process is carried out in Section 3.1 and [32].

The transmitted light field is guided to the photodiode via a multimode fibre. The photodiode converts the amplitude modulated transmitted intensity I(t), that carries the rubidium-interfered information of the excited CPT resonances, to an equivalent photocurrent. A pre-amplifier converts the AC component of the current into a voltage signal, which is fed to the digital lock-in amplifier via an Analogue-to-Digital Converter (ADC). Options for the implementation of the required circuit are discussed in Section 4.1.4.

The third modulation with f_{ref_1} in combination with the lock-in amplifier enables the application of FM spectroscopy techniques capable of sensitive and rapid measurement of the narrow and weak spectral features [32]. The principle and the implementation of the lock-in amplifier are discussed in Section 4.1.5. Since the modulation frequency f_{ref_1} is larger than the linewidth of CPT resonances (typically $\delta f < 2\,\mathrm{kHz}$), the spectral feature is probed by a single sideband (see Figure 3.2 and [32]). With a modulation index $M \approx 1$, the in-phase output of the lock-in amplifier can be interpreted as absorption signal and the quadrature-phase output as dispersion signal of the CPT resonances excited in the rubidium atoms.

Due to the narrow spectral linewidth, which is a consequence of the strict physical

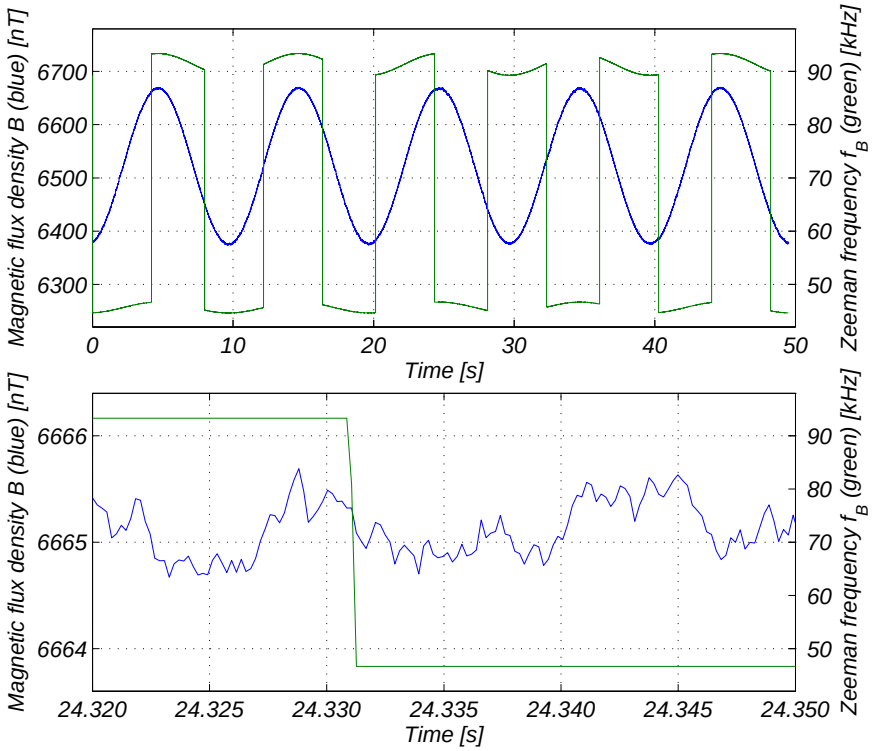

Figure 4.3: Demonstration of the CPT resonance superposition switching.

constrains of the CPT mechanism, the slope at zero crossing of the quadrature-phase signal is steep (see Figure 2.2). The point of zero crossing corresponds to the exact excitation of the magnetic field dependent hyperfine energy levels by the double modulated light field. The only variable parameter of the light field is the frequency f_B of the DDS signal while the laser carrier wavelength λ_{Laser} and the microwave frequency f_{MW} are for now assumed to be constant. The zero crossing in combination with the Zeeman controller in the FPGA (see Figure 4.1) is used to track changes of the magnetic field induced Zeeman energy levels by adapting the DDS frequency f_B (see Figure 4.20). The system identification and the controller design are discussed in Section 4.1.6. The actuating variable of this controller corresponds to f_B of the DDS signal and is, therefore, in direct relation to the magnetic field described by an appropriate form of the Breit-Rabi formula depicted in Equation 2.1.

The controller operates permanently at frequency values which are related to the resonance superposition $n = \pm 2$ via the Zeeman-shifting factor of approximately 14 Hz/nT. In case of changing the magnetic field detection from $n = \pm 2$ to the resonance super-

positions $n = \pm 1$ or $n = \pm 3$, the control loop does not need to be unlocked in order to search and follow the related zero crossings. The controller just scales the actuating variable f_B by the factors 0.5 for $n = \pm 1$ or 1.5 for $n = \pm 3$ which corresponds with sufficient accuracy to the Zeeman-shifting factors of approximately 7 Hz/nT and 21 Hz/nT, respectively (see Table 2.1). The approach of rescaling the output frequency f_B in case of a resonance change enables a quasi-continuous operation of the Zeeman control loop in all directions of the magnetic field and is the basis for the technical realization of a continuously working omni-directional magnetometer. A demonstration of this approach is shown in Figure 4.3. In this measurement [30], a magnetic field (sinusoidal, 300 nT_{pp}, 0.1 Hz and additional DC background field, 6520 nT) with the angle of $\theta = 45°$ in relation to propagation direction of the laser light field was applied. Hence, all three CPT resonance superpositions are observable (see Figure 2.2). The switching between the superposed CPT resonances $n = \pm 1$ and $n = \pm 2$ was manually triggered every 4 seconds. The measured Zeeman frequency values (green curves) have been corrected by the corresponding Zeeman-shifting factors of approximately 7 and 14 Hz/nT, respectively, in order to get the magnetic field values (blue curves). Even in the lower detailed plot, no correlation can be observed between the switching process and the magnetic field data.

In scientific space missions an absolute scalar magnetometer is always operated in combination with vector magnetometers. These measurements can be used to calculate the angle between the magnetic field and the optical axis of the sensor as well as the magnitude of the magnetic field by applying e.g. COordinate Rotation DIgital Computer (CORDIC) algorithms [44] as discussed in Section 4.1.7. The instrument controller can use this information to determine the suitable resonance superposition and to rapidly find the CPT resonances at start-up.

Both functions can also be achieved without an additional vector magnetometer. The resonances can be found in a scanning mode but this approach takes more time. For the independent switching between the CPT resonance superpositions during an ongoing measurement, the superposed sidebands of the resonances are tracked. The zero crossings in the dispersion signal of the sidebands carry the same information of the magnetic field as the actual CPT resonances. The corresponding frequency values are solely shifted from the actual Zeeman frequency by the modulation frequency used for the frequency modulation spectroscopy (f_{ref_1}). The advantage of using the sidebands can be seen for instance at the CPT resonance superposition $n = \pm 3$ for 90° in Figure 2.2. The sidebands have peaks in the absorption signal when the dispersion signal is zero. In contrast, the absorption signals at the actual CPT resonance superposition zero crossings are zero as well. The amplitude of the absorption peaks

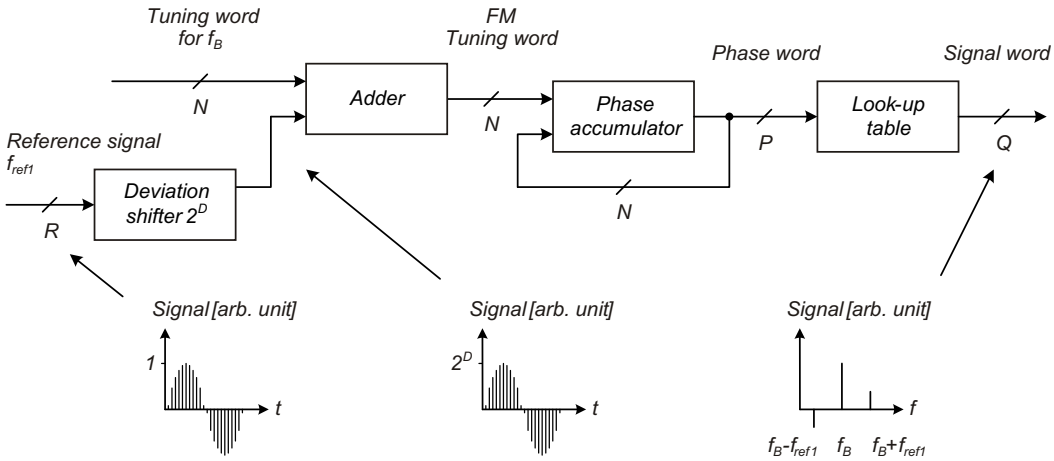

Figure 4.4: DDS block diagram to generate a frequency modulated signal.

of the sidebands are a measure for the angle θ and can be used in order to automatically switch between the superposed CPT resonances lines using a threshold-based algorithm [30].

4.1.2 Synthesis of the Zeeman Frequency f_B

The signal with the magnetic field dependent frequency f_B is generated in the FPGA using the DDS technique. Figure 4.4 shows a block diagram of the DDS implementation.

The frequency f_B is related to the magnetic flux density B via Breit-Rabi equation (see Equation 2.1) and the derived Zeeman-shifting factors of approximately 7, 14 and 21 Hz/nT correspond to the resonance superpositions $n = \pm 1$, ± 2 and ± 3, respectively. According to Table 1.2, the instrument should be able to measure magnetic flux densities up to 100 μT in all directions of the magnetic field. To fulfil the requirement and to enable further investigation of the measurement principle, this is realized for all three CPT resonance superpositions. For the superposition $n = \pm 3$, a magnetic flux density of 100 μT is equivalent to a frequency f_B of approx. 2.1 MHz. With the recommendations for the maximum DDS output frequency discussed in Section 3.2, a sampling frequency f_s of 10 MHz has been selected.

For the EMS mission, as stated in Table 1.2, the resolution of the magnetic flux density measurement Δf_B should be 12 pT in all directions of the magnetic field. In order to enable further investigation, the resolution is set to 0.1 pT and is realized for all three CPT resonance superpositions. For $n = \pm 1$, a resolution of 0.1 pT is

equivalent to a frequency resolution of 0.7 mHz. Derived from Equation 3.12, a width of the phase accumulator and tuning word of N = 34 bit is required.

The phase-to-amplitude conversion is realized by a LUT. For a DAC resolution of 12 bit (see Section 4.1.3) and according to Equation 3.16, a LUT with the size of 2^{13} x 12 bit would be required in order to ensure that unwanted signals in the analogue output signal are dominated by the amplitude quantization of the DAC and not by the phase truncation of the DDS. With sine wave compression based on symmetry as discussed in Section 3.2 only values of the function $f(\phi) = \sin(\phi)$ for $0 \leq \phi \leq \pi/2$ need to be implemented in the FPGA. This reduces the size of the LUT by a factor 8 to 2^{11} x 11 bit.

Without a further modulation signal the constant tuning word for f_B at the input of the adder in Figure 4.4 would lead to a sinusoidal DDS output signal with constant frequency. However, a modulation signal with the frequency f_{ref_1} is added and introduces an additional FM. The sinusoidal modulation signal is generated in the lock-in amplifier unit (see Section 4.1.5) and enables FM spectroscopy. It is normalized and can be scaled by D shifts to fit the required deviation frequency for a modulation index $M \approx 1$.

4.1.3 R-2R Digital-to-Analogue Converter

The FM digital DDS output signal is updated with the sampling frequency $f_s =$ 10 MHz. A DAC implementation with serial interface would require a several times higher interface clock and, consequently, FPGA clock frequency f_{FPGA}. For a single clock solution, the complexity of combinatorial logic which is processable within one clock cycle would be reduced significantly. Additionally, a higher clock rate would lead to an increase of the power consumption of the FPGA. In contrast, a DAC based on a parallel interface and conversion technique can be updated and operated at the DDS sampling frequency $f_s = f_{FPGA}$.

At the time of instrument design could not be found a space-qualified parallel DAC which met the requirements for a sampling frequency up to of 10 MHz, a moderate power consumption below 100 mW and no export restriction. Consequently, the parallel DAC was implemented as discrete R-2R network which is driven directly by FPGA outputs.

Figure 4.5 shows the typical voltage output structure of an FPGA and its equivalent circuit. Depending on the interface type, one or more e.g. Metal-Oxide-Semiconductor Field-Effect Transistor (MOSFET) totem poles are routed in parallel in order to limit the structure's influence on the output voltage level. In general,

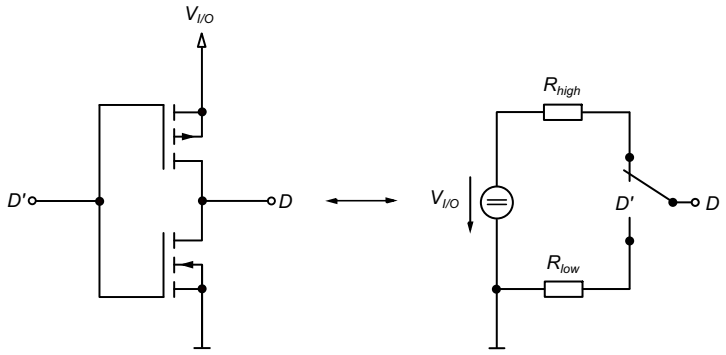

Figure 4.5: FPGA output structure and equivalent circuit.

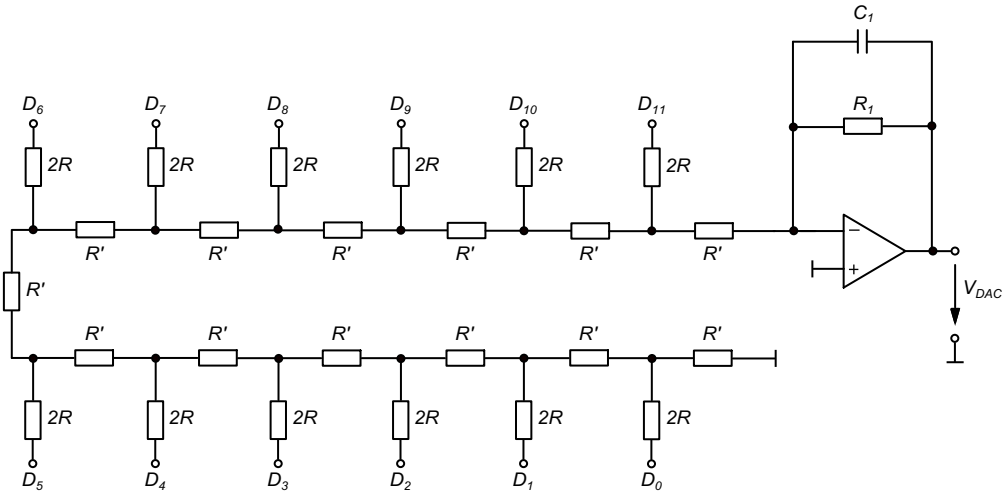

Figure 4.6: Schematic of R-2R DAC network with Q = 12 and inverting amplifier.

p-channel and n-channel MOSFETs have different on-state resistances which, for a constant output current, result in unequal output voltage drops for the high and low state in relation to $V_{I/O}$ and ground, respectively. Consequently, the R_{high} and R_{low} resistances are different in the equivalent circuit in Figure 4.5.

For the implementation, all FPGA output drivers are part of the same interface bank and are supplied with a common voltage. The Complementary Metal-Oxide-Semiconductor (CMOS) 3.3 V interface type has been selected due to its well matching measured output resistances ($R_{high} = 8.62\,\Omega \pm 0.07\,\Omega$ and $R_{low} = 8.23\,\Omega \pm 0.05\,\Omega$) and the advantage of a single interface voltage for the entire FPGA.

A Q-bit R-2R DAC utilizes a network of R and 2R resistors in order to convert the quasi-digital FPGA output voltage signals into an analogue current with the

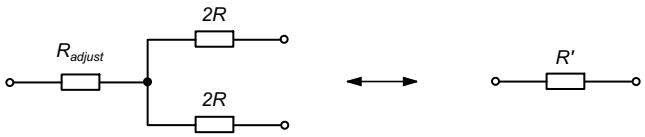

Figure 4.7: Schematic of R-2R DAC FPGA output compensation.

theoretical resolution of 2^Q. The implementation for a resolution of $Q = 12$ bit is shown in Figure 4.6. For the steady state, the signal-to-interference ratio is strongly related to the differential linearity of the DAC and, consequently, to the resistor matching. In principle, resistors with a tolerance better than $1/2^Q$ ensure that the quantization noise dominates spurs caused by non-linearities. E.g. for a 12 bit DAC an overall resistor tolerance better than 0.024 % is required. This is feasible for discrete resistors with space grade[2].

In Figure 4.7, the resistor R' is realized by two 2R resistors in parallel and an additional R_{adjust} in series. The parallel implementation increases the number of required parts, but also enables the use of a single resistor value of a common production lot for all dominating components of the R-2R network. This approach can reduce temperature and long-term drifts in the passive network to a high extent. Additionally, R_{adjust} is dimensioned with approximately 4.21 Ω in order to compensate the mean value of FPGA output resistors R_{high} and R_{low}.

Nevertheless, the steady state performance is not the limiting factor for this application whose main purpose is to generate a sinusoidal signal with accurate frequency. The non-ideal characteristics of the board layout and components can decrease the signal-to-interference ratio significantly. Parasitic capacitors and inductances, e.g. of the connections on the Printed Circuit Board (PCB), in combination with the R and 2R resistors lead to a lowpass characteristic of the network. The switching of quasi-digital FPGA outputs leads to ringing in the analogue output signal. The energy of these transients can be observed as additional harmonics in the frequency domain.

Figure 4.8 shows the dynamic performance of the DAC implementation. The signal-to-interference ratio was measured with two spectrum analyzers[3] for various output frequencies and digital output resolutions. Ultimately, the DAC performance is limited to 73.3 dB at 210 Hz and reduces to 14.8 dB at 2.1 MHz. The programmed digital output resolutions (Q_p) of 10 to 12 bit result in identical performances and lead to overlayed curves in Figure 4.8. The measurements with $Q_p = 9$ bit are slightly better

[2] E.g. the Vishay PHR ESCC 4001/023 qualified high precision thin film chip resistors have a laser trimmed tolerance down to ±0.01%.

[3] Measured with Hewlett-Packard/Agilent spectrum analyzers 3562A and 8562A.

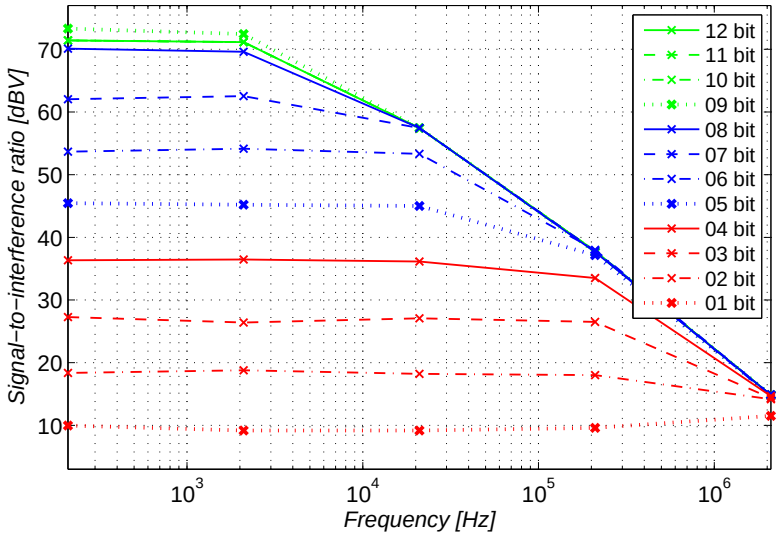

Figure 4.8: Signal-to-interference ratio as a function of frequency and digital resolution.

than with 10 to 12 bit. This could origin from a coincidentally better matching of the involved resistors. The performances for $Q_p = 8$ bit to $Q_p = 1$ bit decrease with approx. 8.5 dB per bit. Figure 4.8 also shows that a resolution (Q) of the R-2R network implementation greater than 5 would not improve the signal-to-interference ratio in the Earth field (e.g. 50000 nT corresponds to approx. $f_B = 1.05$ MHz for $n = \pm 3$). However, $Q = 12$ bit is implemented which enables a more detailed investigation of the measurement principle in low fields.

The amplifier circuit in Figure 4.6 converts and scales the output current of the R-2R network to a voltage. The capacitor C_1 in combination with the feedback resistor R_1 forms a lowpass filter with the corner frequency $f_{-3\,dB} = 2.1$ MHz which is required to suppress the effects of image responses in the output spectrum of the DAC. The resulting FM signal with the magnetic field dependent carrier frequency f_B is fed to the phase modulation input of the phase-lock loop circuit in the microwave generator.

4.1.4 Photodiode, Pre-amplifier and Analogue-to-Digital Converter

The photodiode converts the light power of the incoming amplitude modulated light field into a proportional current. Figure 4.9 shows the equivalent circuit of a photodiode where I_P refers to the photocurrent, R_J to the shunt resistance of the diode junction and C_J to the junction capacitance. The bandwidth of the conversion is mainly limited due to the parasitic capacitance C_J of the diode and the selected

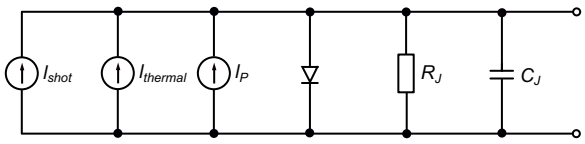

Figure 4.9: Equivalent circuit of a photodiode.

circuit design.

In this application only the DC intensity and those spectral features which are introduced for frequency modulation spectroscopy must be detected. The amplitude variations can be seen as envelope of the overall light field intensity which carries the information of the interaction of the laser field with the rubidium atoms in the sensor cell.

Two dominating sources of noise can be identified in a photodiode. Shot noise is related to the statistical fluctuation caused by the photocurrent and the dark-current. The photocurrent origins in the random creation of electron hole pairs by the photon flux while the dark-current is caused by a random recombination of electrons and holes in the semiconductor. The magnitude of the shot noise can be expressed by

$$I_{shot} = \sqrt{2q(I_P + I_D)\Delta f} \tag{4.1}$$

where $\mathrm{q} = 1.6 \cdot 10^{-19}\,\mathrm{C}$ is the electron charge, I_P is the photo-generated current, I_D is the dark-current and Δf is the considered noise bandwidth. The shunt resistor R_J in a photodetector causes Johnson noise due to the thermal generation of carriers. The magnitude of this noise is

$$I_{thermal} = \sqrt{\frac{4k_B T \Delta f}{R_J}} \tag{4.2}$$

where $\mathrm{k}_B = 1.38 \cdot 10^{-23}\,\mathrm{J/K}$ is the Boltzmann constant, T the absolute temperature in Kelvin, Δf is the noise measurement bandwidth and R_J is the shunt resistance of the photodiode. The total noise current in a photodetector is given by

$$I_{total} = \sqrt{I_{shot}^2 + I_{thermal}^2}\ . \tag{4.3}$$

In spectroscopy, silicon photodiodes are operated in the photoconductive mode and connected to a transimpedance amplifier in order to optimize the signal-to-noise ratio (see Figure 4.10). For experiments with low light intensity, the input current noise density of the amplifier and, consequently, the Johnson noise, limits the SNR of the detection circuit. The output signal voltage is proportional to the transimpedance

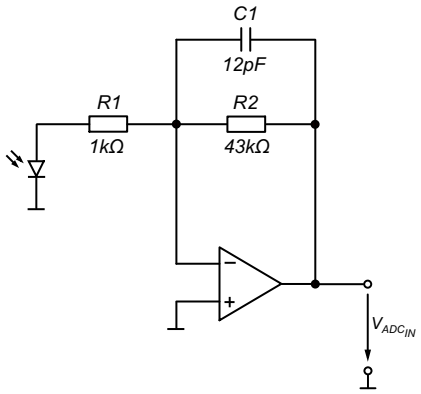

Figure 4.10: Schematics of a single stage transimpedance amplifier circuit.

resistance for frequencies $f \ll f_{-3\,dB}$ while the noise current of the photodetector is amplified by its square root. Consequently, the value of the transimpedance resistor is maximized within limits of the output range of the operational amplifier in order to improve the signal-to-noise ratio.

In practice, the connection pins and printed wires between the photodiode and the operational amplifier span a induction loop. Electro-Magnetic Interferences (EMI) can couple and create an interference voltage. The low resistance of the loop would result in high current interference which would appear as voltage interferences at the circuit output. The additional resistor R_1 in Figure 4.10 reduces these interferences significantly. R_1 has no influence on the photocurrent since $R_j \geq 1\,G\Omega \gg R_1$. The photodetector in Figure 4.10 can be seen as ideal current source for frequencies $f < f_{-3\,dB}$.

The parasitic junction capacitance C_J of the photodiode forms a highpass filter in combination with R_2 (see Figure 4.9 and Figure 4.10). The capacitor C_1 in combination with the transimpedance resistor limits the measurement and the noise bandwidth of the circuit and, additionally, damps the typical increase of noise density of the overall circuit due to this highpass filter (see Figure 4.13).

Amplitude variations are caused by the magnetic field dependent information of the CPT resonances and optical noise disturbances. Both are small compared to the detected constant background light field (e.g. 100 nW rms amplitude of the modulated transmitted laser power in relation to 200 μW background power). Consequently, the photocurrent is a superposition of a DC and an AC with the same ratio.

For a single stage transimpedance amplifier configuration as displayed in Figure 4.10, the value of the feedback resistor R_2 is limited by the DC background

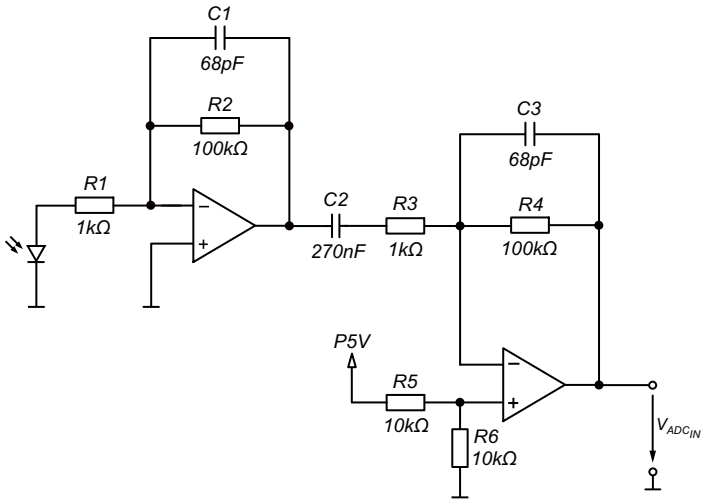

Figure 4.11: Schematics of a two-stage photodiode amplification circuit.

field and the ADC input range. With a maxium intensity of 200 μW, a photodiode sensitivity S of 0.58 A/W[4] and an ADC input range of 5 V, the transimpedance is limited to approx. 43 kΩ. With the resulting amplification factor, the AC component of 100 nW would lead to an output voltage of approx. 2.5 mV_{rms} or 7.1 mV_{pp}. In case of a 12 bit ADC, the maximum digital resolution of the amplitude variations is limited to less than 3 bit.

In order to improve the SNR of the digitized AC component and to avoid high quantization noise resulting from a 3 bit resolution, the photodiode amplification circuit is split into two subunits (see Figure 4.11).

The transimpedance of the first stage was redimensioned to 100 kΩ which leads to a maximum DC output voltage of 11.6 V. Additionally, a second stage amplifier forms an active bandpass filter. Consequently, the DC component and higher frequencies are cancelled while AC components which enable the FM spectroscopy can pass.

In this application, the photodetector shot noise caused by the constant optical background field dominates the noise performance of the overall circuit and limits the SNR of the AC component detection. This shot noise is an inherent physical process associated with the irradiated light power and thus not avoidable. An overall noise of 15.6 mV_{rms} was derived by simulation at the output of the second stage amplifier over the Nyquist frequency of 156.25 kHz of the ADC. The quantization

[4] The sensitivity value refers to the Hamamatsu S3883 Positive Intrinsic Negative (PIN) photodiode which is electrically similar to the target photodiode Micropac 61082-101.

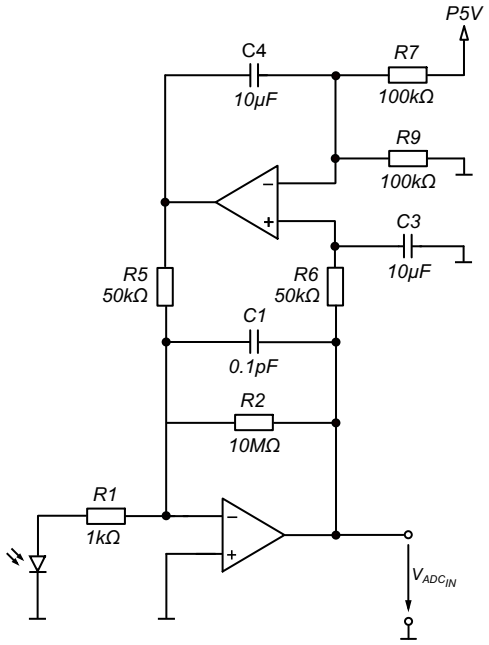

Figure 4.12: Schematics of a transimpedance amplifier with feedback [45].

noise of the ADC can be approximated by [33]

$$N_{ADC} = \frac{q}{\sqrt{12}} \tag{4.4}$$

where q is the voltage step of the Least Significant Bit (LSB). A 12 bit ADC with 5 V full-scale range results in q = 1.22 mV and $N_{ADC} = 0.35\,mV_{rms}$ for frequencies up to the Nyquist frequency of 156.25 kHz. With the selected second stage amplification factor of 100, the overall noise I_{total} of the photodiode circuit dominates the overall noise of the quantized signal[5]. A further increase of the amplification factor would not improve the signal-to-noise ratio.

Investigations in [46] showed that the ratio of the DC and AC components is almost constant for a wide range of overall intensities received at the photodiode. Consequently, a reduction of the overall light intensity would not improve the signal-to-noise ratio of the CPT resonances. There is also a benefit of this fundamental limitation. The requirements on the transimpedance operational amplifier in terms of the unity gain bandwidth are moderate and a less power consuming operational amplifier will not degrade the signal-to-noise ratio.

[5] A margin takes additional AC interferences into account.

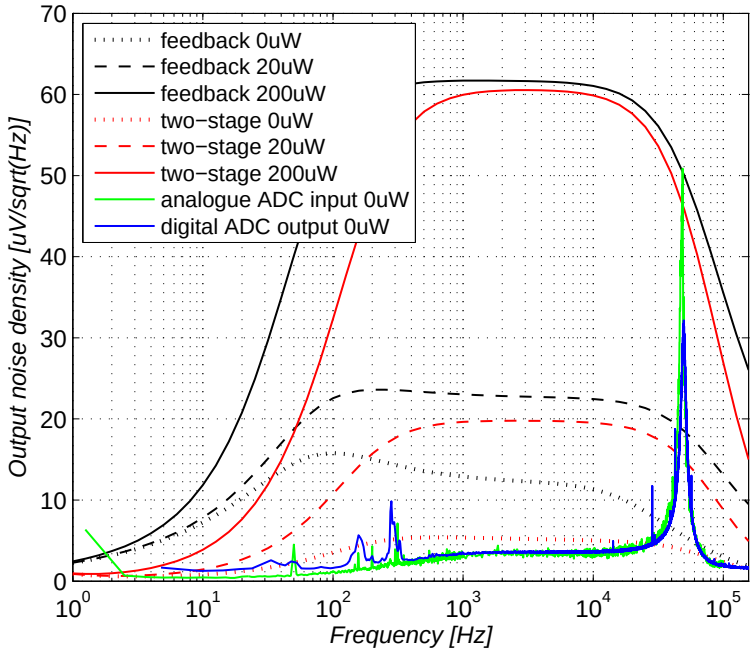

Figure 4.13: Noise performance of circuit designs which contain two amplifiers.

For comparison, an alternative single stage solution derived from [45] and as shown in Figure 4.12 was evaluated with simulation. Here, the transimpedance resistance is not limited by the DC component because an active lowpass filter feeds it back to the inverting amplifier input and compensates it. In steady state the output is solely an AC signal which can be shifted to half of the ADC full-scale voltage in order to fit the ADC input range. Theoretically, the signal-to-noise ratio is higher compared to the two-stage solution of Figure 4.11. This assumption roots in the unequal amplification factor for the signal path and the noise path as discussed above. Nevertheless, this would require a transimpedance resistance of 10 MΩ which is challenging in terms of procurement with space grade. Adverse parasitic capacitors form additional poles and thus reduce the bandwidth of the overall circuit.

Figure 4.13 shows the noise analysis of both circuit designs with two operational amplifiers in different configurations. The black and red lines are derived from simulations of the single stage feedback configuration in Figure 4.12 and the two stage implementation shown in Figure 4.11, respectively. For all three simulated input light intensities 0 μW (dotted), 20 μW (dashed), 200 μW (solid), the two-stage configuration shows better results which can be explained by additional noise which is

introduced by the feedback amplifier. The green and blue lines were measured at the selected and realized two-stage circuit for 0 μW. The green line displays the analogue input of the ADC measured with a spectrum analyser[6], while the blue is the quantized version read by the FPGA. In the range of interest of 1 to 15 kHz, no interferences are visible. The measured noise level is lower than the one derived from the worst case simulation for 0 μW (blue, dotted). The resonance at approximately 49 kHz is caused by the parasitic capacitance C_J of the photodiode.

4.1.5 Lock-in Amplifier

A lock-in amplifier uses a phase sensitive detection technique in order to single out the spectral component of the input signal at a specific reference frequency and phase [47]. As discussed in Section 3.1, the rubidium atoms in the glass cell are excited by $f_{MW} \pm f_B$ and additionally probed by frequency f_{ref_1} which is realized by the FM of the Zeeman frequency f_B (see Section 4.1.2). The lock-in amplifier detects the response of the excited atoms which is contained in periodic variations of the transmitted light (I(t) in Figure 3.1) at the frequency f_{ref_1}.

Figure 4.14 shows the block diagram of the dual-phase lock-in amplifier with diagrams of the time response of different stages to visualize the time delay and phase shift. Additionally, diagrams with a qualitative representation of the frequency responses with noise floors and discrete spectral components are shown.

The frequency reference unit uses the DDS technique as discussed in Section 3.2 in order to generate a sinusoidal signal

$$V_{ref} = B \cdot cos(\omega_{ref} t + \phi_{ref}) \tag{4.5}$$

with the frequency $f_{ref} = \omega_{ref}/(2\pi)$ and the amplitude $-1 \leq B \leq 1-2^{-R}$ where R is the digital width, e.g. 12 bit. An equal amount of input samples in every quadrant of the reference period simplifies the testing of the functional block. With 32 clock cycles for each analogue-to-digital conversion, the possible output frequencies are limited to

$$f_{ref} = \frac{f_{FPGA}}{128 N_{ref}} \quad with \quad N_{ref} \in \mathbb{Z} \geq 1 \tag{4.6}$$

where f_{FPGA} is the clock of the FPGA. The additional reduction of N_{ref} to prime numbers improves the independence of multiple frequency modulation spectroscopy

[6] Measured with Hewlett-Packard/Agilent spectrum analyzer 3562A.

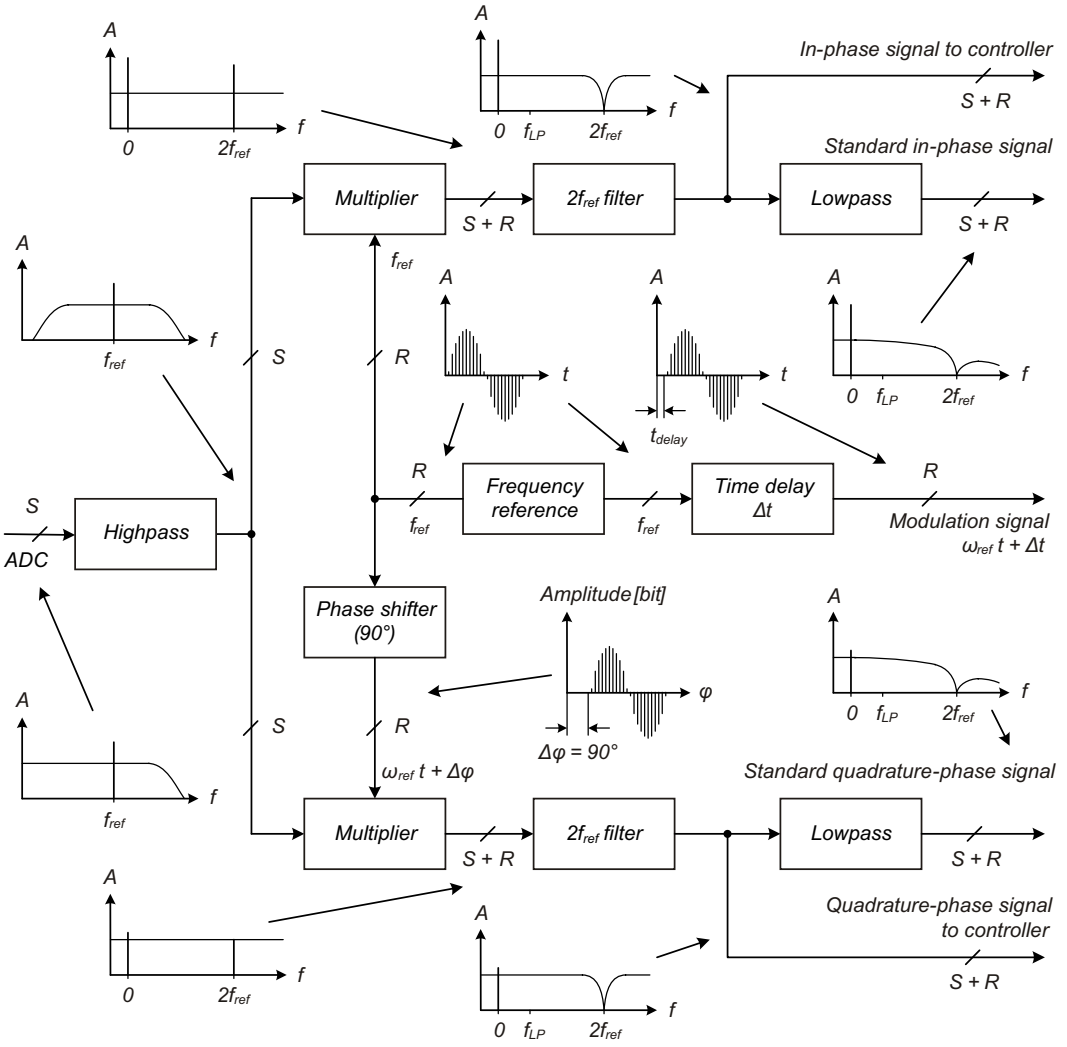

Figure 4.14: Block diagram and characteristic signals of the dual-phase lock-in amplifier.

processes in parallel within the chosen implementation. For the Zeeman control loop, the selected $N_{ref} = 11$ leads to an approximate reference frequency of $f_{ref} = 7102\,\mathrm{Hz}$.

Additionally, a time-delayed version serves as modulation signal for the third modulation of the light field spectrum which is processed in the Zeeman DDS unit (see Section 4.1.2). The delay of this reference signal considers the overall delayed response of the experiment.

In principle, a lock-in amplifier can only process AC signals. In the simplest way, a DC component would introduce noise due to the detection process. More likely, it

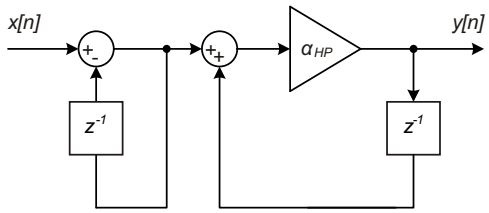

Figure 4.15: Block diagram of the highpass filter implementation.

saturates the fixed point arithmetics of the subsequent function units which would lead to a degradation of the performance or even to a malfunction of the overall system. Consequently, the input signal of the lock-in amplifier is highpass filtered. The transfer function of the implemented first-order Infinite Impulse Response (IIR) filter [33] is given by

$$T_{HP}(z) = \frac{y_{HP}(z)}{x_{HP}(z)} = \frac{\alpha_{HP}(z-1)}{z-\alpha_{HP}} \quad with \quad \alpha_{HP} = \frac{\tau_{HP} f_s}{\tau_{HP} f_s + 1} \tag{4.7}$$

where τ_{HP} refers to the time constant $\tau_{HP} = 1/(2\pi f_{HP})$, f_{HP} to the cut-off frequency and f_s to the sampling frequency of the implementation. The block diagram in Figure 4.15 shows that in total, one adder, one subtractor, one register array and one multiplier are required to enable the highpass characteristic. The multiplier is realized by an additional subtractor and a shifter in order to reduce required resources. This limits the parameter α_{HP} to 1 - $2^{K_{HP}}$ with $K_{HP} \in \mathbb{Z} < 0$.

The parameter K_{HP} can be commanded in operation from -16 (blue) to -8 (green) which leads to corner frequencies between approx. 0.8 Hz and 195 Hz (see Figure 4.16).

In the multiplier, the remaining AC input signal (S = 12 bit)

$$V_{in} = A \cdot cos(\omega_{in} t + \phi_{in}) \tag{4.8}$$

is mixed with reference signal V_{ref} (R = 12 bit). This process can be interpreted as phase sensitive detection. The output consists of two AC signals, one at the frequency difference ω_{in} - ω_{ref} and the other at the frequency sum ω_{in} + ω_{ref}, which can be written as

$$\begin{aligned} V_X = V_{in} \cdot V_{ref} \propto \\ \frac{AB}{2} cos((\omega_{in} - \omega_{ref})t - (\phi_{in} - \phi_{ref})) - \\ - \frac{AB}{2} cos((\omega_{in} + \omega_{ref})t - (\phi_{in} + \phi_{ref})) \,. \end{aligned} \tag{4.9}$$

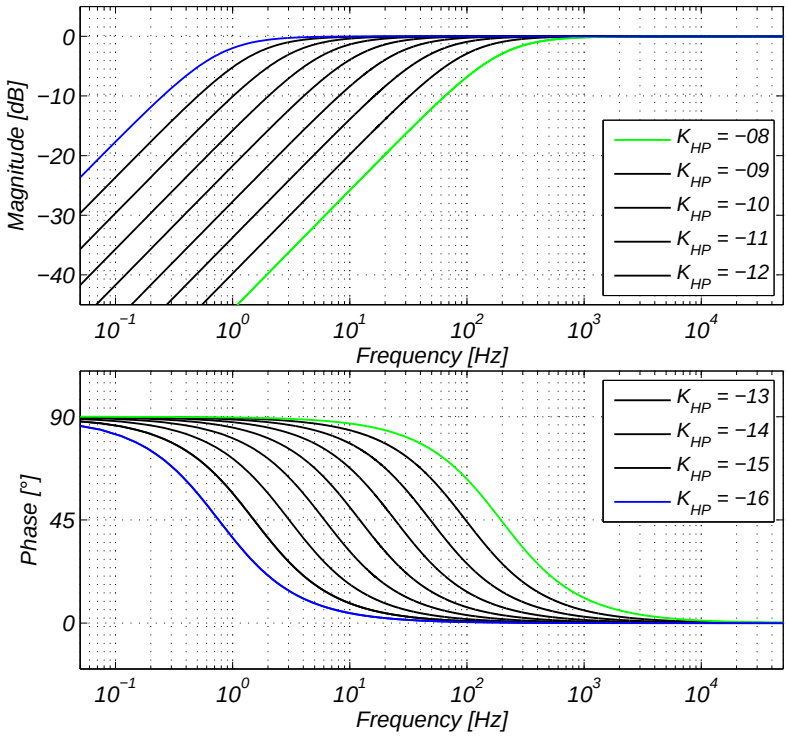

Figure 4.16: Bode diagram of the highpass filter for different K_{HP}.

If $\omega_{in} = \omega_{ref} = \omega$, the expression can be reduced to

$$V_X = V_{in} \cdot V_{ref} \propto \frac{AB}{2} cos(\phi_{in} - \phi_{ref}) - \frac{AB}{2} cos((2\omega_{ref})t - (\phi_{in} + \phi_{ref}))\,. \quad (4.10)$$

The amplitudes of the resulting components at DC and $2\omega_{ref}$ are proportional to the amplitudes of the input signal V_{in} and the reference signal V_{ref} and their phase difference $\phi = \phi_{in} - \phi_{ref}$.

If $\phi_{ref} = \phi_{in}$, the output signal reaches its maximum. Consequently, if the phase difference $\phi = \phi_{ref} - \phi_{in} = \pm 90°$, there is no output at all. This phase dependence can be eliminated by adding a second phase sensitive detector, whose frequency reference is phase-shifted by 90°. Analogue to Equations 4.9 and 4.10 the output of the additional detector can be expressed by

$$V_Y = V_{in} \cdot V_{ref} \propto \frac{AB}{2} sin((\omega_{in} - \omega_{ref})t - (\phi_{in} - \phi_{ref})) - \frac{AB}{2} sin((\omega_{in} + \omega_{ref})t - (\phi_{in} + \phi_{ref})) \tag{4.11}$$

and

$$V_Y = V_{in} \cdot V_{ref} \propto \frac{AB}{2} sin(\phi_{in} - \phi_{ref}) - \frac{AB}{2} sin((2\omega_{ref})t - (\phi_{in} + \phi_{ref}))\,. \tag{4.12}$$

Consequently, a dual-phase lock-in amplifier provides two signals. The V_X or in-phase component is proportional to the cosine of ϕ, while the output V_Y scales with the sine of ϕ and represents the quadrature-phase component.

A subsequent $2\,f_{ref}$ filter cancels spectral components at $f = M_{2f_{ref}} \cdot 2\,f_{ref}$ with $M_{2f_{ref}} \in \mathbb{Z} \geq 2$. It is implemented as Finite Impulse Response (FIR)[7] moving average filter with $N_{2f_{ref}}$ stages which is defined by

$$N_{2f_{ref}} = 2\,N_{ref}\,. \tag{4.13}$$

The transfer function of the filter can be expressed by

$$T_{2f_{ref}}(z) = \frac{y_{2f_{ref}}(z)}{x_{2f_{ref}}(z)} = \frac{z^{-1} + z^{-2} + ... + z^{-N_{2f_{ref}}}}{N_{2f_{ref}}} \tag{4.14}$$

The parameter $N_{2f_{ref}}$ can be commanded in operation from 4 (green) to 32768 (blue) which leads to first notch frequencies between 78125 Hz and approx. 10 Hz (see Figure 4.17). For the Zeeman control loop $N_{2f_{ref}}$ is 22. This leads to an implementation with 22 registers and a first frequency notch at approx. $f = 2\,f_{ref} = 14205$ Hz.

In a typical lock-in amplifier application, the output is filtered by an additional digital lowpass [47]. The phase sensitive detector in combination with this filter detects only signals whose frequencies are very close to the reference frequency f_{ref}. Noise frequencies far from the reference are attenuated by the lowpass filter. The attenuation depends on the lowpass filter bandwidth and roll-off. A narrow bandwidth removes noise sources very close to the reference frequency while a wider bandwidth allows these signals to pass. Only signals at the reference frequency result in a DC output.

[7] An implementation based on FIR is a simple way to realize adjustable moving average filters [33].

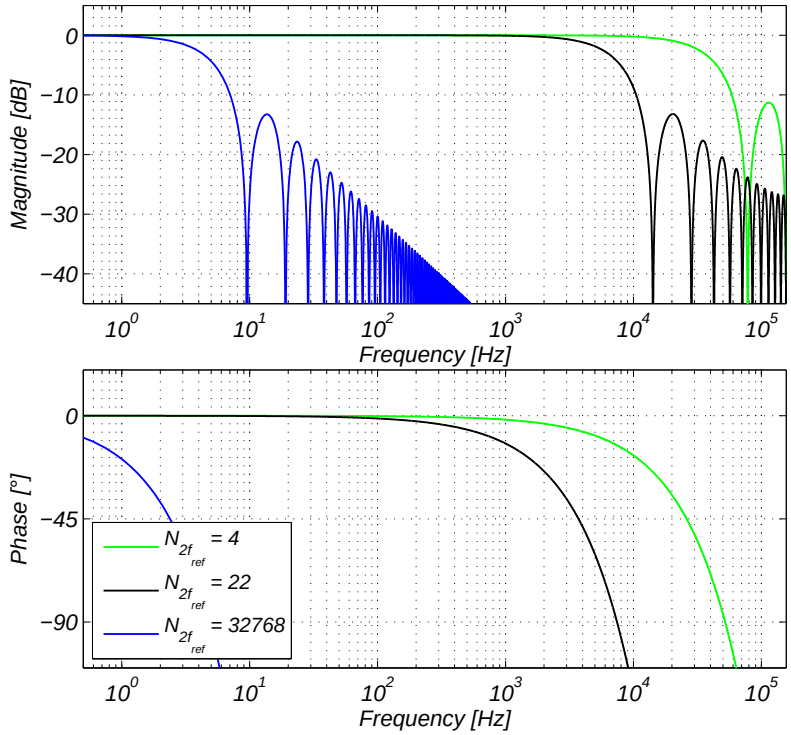

Figure 4.17: Bode diagram of the moving average filter for different $N_{2f_{ref}}$.

For the CDSM, the lock-in amplifier is used in this typical implementation in order to obtain in-phase and quadrature-phase output signals for sweeps of e.g. the Zeeman frequency over the CPT resonance features. The transfer function of the implemented first-order IIR lowpass filter [33] is given by

$$T_{LP}(z) = \frac{y_{LP}(z)}{x_{LP}(z)} = \frac{\alpha_{LP} \cdot z}{z - 1 + \alpha_{LP}} \quad with \quad \alpha_{LP} = \frac{1}{\tau_{LP} f_s + 1} \tag{4.15}$$

where τ_{LP} refers to the time constant $\tau_{LP} = 1/(2\pi f_{LP})$, f_{LP} to the cut-off frequency and f_s to the sampling frequency of the implementation. The block diagram in Figure 4.18 shows that overall two adders, one register array and one multiplier are required. Similar to the highpass filter, the multiplier is realized by a shifter in order to reduce the required resources. This limits the parameter α_{LP} to $2^{K_{LP}}$ with $K_{LP} \in \mathbb{Z} < 0$.

Similar to the highpass implementation, the parameter K_{LP} can be commanded in operation from -19 (blue) to -8 (green) which leads to corner frequencies between approximately 0.1 Hz and 195 Hz (see Figure 4.19).

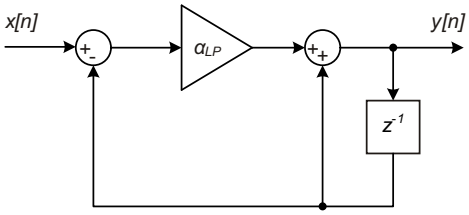

Figure 4.18: Block diagram of the lowpass filter implementation.

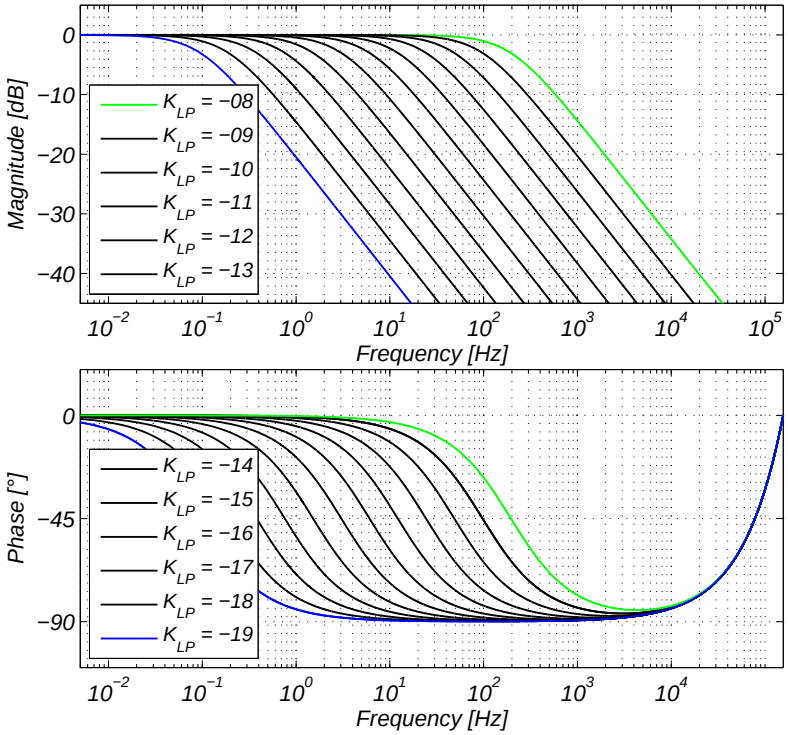

Figure 4.19: Bode diagram of the lowpass filter for different K_{LP}.

For the closed loop, the controller discussed in Section 4.1.6 acts as lowpass filter and no additional lowpass filter as discussed above is required. Therefore, the output of the $2\,f_{ref}$ filter is directly provided to the controller functional block (see Figure 4.14).

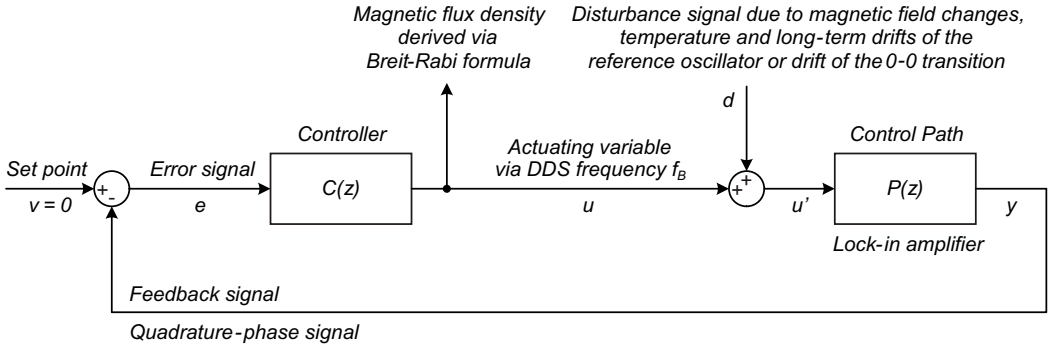

Figure 4.20: Block diagram of the Zeeman control loop.

4.1.6 Controller

Figure 4.20 shows the block diagram of the control loop structure, control theory relevant parameters and their physical equivalents. Changes of the external magnetic field are detected by the excited rubidium atoms inside the glass cell and can be interpreted as a disturbance signal of the closed control loop. The set point is fixed to zero in order to track the zero passage of the quadrature-phase of the lock-in amplifier and, consequently, the dispersion signal of the CPT resonance (see Figure 3.2). The Zeeman DDS output frequency f_B is the actuating variable and is a direct measure of the magnetic flux density via the Breit-Rabi formula (see Equation 2.1).

For a standard lock-in amplifier implementation, the transfer function of the control path $P_s(z)$ can be written as

$$P_s(z) = \frac{y_s(z)}{u'_s(z)} = P_{2f_{ref}}(z) \cdot P_{LP}(z) \tag{4.16}$$

where $y_s(z)$ refers to the feedback signal, $u'_s(z)$ to the disturbed actuating variable, $P_{2f_{ref}}$ to the transfer function of the $2f_{ref}$ filter and P_{LP} to the transfer function of the lowpass filter of the lock-in amplifier (see Section 4.1.5). For most applications, $\tau_{LP} \gg \tau_{2f_{ref}}$ is valid and τ_{LP} is the dominating time constant of the control path. In this case, the transfer function can be simplified to

$$P_s(z) = \frac{y_s(z)}{u'_s(z)} = P_{LP}(z)\,. \tag{4.17}$$

Since the target time constant of the closed control loop $\tau_T \approx \tau_{LP}$, τ_{LP} would need to be compensated by the controller in order to enable a first-order frequency response of the overall control loop. Otherwise, the lowpass filter P_{LP} and the integrator of

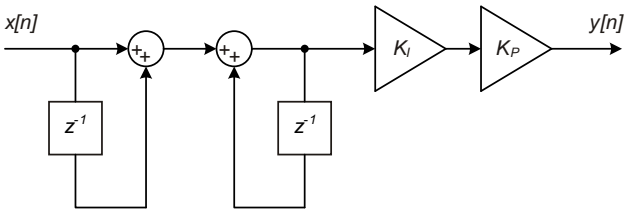

Figure 4.21: Block diagram of the Zeeman controller.

the controller C_I would form a second-order frequency response and would push the loop dynamics towards the limit of the stability region [33].

For the reduced lock-in amplifier implementation as discussed in Section 4.1.5, the transfer function of the control path can be written as

$$P_r(z) = \frac{y_r(z)}{u'_r(z)} = T_{2f_{ref}}(z) \tag{4.18}$$

where $\tau_{2f_{ref}}$ is the time constant of the $2f_{ref}$ filter. Since $\tau_T \approx \tau_{LP} \ll \tau_{2f_{ref}}$, the control path can be simplified to

$$G_r(z) = \frac{y_r(z)}{u'_r(z)} = 1 \quad for \quad \tau_T \gg \tau_{2f_{ref}} \,. \tag{4.19}$$

For a closed loop and $\tau_T \ll \tau_{2f_{ref}}$, the bandwidth of the frequency modulation spectroscopy and, consequently, the noise bandwidth of the measurement, which in a typical application is defined by the lowpass filter of the lock-in amplifier, can be simply determined by the transfer function of the controller.

A first-order characteristic similar to the lowpass filter of the standard lock-in amplifier implementation in Section 4.1.5 can be realized by an integrator $C_I(z)$,

$$C_I(z) = \frac{u_r(z)}{e_r(z)} = K_I \cdot \frac{z+1}{z-1} \quad with \quad K_I = \frac{1}{2f_s\tau_I} \tag{4.20}$$

where f_s is the sampling frequency and τ_I is the time constant of the integrator and, consequently, of the closed control loop.

The block diagram in Figure 4.21 shows that overall two adder, two register arrays and one multiplier are required for the integrator. The multiplication is realized by a shifter in order to reduce required resources. This limits the factor K_I to 2^{N_I} with $N_I \in \mathbb{Z}$. The parameter N_I can be commanded in operation from -24 (blue) to -10 (green) which leads to corner frequencies between approximately 6 mHz and 97 Hz (see Figure 4.22). The final controller C(z) is given by

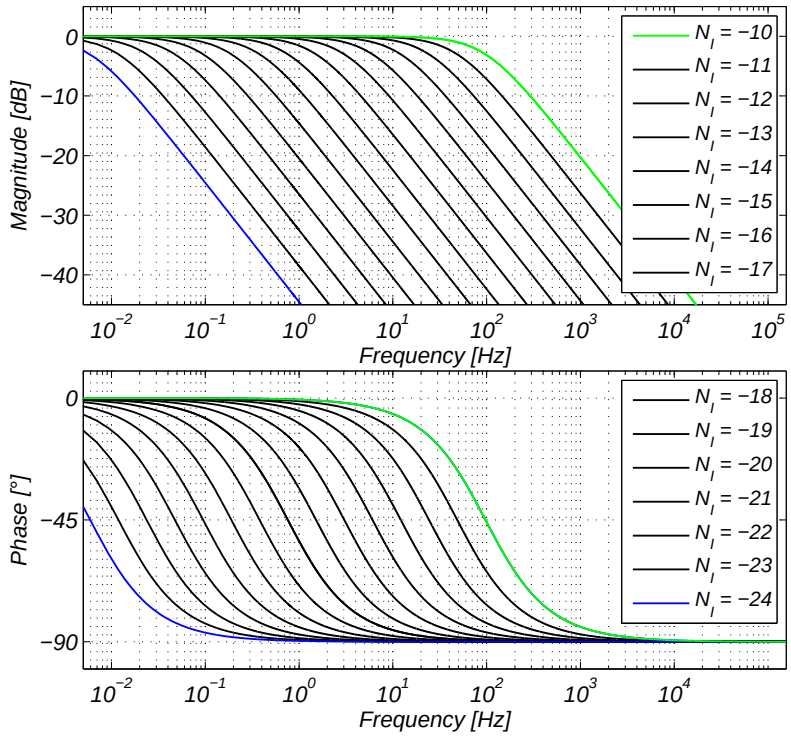

Figure 4.22: Bode diagram of the closed Zeeman control loop.

$$C(z) = \frac{u_r(z)}{e_r(z)} = K_P \cdot C_I(z)\,. \tag{4.21}$$

where the additional factor K_P compensates the slope of the quadrature-phase signal component of the CPT resonance at the zero crossing and sets the loop gain to one.

4.1.7 Processing of Vector Magnetometer Data

In scientific space missions, fluxgate magnetometers provide the x_f-, y_f- and z_f-components of the magnetic flux density which are orthogonalized and shown in braces in Figure 4.23. In a spherical coordinate system with identical reference point, the radial distance r is equivalent to the magnitude B while the polar angle Θ refers to the angle between the magnetic field and the light field. Consequently, the fluxgate data can be transferred into spherical coordinates to gain information about the angle Θ and the magnitude B in order to ensure the CDSM operation in all directions of the

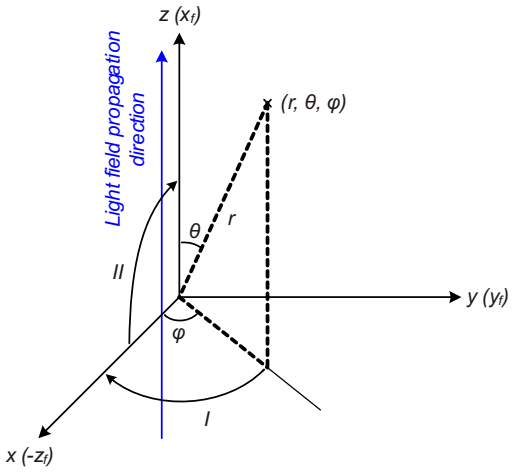

Figure 4.23: Transformation of Cartesian to the spherical coordinate system.

magnetic field and to rapidly find the CPT resonances at start-up (see Section 4.1.1).

The typical Full Width of Half Maximum (FWHM) linewidth of CPT resonance superpositions in the current setup is approximately 2 kHz which is equivalent to 95 nT for n = ±3. For a reliable operation of the CDSM, the magnitude of the magnetic flux density calculated of fluxgate components x_f, y_f and z_f should have an absolute error of less than 30 nT. The magnitude can be written as

$$B_f = \sqrt{(x + x_e)^2 + (y + y_e)^2 + (z + z_e)^2} \tag{4.22}$$

where x, y and z refer to the actual magnetic field and x_e , y_e and z_e to error components. With the worst case assumption x = y = z and $x_e = y_e = z_e$, it can be simplified to

$$B_f = B + B_e = \sqrt{3}\,(x + x_e) \tag{4.23}$$

which leads to a single component error of the fluxgate of

$$x_e = \frac{B_e}{\sqrt{3}} = \frac{30}{\sqrt{3}} \approx 17\,nT\,. \tag{4.24}$$

Consequently, the fluxgate magnetometer should provide the x_f-, y_f- and z_f-components of the magnetic flux density within an absolute error of 17 nT each in order to ensure a correct detection of the CPT resonances.

Spherical coordinates of the fluxgate data can be calculated by a two-stage transformation. Each stage can be implemented as a rotation of one Cartesian coordinate

axis into another one by applying e.g. CORDIC algorithms. These type of algorithms have been first published by *Volder* in 1959 [44] and allow an efficient implementation of functions with digital signal processing.

Typically, the x_f- and y_f-axes are defined in the sensor mounting plane. For the CDSM sensor unit, the z-axis has been selected as the laser propagation direction. In order to fit the Cartesian coordinates system to the common nomenclature of spherical coordinate systems the coordinates are transferred by

$$\begin{bmatrix} x \\ y \\ z \end{bmatrix} = \begin{bmatrix} 0 & 0 & -1 \\ 0 & 1 & 0 \\ 1 & 0 & 0 \end{bmatrix} \begin{bmatrix} x_f \\ y_f \\ z_f \end{bmatrix} \tag{4.25}$$

into a second Cartesian coordinate system denoted by x, y, and z in Figure 4.23. In a first CORDIC process the transformed y-axis is rotated into the x-axis (I). The iterative rotation of a CORDIC vector $(x_c^{(i)}, y_c^{(i)})^T$ by an angle α_i in order to obtain $(x_c^{(i+1)}, y_c^{(i+1)})^T$ is given by

$$\begin{bmatrix} x_c^{(i+1)} \\ y_c^{(i+1)} \end{bmatrix} = \begin{bmatrix} cos\alpha_i & -sin\alpha_i \\ sin\alpha_i & cos\alpha_i \end{bmatrix} \begin{bmatrix} x_c^{(i)} \\ y_c^{(i)} \end{bmatrix} \tag{4.26}$$

which can be rewritten as

$$\begin{bmatrix} x_c^{(i+1)} \\ y_c^{(i+1)} \end{bmatrix} = cos\alpha_i \begin{bmatrix} 1 & -tan\alpha_i \\ tan\alpha_i & 1 \end{bmatrix} \begin{bmatrix} x_c^{(i)} \\ y_c^{(i)} \end{bmatrix} . \tag{4.27}$$

In case $\tan\alpha_i$ is selected to $d_i 2^{-i}$, with $d_i = \pm 1$, the rotation can be implemented without multiplications except for the factor

$$cos\alpha_i = \frac{1}{\sqrt{1 + 2^{-2i}}} \tag{4.28}$$

which is solely a function of the number of iterations N, with $0 < i \leq N$. For the rotation over an arbitrary angle α, with $-\frac{\pi}{2} \leq \alpha \leq \frac{\pi}{2}$, the angle can be decomposed to

$$\alpha = \sum_{i=0}^{N} d_i \, arctan\, 2^{-i} \tag{4.29}$$

where $d_{i+1} = \pm 1$ for $z_c^{(i)} \geq 0$ or $d_{i+1} = -1$ for $z_c^{(i)} < 0$ (see Equations 4.30). The factor $\arctan 2^{-i}$ can be pre-calculated and stored in the look-up table. This leads to the general CORDIC equations

$$\begin{aligned} x_c^{(i+1)} &= x_c^{(i)} - d_i 2^{-i} y_c^{(i)} \\ y_c^{(i+1)} &= d_i 2^{-i} x_c^{(i)} + y_c^{(i)} \\ z_c^{(i+1)} &= z_c^{(i)} - d_i l(i)\,. \end{aligned} \tag{4.30}$$

For the applied vectoring-mode and with the initial values $x_c^{(0)} = x$, $y_c^{(0)} = y$ and $z_c^{(0)} = 0$, the iterative calculations result in

$$\begin{aligned} x_c^{(N)} &= K\sqrt{x^2 + y^2} = x' \\ y_c^{(N)} &= 0 \\ z_c^{(N)} &= arctan(\frac{y}{x}) \end{aligned} \tag{4.31}$$

where $K = \prod_{i=1}^{N} \sqrt{1 + 2^{-2i}}$ and d_i is a function of $y_c^{(i)}$: $d_i = 1$ for $y_c^{(i)} \leq 0$ or $d_i = -1$ for $y_c^{(i)} > 0$. Consequently, the initial vector $(x_c^{(i)}, y_c^{(i)})^T$ has been rotated onto the x-axis and scaled with the factor K to gain the value x'.

The new CORDIC vector $(x_c^{(i)}, y_c^{(i)})^T$ is rotated onto the z-axis by a second iterative rotation (II) with the initial values $x_c^{(0)} = z$, $y_c^{(0)} = x'$ and $z_c^{(0)} = 0$. It is scaled with same factor K since the number of iterations for both rotations is set equal. The iterative calculations result in

$$\begin{aligned} x_c^{(N)} &= K\sqrt{z^2 + x'^2} = B \\ y_c^{(N)} &= 0 \\ z_c^{(N)} &= arctan(\frac{x'}{z}) = \theta \end{aligned} \tag{4.32}$$

where the value of $x_c^{(N)}$ in Equation 4.32 correspond to the magnitude of the magnetic flux density B while the value of $z_c^{(N)}$ is the angle θ between the magnetic field and light propagation direction in the sensor.

4.2 Control Loops to Track Fine Structure Transition

In order to excite the fine structure splitting transition $5^2S_{1/2} \rightarrow 5^2P_{1/2}$ of the rubidium D1 line in Figure 2.1, energy of a light field with the wavelength $\lambda_{FS} = \lambda_{VCSEL} = 794.979\,\text{nm}$ is required. The wavelength in the Near Infra-Red (NIR) region can be established by a VCSEL diode. The vertical cavity of VCSELs has the characteristic of low parasitic capacity and therefore can be modulated by microwave signals with good efficiency [48]. Furthermore, VCSELs have inherent single mode capability [48].

Without control of the laser carrier frequency, the entire triple modulated light field spectrum, which is applied in order to excite and detect the magnetic field dependent Zeeman resonances, would drift. This would cause a so-called two-photon detuning [49] of the CPT resonance excitation process and would lead to a malfunction of the magnetometer. The optical transition $5^2S_{1/2} \rightarrow 5^2P_{1/2}$ of the rubidium D_1 line has typically a Doppler broadened FWHM of 600 MHz. For a reliable operation of the CDSM, the laser frequency must fit within a tolerance of < 100 MHz. The VCSEL frequency is strongly related to the DC injection current and to the temperature via the frequency and temperature shifting coefficients 340 GHz/mA and 34 GHz/K (@ $\lambda_{VCSEL} = 794.979$ nm), respectively[8]. Consequently, both parameters must be controlled precisely as it is discussed for the laser temperature in Section 4.2.1 and for the laser injection current in Section 4.2.2.

4.2.1 Control Loop to Set Laser Temperature

The laser temperature control loop is established in order to set the temperature of the VCSEL diode, that in combination with the laser injection current directly influences the output frequency. In Section 4.2.1.1, a general overview of the control loop design is given. Section 4.2.1.2 to Section 4.2.1.5 discuss in detail the function blocks which are part of the control unit.

4.2.1.1 Overview

The temperature of the VCSEL diode is set by a bi-directional current through a Thermo-Electric Cooling (TEC) element (see Figure 4.1). According to the thermo-electric effect in conductors, the current through the TEC element cools down one side of the module while the other is heated up. A reverse current leads to a change of the direction of the heat flow through the TEC element. The current strength and direction are set by dual Pulse Width Modulation (PWM), generated in the FPGA and discussed in Section 4.2.1.2.

The PWM signals are amplified by an output structure on the electronics board and drive the TEC element located in the laser unit. Two options of possible output structures are compared in terms of efficiency in Section 4.2.1.3.

The laser temperature is monitored by a Negative Temperature Coefficient (NTC) resistor. Both the TEC element and the NTC resistor are thermally coupled to the laser diode. The temperature measurement circuit and the ADC are discussed in

[8] The frequency and temperature shifting coefficients are values obtained from the ULM photonics 795 nm single mode VCSEL diode datasheet, v4.

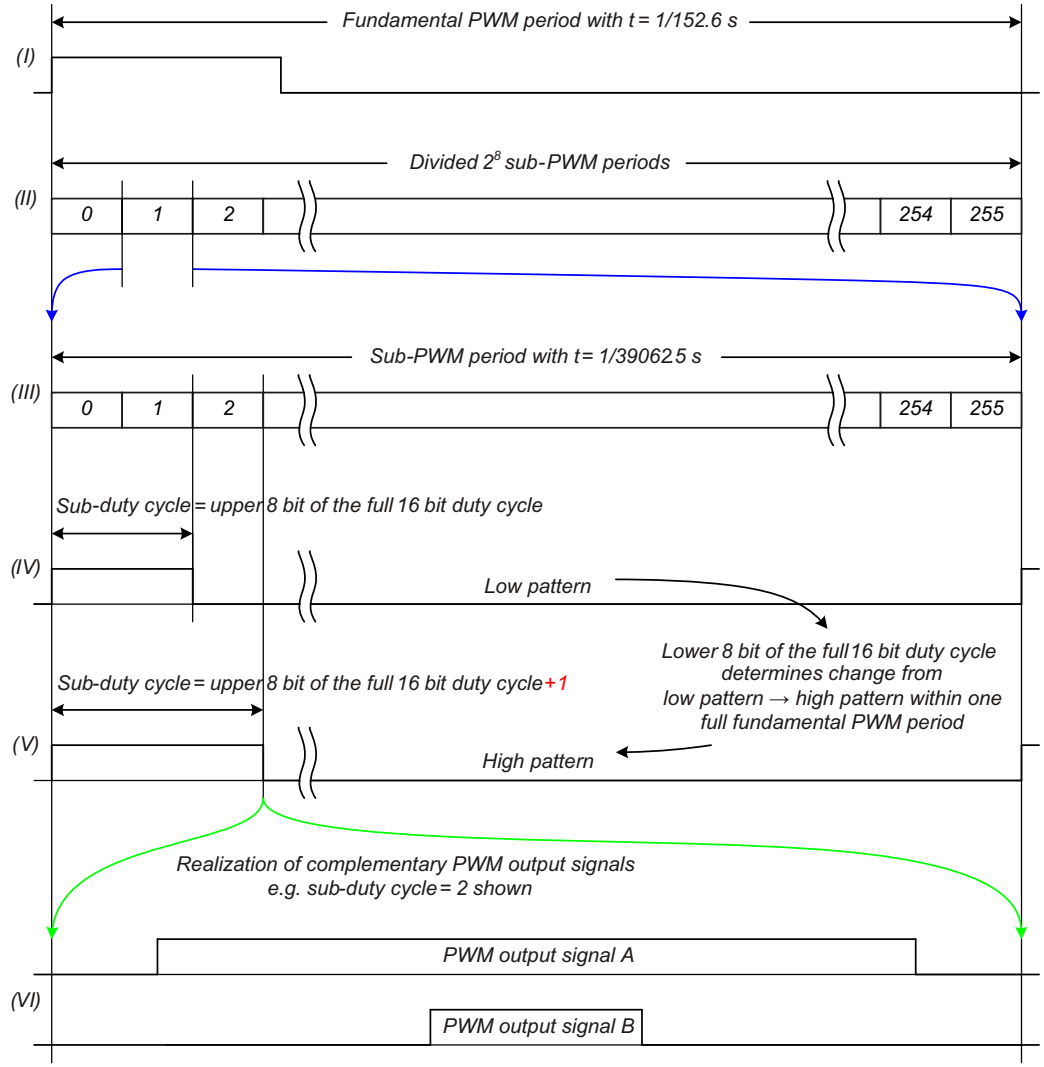

Figure 4.24: Different stages of the PWM pattern generation.

Section 4.2.1.4. The quantized signal is fed to the laser temperature controller which calculates the duty cycle required to keep the actual VCSEL temperature at the set temperature.

4.2.1.2 Synthesis of Duty Cycle

The PWM should not disturb the magnetic field measurement or other function blocks of the instrument. Frequencies below 30 Hz are of interest for the magnetic

field measurement. Modulation frequencies from 1000 Hz to 30000 Hz are typically used for the overall three lock-in amplifiers in order to phase-sensitively detect optical resonance features in the experiment. Hence, the fundamental frequency of the PWM is set to approximately 152.6 Hz whose period is equivalent to 2^{16} clock cycles of the FPGA clock frequency $f_{FPGA} = 10$ MHz (see (I) in Figure 4.24). Consequently, the resolution of the PWM word is 16 bit. However, for this frequency regime, the design and implementation of power supply filters would be challenging in terms of mass and PCB area.

In order to enable a more frequent output switching and preserve the high resolution of the initial PWM word, the 16 bit fundamental PWM period is divided into 2^8 segments which act as sub-PWM periods with a resolution of 8 bit each (see (II) and (III) in Figure 4.24). At the start of a fundamental PWM period, the duty cycle of the sub-PWMs is set by the higher 8 bit of the 16 bit PWM word (see (IV) in Figure 4.24). The low 8 bit of the 16 bit PWM word in combination with a segment counter decides at which segment of the fundamental PWM period the duty cycle of the sub-PWMs is incremented by one (IV and V). This technique combines a high PWM resolution of 16 bit and a high frequent PWM output switching with a defined sub-fundamental at 39062.5 Hz. The sub-fundamental frequency is beyond the frequency range of the lock-in amplifiers.

Within one sub-PWM period, the PWM signals A and B are switched complementary and symmetric to half of the period (VI). This minimizes synchronous switching events of signal A and signal B and, consequently, the EMI on the power supply.

4.2.1.3 Output Structure

The signals A and B of the dual PWM are amplified by a dual MOSFET driver on the electronics board (see Figure 4.25).

For option 1, the TEC element is directly connected to the driver. If the PWM signals A and B are both high or low, the terminals of the TEC are at the same potential and no current flows. In case of signal A is low and signal B is high, the current through the TEC module e.g. heats the laser diode while the mounting plate on the other side of the element is cooled. For steady state, the maximal electrical power $P_{TEC_{max}}$ in the TEC element can be expressed by

$$P_{TEC_{max}} = R_{TEC} \cdot I^2_{TEC_{max}} \tag{4.33}$$

where R_{TEC} refers to the resistance of the TEC element and $I_{TEC_{max}}$ to the maximum TEC current which is determined by the supply voltage of the MOSFET drivers

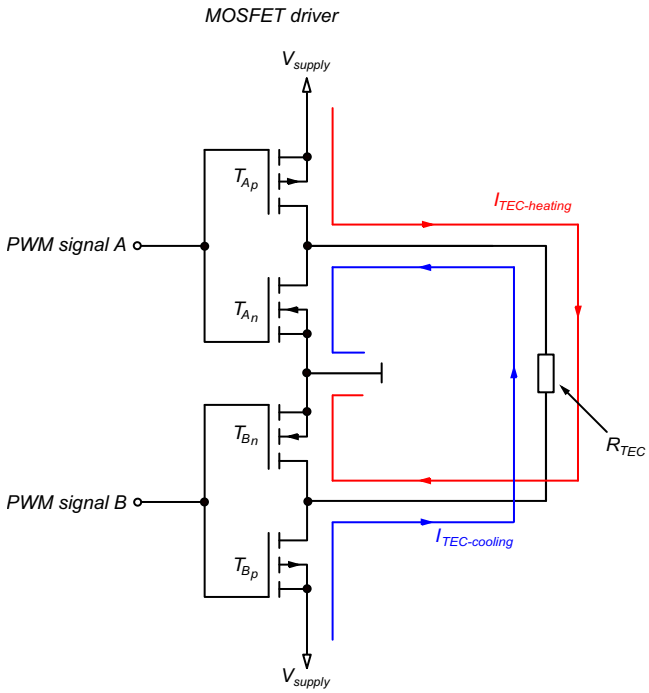

Figure 4.25: Simple laser temperature output structure (option 1).

and the series resistance of all elements in the current path of I_{TEC}. For option 1, that includes the on-resistances R_{A_p} and R_{B_n} of the p-channel and n-channel MOSFETs of the drivers A and B, respectively, the resistance R_w of the wires and connectors which interface the laser unit and R_{TEC}. The resistance of the current path of I_{TEC} for heating, R_{h_1}, can be written as

$$R_{h_1} = R_{A_p} + \frac{1}{2}R_w + R_{TEC} + \frac{1}{2}R_w + R_{B_n}\,. \tag{4.34}$$

In case of the PWM signal A is high and signal B is low, the current through the TEC element is reversed and cools the laser. Analogue to Equation 4.34, the cooling resistance for option 1 can be expressed by

$$R_{c_1} = R_{A_n} + \frac{1}{2}R_w + R_{TEC} + \frac{1}{2}R_w + R_{B_p} \tag{4.35}$$

where R_{A_n} and R_{B_p} refer to the on-resistances of the n-channel and p-channel MOS-FETs of the drivers A and B, respectively.

For option 2, two additional MOS-FET Totem Pole (TP) output structures A and B are introduced in order to drive the TEC element. The overall resistances for

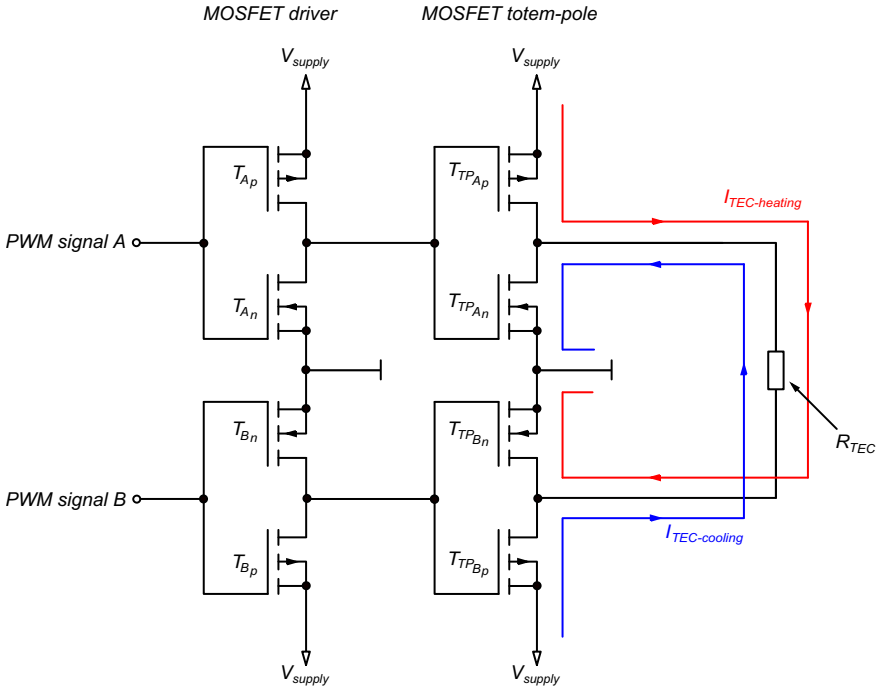

Figure 4.26: Advanced laser temperature output structure (option 2).

heating and cooling can be written as

$$R_{h_2} = R_{TP_{A_p}} + \frac{1}{2}R_w + R_{TEC} + \frac{1}{2}R_w + R_{TP_{B_n}} \tag{4.36}$$

and

$$R_{c_2} = R_{TP_{A_n}} + \frac{1}{2}R_w + R_{TEC} + \frac{1}{2}R_w + R_{TP_{B_p}} \tag{4.37}$$

where $R_{TP_{A_p}}$ and $R_{TP_{B_n}}$ refer to the on-resistances of the p-channel and n-channel MOSFETs of the totem poles A and B in case of heating, while $R_{TP_{A_n}}$ and $R_{TP_{B_p}}$ are the on-resistances of the n-channel and p-channel MOSFETs of totem poles A and B in case of cooling.

Figure 4.27 shows calculations of the overall power consumption of the output structures (upper plot, dashed lines), the electrical power dissipation in the TEC element (upper plot, solid lines) and the power efficiency (lower plot) for output structure option 1 (blue) and option 2 (green). The resistances of wires and connectors are

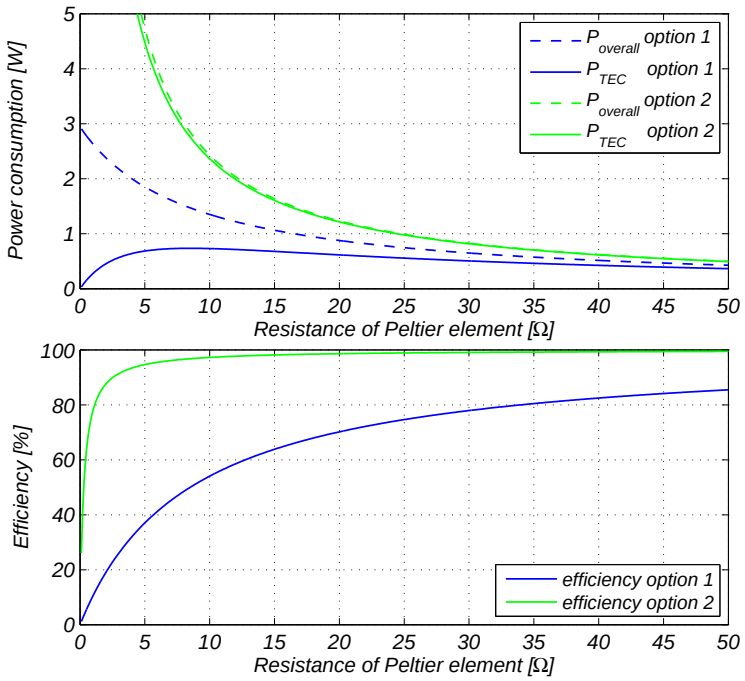

Figure 4.27: Laser temperature output structure power consumption and efficiency.

neglected for these calculations[9] For option 1, the selected dual MOSFET driver[10], operated at $V_{supply} = 5\,V$, limits the electrical power at the TEC element to approximately 740 mW with an efficiency of 50 % ($R_{TEC} = 8.5\,\Omega$). The additional MOSFET totem poles in option 2 have lower on-resistances[11] which increase the maximal electrical power at the TEC and improve efficiency of the overall circuit. E.g. an electrical TEC power of 1 W can be realized with a TEC resistance of $R_{TEC} = 24.4\,\Omega$ and with an efficiency of 98.85 %.

[9] The wire and connector resistances are much smaller than R_{TEC}. E.g. 0.25 Ω/m obtained from datasheet for a space-qualified GORE wire or $< 0.01\,\Omega$ obtained from datasheet for a LEMO 00 series connector.

[10] E.g. $R_{A_p}, R_{B_p} = 4.5\,\Omega$ and $R_{A_n}, R_{B_n} = 4\,\Omega$ obtained from datasheet for Micrel MIC4424 dual MOSFET driver.

[11] E.g. $R_{TP_{A_p}}, R_{TP_{A_n}} = 0.219\,\Omega$ obtained from datasheet for a p-channel MOSFET 2SJ1A06 and $R_{TP_{A_n}}, R_{TP_{B_n}} = 0.064\,\Omega$ obtained from datasheet for a n-channel MOSFET 2SK4219.

Table 4.1: Parameters of the laser temperature measurement.

	Temperature (°C)	R_{NTC} (Ω)	V_{NTC} (V)	V_{ADC} (V)
Lower limit	31.4	7875	2.67	5
Nominal	35.2	6859	2.50	2.5
Upper limit	38.9	6010	2.34	0

4.2.1.4 Temperature Measurement

The temperature of the laser diode is measured with an NTC resistor. The thermistor is thermally coupled to the laser diode and part of a Wheatstone bridge. The voltage difference of the bridge is buffered, scaled and offset by a non-inverting amplifier. The output signal is quantized by an ADC whose resolution is the limiting factor for the accuracy of the laser temperature control loop.

The low range current sink of the laser current generator discussed in Section 4.2.2.3 has a full-scale range of 1.953 μA. This is equivalent to a laser temperature interval of 0.0195 K[12] (0.0252 K)[13]. The resolution of the high range current sink is set to half of the low range full-scale in order to avoid missing output currents due to part imperfections (see Section 4.2.2).

Therefore, laser temperature changes greater or equal to half of the low range full-scale require an adaption of the high range current sink in order to keep the output wavelength tuned to the fine structure transition $5^2S_{1/2} \rightarrow 5^2P_{1/2}$ (see Figure 2.1). This process would lead to hysteresis effects at the laser output current and would result in additional noise of the laser carrier frequency. Consequently, the temperature control loop should be designed to keep the laser temperature within half of the low range current sink full-scale and, respectively, within the temperature range of 0.0098 K (0.0126 K) in order to avoid hysteresis noise.

Additionally, the measurement should cover all temperatures which are paired to the laser injection current operating range of 1.5 to 2 mA. The experimentally determined temperature-current pairs for a constant wavelength of $\lambda_{LASER} = 794.979$ nm

[12] The wavelength tuning over current coefficient of 0.6 nm/mA and the wavelength tuning over temperature coefficient of 0.06 nm/K result in a temperature over current coefficient of 10 K/mA. Values are obtained from ULM photonics 795 nm single mode VCSEL diode datasheet, v4.

[13] Parameters shown in braces are measured for the same laser diode. The displacement coefficient of -2.99 μA/GHz and the temperature dependence of -25.96 GHz/K result in a temperature over current coefficient of 12.88 K/mA.

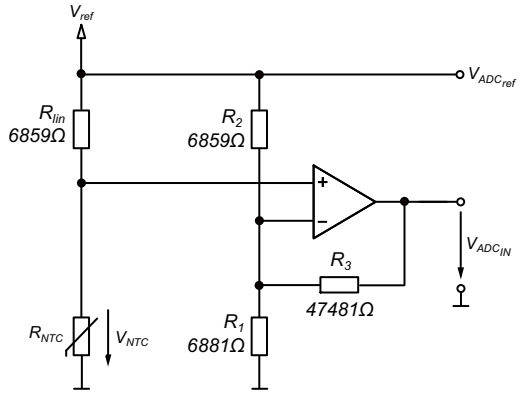

Figure 4.28: Laser temperature measurement circuit with calculated values.

are 38.3°C at 1.5000 mA, 35.2°C at 1.7500 mA and 32°C at 2.0000 mA. With a margin of about 20 %, the lower and the upper limit of the measurement are set to 31.4°C and 38.9°C, respectively.

With a temperature measurement range of 7.5 K and a 12 bit ADC, the minimal quantized temperature step of 0.00183 K is a fraction of 5.3 (6.9) of the target resolution.

Table 4.1 shows the lower limit, the upper limit and the nominal temperature of the laser temperature measurement with the corresponding NTC[14] resistances, the voltages at the NTC resistor and the voltages at the ADC input. The nominal operating current of the laser diode is set to 1.75 mA which enables a balanced adjustment range for the current sinks (see Section 4.2.2). The resistance of R_{lin} in Figure 4.28 has been selected equal to the NTC resistance at the nominal temperature of 35.2°C ($R_{NTC} = 6859\,\Omega$) which leads to the maximum temperature-to-voltage gain factor of the measurement at this point [33]. R_2 is set equal to R_{lin}. The voltages V_{NTC_l} and V_{NTC_u} at the NTC resistor which correspond to the lower and upper limit of the temperature measurement range, respectively, can be calculated by

$$V_{NTC_l} = V_{ref}\frac{R_{NTC_{31.4°C}}}{R_{lin} + R_{NTC_{31.4°C}}} = 2.67\,V \tag{4.38}$$

and

$$V_{NTC_u} = V_{ref}\frac{R_{NTC_{38.9°C}}}{R_{lin} + R_{NTC_{38.9°C}}} = 2.34\,V \tag{4.39}$$

[14]The NTC resistances refer to measured values of EPCOS B57550G103J.

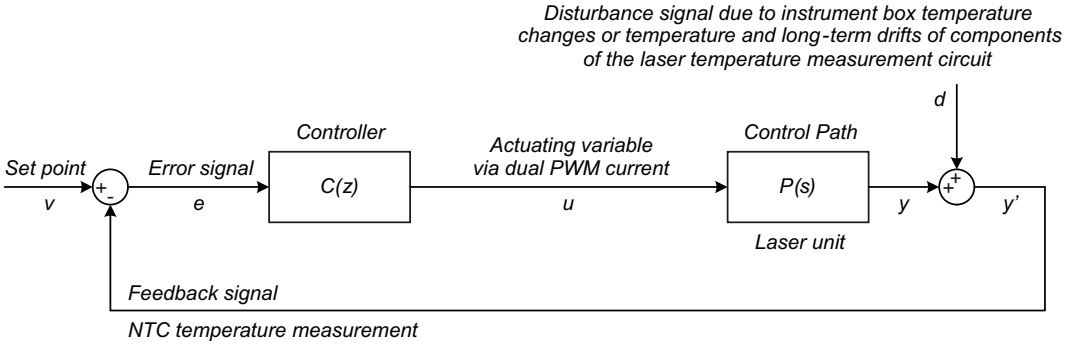

Figure 4.29: Block diagram of the laser temperature control loop.

where V_{ref} is the supply voltage generated by a voltage reference for the Wheatstone bridge and for the ADC. V_{NTC_l} and V_{NTC_u} are mapped to $V_{ADC_l} = V_{ref} = 5\,V$ and $V_{ADC_u} = 0\,V$, respectively, in order to fit the ADC input range. The required amplification factor can be calculated by

$$A = \frac{V_{ADC_u} - V_{ADC_l}}{V_{NTC_u} - V_{NTC_l}} = 14.8\,. \tag{4.40}$$

The amplification of the non-inverting amplifier is given by

$$A = 1 + \frac{R_3}{R_1 \parallel R_2} \tag{4.41}$$

With $V_{NTC_l} = 2.67\,V$ mapped to $V_{ADC_{high}} = 0\,V$ the condition

$$V_{NTC_l} = V_{ref}\frac{R_1 \parallel R_3}{R_1 \parallel R_3 + R_2} = 2.67\,V \tag{4.42}$$

must be fulfilled, which leads to equations

$$R_3 = A \cdot R_2 \cdot \frac{V_{NTC_u}}{V_{ref}} = 47481\,\Omega \tag{4.43}$$

and

$$R_1 = -\frac{R_3}{1 + A(\frac{V_{NTC_u}}{V_{ref}} - 1)} = 6881\,\Omega\,. \tag{4.44}$$

4.2.1.5 Controller

In Figure 4.30, the step response of the laser temperature control path in air (red) is measured with a duty cycle step from 0.6875 to 0.8125. The upper plot shows that

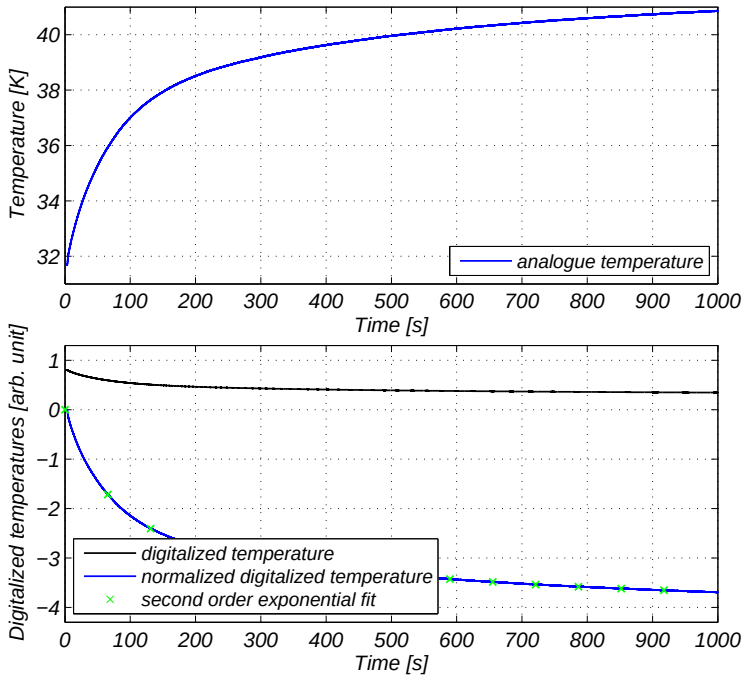

Figure 4.30: Step response of the laser temperature control path P(s) in air.

the laser temperature raises from approx. 31.7°C to 40.9°C within 1000 s. In the lower plot the digitized temperature in the FPGA (black) is normalized to obtain the step response (blue) which is fitted by a second order exponential function (green). The control path P(t) can be expressed as two-pole system in the time domain

$$P(t) = G_1(1 - e^{\frac{t}{\tau_1}}) + G_2(1 - e^{\frac{t}{\tau_2}}) + const \tag{4.45}$$

where $G_1 = -1.62$ and $G_2 = -2.25$ are the gain factors and $\tau_1 = 449\,\mathrm{s}$ and $\tau_2 = 60\,\mathrm{s}$ are the time constants of the first and the second exponential function, respectively. Figure 4.29 shows the block diagram of the simplified laser temperature control loop. The transfer function of the control path in the s-domain, P(s), is given by

$$P(s) = \frac{y(s)}{u(s)} = \frac{G_1}{\tau_1 s + 1} + \frac{G_2}{\tau_2 s + 1} \tag{4.46}$$

which can be rewritten as

$$P(s) = k_P \frac{s + c}{(s + d)(s + e)} \tag{4.47}$$

with

$$\begin{aligned} k_P &= \frac{G_2 \cdot \tau_1 + G_1 \cdot \tau_2}{\tau_1 \cdot \tau_2} \\ c &= \frac{G_1 + G_2}{G_2 \cdot \tau_1 + G_1 \cdot \tau_2} \\ d &= \frac{1}{\tau_1} \\ e &= \frac{1}{\tau_2}\,. \end{aligned} \tag{4.48}$$

For d = 0, the transfer function of the closed control loop T(s) can be expressed as

$$T(s) = \frac{y(s)}{v(s)} = \frac{y'(s)}{v(s)} = \frac{R(s)\,C(s)}{1 + R(s)\,C(s)}\,. \tag{4.49}$$

P(s) can be ideally compensated by the controller

$$C(s) = \frac{u(s)}{e(s)} = k_C \frac{(s+d)(s+e)}{s(s+c)}\,. \tag{4.50}$$

with

$$k_C = \frac{1}{k_P \cdot \tau_T} \tag{4.51}$$

where τ_T is the target time constant of the closed control loop without considering limitation of the system parameters. With the transfer function C(s) in Equation 4.50, the gain, the zero and the poles of the control path are compensated. An additional integrator leads to a steady state error $e_\infty = 0$. The transfer function in the z-domain can be determined for the given parameters c, d, e, k_C with bilinear transformation[15] which can be written as

$$C(z) = \frac{u(z)}{e(z)} = k_C \cdot \frac{b_2 z^2 + b_1 z + b_0}{a_2 z^2 + a_1 z + a_0} \tag{4.52}$$

with[16]

$$b^T = \begin{bmatrix} b_2 & b_1 & b_0 \end{bmatrix}^T = \begin{bmatrix} 1 \\ -1.999876183413669 \\ 0.999876185007842 \end{bmatrix} \tag{4.53}$$

[15] The bilinear transformation can be expressed by $s = \frac{2}{T}\frac{z-1}{z+1}$ where $f_s = 1/T$ refers to the sampling frequency of the controller implementation.

[16] The coefficients are calculated with MathWorks Matlab in the double precision format.

and

$$a^T = \begin{bmatrix} a_2 & a_1 & a_0 \end{bmatrix}^T = \begin{bmatrix} 1 \\ -1.999977098612504 \\ 0.999977098612504 \end{bmatrix} . \tag{4.54}$$

C(z) represents sufficiently the transfer function C(s) for $f_s/f_{-3\,dB} \gg 10$ [50], where f_s refers to the sampling frequency of the digital controller implementation and $f_{-3\,dB}$ to the corner frequency of the control loop. For a "resource-friendly" implementation, the coefficients are approximated by functions of rounded powers of two, which can be implemented as shifting operations in the FPGA. The rounded coefficients b_r and a_r of the controller $C_r(z)$ can be expressed as

$$b_r^T = \begin{bmatrix} b_2 & b_1 & b_0 \end{bmatrix}^T = \begin{bmatrix} 1 \\ -2 + 2^{-13} \\ 1 - 2^{-13} \end{bmatrix} \tag{4.55}$$

and

$$a_r^T = \begin{bmatrix} a_2 & a_1 & a_0 \end{bmatrix}^T = \begin{bmatrix} 1 \\ -2 + 2^{-15} \\ 1 - 2^{-15} \end{bmatrix} . \tag{4.56}$$

Figure 4.31 shows the frequency responses of the control path P(s) (black), of the ideal controller C(z) (dashed green), of the implemented controller $C_r(z)$ (dashed blue), of the ideal closed loop (solid green) and of the implemented closed loop (solid blue). Ideally, the gain factor of the controller is -24.3 in order to enable a hypothetical time constant of $\tau_T = 1\,\mathrm{s}$ of the closed control loop. The bandwidths of the implemented controller and of the closed control loop are slightly higher since the gain factor k_r is realized by a negation and a shift function of 5 which is equal to 32.

4.2.2 Control Loop to Set Laser Current

The laser current control loop is established in order to set the injection current of the VCSEL diode which in combination with the laser temperature directly influences the output frequency. In Section 4.2.2.1, a general overview on the control loop design is given. Section 4.2.2.2 and Section 4.2.2.3 discuss in detail the function blocks which are part of the control unit.

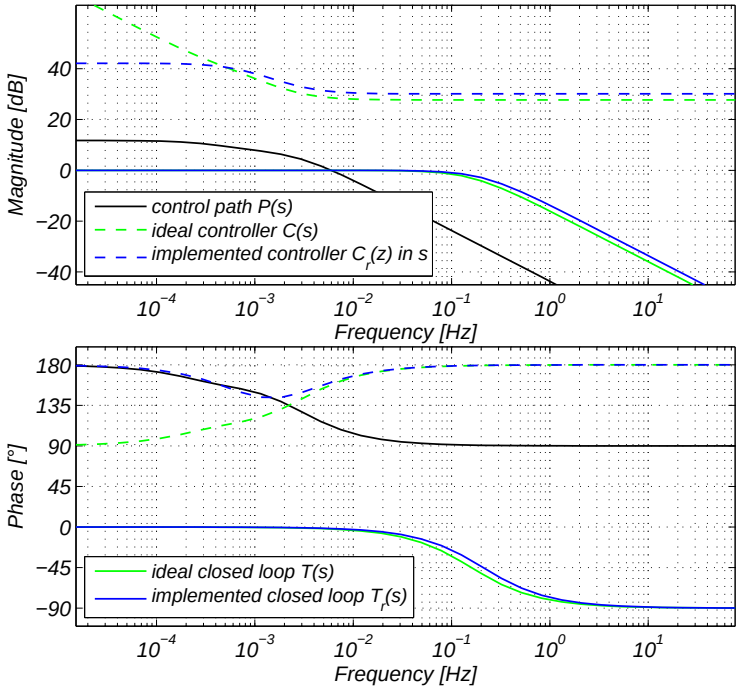

Figure 4.31: Bode diagram of the laser temperature control loop.

4.2.2.1 Overview

The laser current control loop sets the injection current of the VCSEL diode in order to keep the output frequency equal to the frequency of the optical transition $5^2S_{1/2} \rightarrow 5^2P_{1/2}$ for a given laser operating temperature (see Figure 2.1). The used constant current generator is designed to be sufficiently short-term constant on a timescale of $t \leq 10\,\text{min}$. The circuit design is discussed in detail in Section 4.2.2.3. The source supplies the VCSEL diode and, additionally, three adjustable voltage controlled current sinks in parallel via the same current node. Two of the current sinks set the DC current through the laser diode. Here, the control voltages correspond to the actuating variable of the laser current controller in the FPGA. The mapping process of the actuating variable onto the two current sinks is outlined in Section 4.2.2.2. The third current sink is driven by a sinusoidal reference signal which is provided by the lock-in amplifier. It enables FM spectroscopy which is used to stabilize the VCSEL carrier frequency onto the spectral feature (see Figure 4.33). The lock-in amplifier implementation is identical to the Zeeman control loop but operates at a different reference frequency $f_{ref_3} \approx 11160.7\,\text{Hz}$ (see Section 4.1.5). Consequently, the output

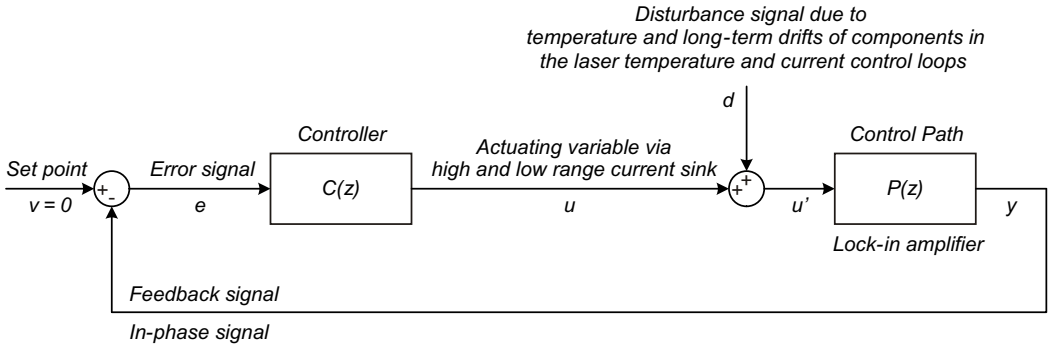

Figure 4.32: Block diagram of the laser current control loop.

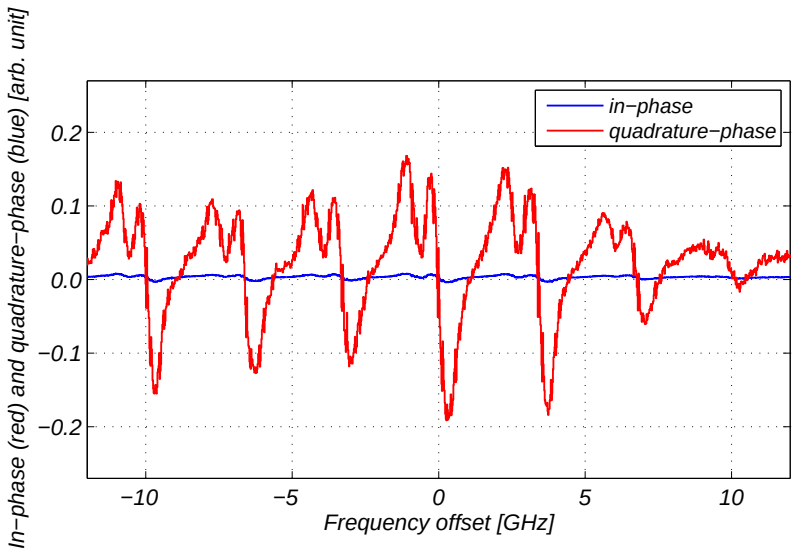

Figure 4.33: Laser frequency spectrum derived by current sweep.

current of the adjustable current generator is actually a superposition of a DC and an AC component. The subsequent signal path is similar to the one of the magnetic field control loop discussed in Section 4.1.

Figure 4.33 shows the in-phase (red) and quadrature-phase (blue) outputs of the lock-in amplifier for a laser current sweep with enabled FM spectroscopy. The fine structure transition frequency ν_{FS} is probed by the laser carrier frequency f_{LASER} and the microwave sidebands $f_{LASER} \pm n\, f_{MW}$ (n = 1, 2, ...).

The parameters for the FM spectroscopy (deviation frequency, modulation index and phase of the reference signal) are different compared to the control loop for the

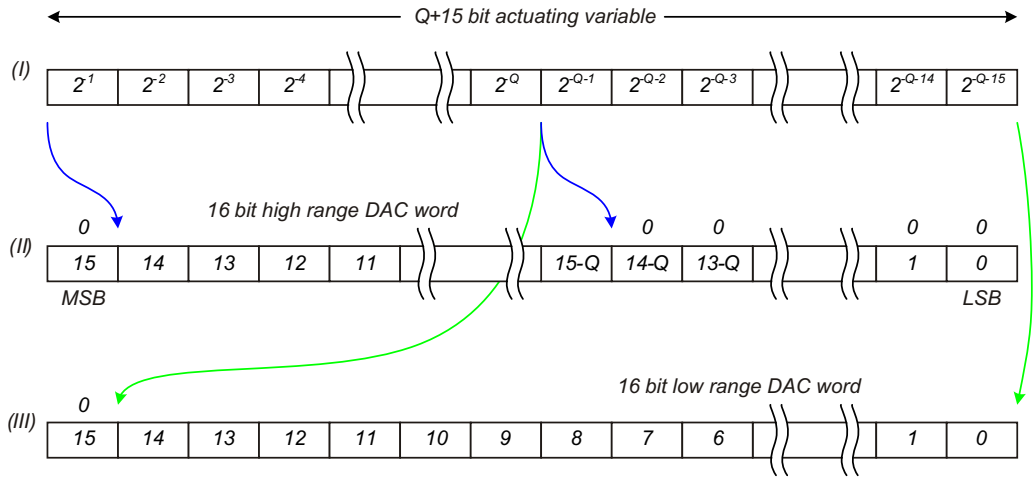

Figure 4.34: Mapping of the actuating variable onto two DAC words.

magnetic field measurement ($f_{ref_3} \ll$ linewidth of spectral feature). Therefore, the demodulation outputs of the lock-in amplifier have to be interpreted differently (see Section 3.1). The in-phase signal (red), or cosine component, is then proportional to the first derivative of the absorption profile while the quadrature-phase signal (blue), or sine component, is related to its second derivative [51]. In consequence, the zero crossing, which is important to track changes of the laser frequency, occurs in the in-phase signal [51] at the zero frequency offset in Figure 4.33.

As shown in Figure 4.32, it is fed to the laser current controller as feedback signal. The controller is identical to the implementation discussed for the Zeeman control loop. Typically, the bandwidth of the laser current controller is set 10 times larger than the bandwidth of the Zeeman control loop in order to reduce noise of the constant current source in the frequency range of the magnetic field measurement.

4.2.2.2 Mapping of Actuating Variable

The combination of a high range and a low range current sink enables a wide adjustment range of the DC injection current with high resolution. In principle, the digital words of the high and low range DACs correspond to the actuating variable of the laser current controller. The least significant current step of the high range current sink is set to half of the full range of the low range current sink. This overlap avoids missing analogue current outputs due to part tolerances.

In Figure 4.34, the actuating variable is scaled to one (I). The digital input word for the high range DAC is defined by the ratio of the high range and the low range.

For instance, with a sink ratio of 2^8 as implemented in Figure 4.35 only the Q = 9 most significant bits of the actuating variable are mapped to the high range DAC while the rest of the high range bits is zero (II). The subsequent bits of the actuating variable are mapped to the low range DAC (III). As discussed in Section 4.2.2.3, the Most Significant Bits (MSB) of both, the high range and low range DAC word, are set to one.

4.2.2.3 Current Generator

The constant current generator circuit in Figure 4.35 consists of three subunits, the constant current source (shown in the upper third), the high range and low range current sinks to adjust the DC injection current, the sink with sinusoidal output to enable frequency modulation spectroscopy (shown in the center) and the protection circuit (shown in the lower third).

The microwave oscillator in the current CDSM design requires a laser injection current which refers to ground potential. This limits significantly possible options for the design and implementation of a precise and long-term stable constant current source. The selected circuit[17] in Figure 4.35 consists of two inverting operational amplifiers with an additional feedback loop from the circuit output to the inverting input of IC 1a. With the condition

$$R_3 = R_2 - R_1 \tag{4.57}$$

the output current I_{DC} does not depend on the output voltage V_{node} and can be expressed by

$$I_{DC} = \frac{R_2}{R_1(R_2 + R_{ref})} \cdot V_{ref} \tag{4.58}$$

where V_{ref} is the output of a voltage reference, e.g. 7 V. In addition to the circuit in [33], two capacitors C_1 and C_2 in the feedback loop of each inverting operational amplifier sub-circuit slow down the current source and reduce significantly the current noise. In a typical operation mode, the circuit sources the VCSEL diode and three adjustable voltage-controlled current sinks in parallel via the same current node.

Each current sink operates similar and consists of a DAC, an operational amplifier, an npn-transistor and a resistor. As an example, for the high range current sink, the DAC output voltage V_h is fed to the non-inverting input of the operational amplifier IC 3a. The voltage adjusts the amplifier's output and the current through the resistor R_h in order to minimize the voltage difference between the amplifier inputs. The

[17] The constant current source is based on a design example in [33] page 797 f.

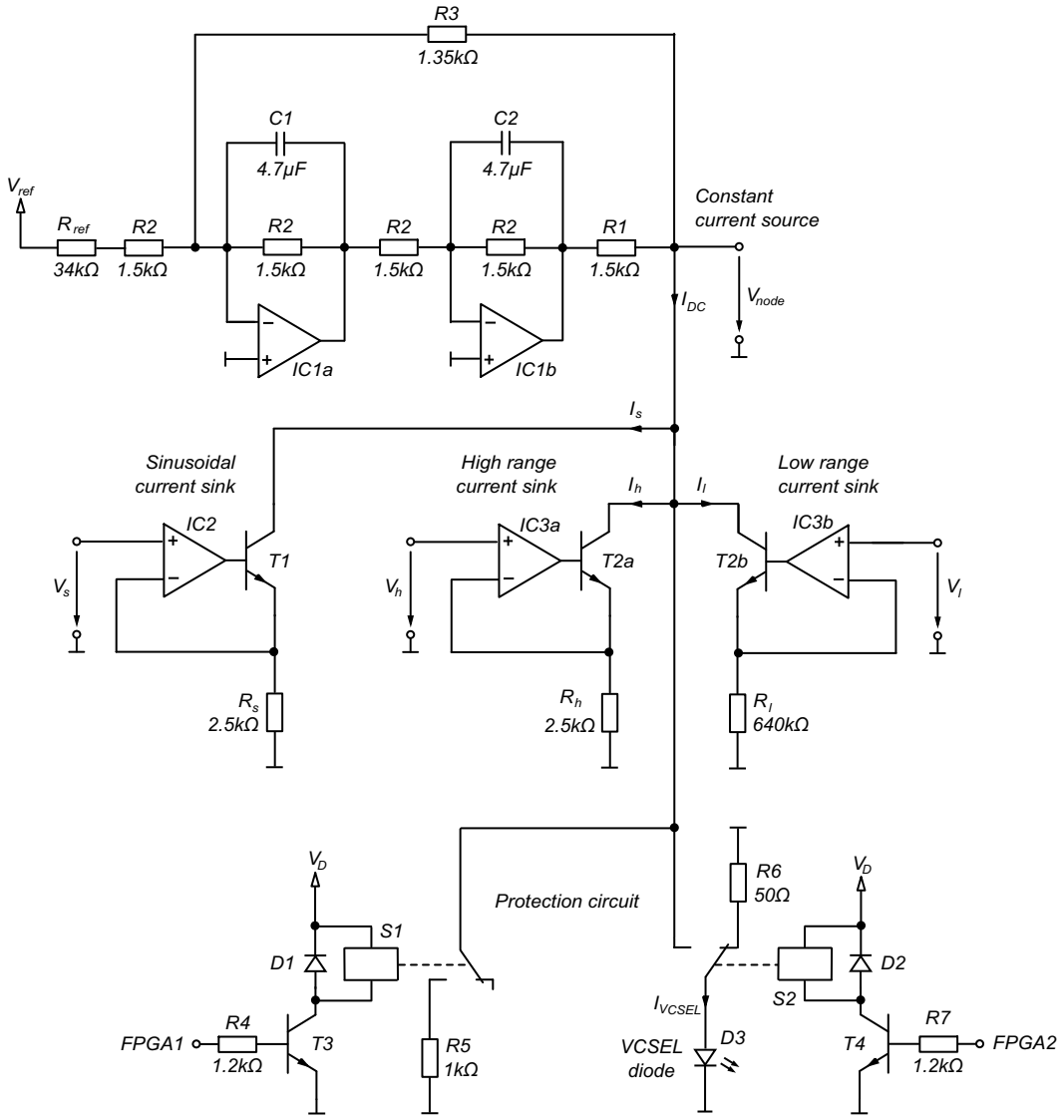

Figure 4.35: Schematics of laser current generator.

current I_h through the resistor R_h is defined by Ohm's law and can be expressed for ideal components as [33]

$$I_h = \frac{V_h}{R_h} \,. \tag{4.59}$$

The nominal threshold voltage V_{th} of the selected VCSEL diode[18] is 1.8 V. A DAC output voltage V_h greater than the sum of threshold voltage V_{th} and the forward voltage V_f of the collector-base diode inherent in the transistor T_{2a} would lead to a malfunction of the current sink. The operational amplifier in combination with the conductive collector-base transition would turn the current sink into a source and the resulting over-current could damage the VCSEL diode. The MSB is permanently set to zero for the selected DAC with a full-scale range of 2.5 V[19]. This limits the maximum possible output voltage to 1.25 V without the need of additional analogue components.

The resistors R_h and R_l are selected to 2.5 kΩ and 640 kΩ, respectively, which leads to an adjustment range of 0.5 mA for the injection current with a theoretically minimum current step of 60 pA for a 16 bit DAC.

The operational amplifiers IC 4a and IC 4b and the npn-transistors T 2a and T 2b are implemented as dual parts on common dies. The electrical characteristics e.g. possible temperature and long-term drifts match to high extend which keeps the ratio between the high range and the low range current sink preserved.

For the low range and the sinusoidal current sink, the parasitic offset voltage of the used operational amplifiers could lead to switching noise in the output current or to harmonic distortion, respectively. Consequently, both digital DAC words are shifted by a constant value whose output voltage is greater than the worst case offset voltage considering operating temperature range and mission life time. This approach does not reduce the output resolution and keeps the maximum output voltage below the critical voltage sum of V_{th} and V_f.

VCSEL diodes are sensitive to EMI and Electro-Static Discharge (ESD). Therefore, an additional circuit is needed to protect the laser diode when it is unbiased and at start-up (see Figure 4.35). In the unpowered mode, the monostable relays S 1 and S 2 keep the output of the current generator open and terminate the VCSEL diode with the resistor R_6 to ground, respectively. At instrument start-up, the FPGA output 1 switches the relay S 1 and connects the resistor R_5 to the output of the current generator. Transient processes of the generator are only seen by the dummy load R_5 and after some time the voltage V_{node} is settled within the operating range of the VCSEL diode. Then, the FPGA output 2 and the relay S 2 switch the VCSEL diode parallel to R_5. In steady state, the dummy load R_5 is released by S 1 and the VCSEL diode is in operation mode. With this sequence, transients at start-up cannot harm

[18] The nominal threshold voltage is obtained from the ULM photonics 795 nm single mode VCSEL diode datasheet, v4.

[19] E.g. Maxim MAX542 serial-input, voltage-output 16 bit DAC.

the laser diode and only one relay needs to be powered permanently (S 2).

4.3 Control Loop to Track Hyperfine Structure Transition

The microwave control loop is established to tune the microwave generator frequency in order to cancel adverse systematic frequency shifts of the hyperfine structure transition $5^2S_{1/2}$, F = 1, $m_F = 0 \leftrightarrow 5^2S_{1/2}$, F = 2, $m_F = 0$ and to compensate long-term drifts of the microwave generator. In Section 4.3.1, a general overview on the control loop design is given. Section 4.3.2 discusses in detail the analogue output structure.

4.3.1 Overview

The hyperfine structure transition frequency ν_{HFS} depends in second order on the magnetic field (57.514 kHz/mT^2), the buffer gas pressure (2.94 Hz/Pa), the buffer gas temperature (4.1 Hz/K for 4 kPa) and the light intensity.

A mismatch $\Delta\nu_{HFS}$ of the microwave generator frequency and the hyperfine structure transition frequency causes a pair of CPT resonances which are split by the magnitude $\Delta\nu_{HFS}$ instead of one single superposition (n = ±1, ±2 or ±3). In case of $\Delta\nu_{HFS} < \delta\nu_{CPT}$, where $\delta\nu_{CPT}$ is the linewidth of the CPT resonance, this splitting is not entirely resolved and thus observable as distorted, dispersive shaped signal. In case of equal CPT resonance line strengths (n = −1 and 1, n = −2 and 2 or n = −3 and 3) the point of zero crossing is identical to the case $\Delta\nu_{HFS} = 0$. Therefore, a mismatch would not affect the magnetic field measurement of the CDSM [8]. Unfortunately, the line strengths of single positive and negative numbered CPT resonances are not symmetric due to the influence of the optical pumping [22]. Hence, the systematic error induced by the mismatch is not entirely cancelled.

The CPT resonance related to the hyperfine structure splitting transition can be used as reference to tune the microwave generator frequency in order to reach $\Delta\nu_{HFS} = 0$ and thus achieve cancellation of the adverse systematic frequency shifts induced by the buffer gas, the AC Stark effect [27] or the mismatch of $\Delta\nu_{HFS}$. Additionally, the hyperfine structure transition control loop is capable to compensate long-term drifts of the microwave generator. The required calibration period depends on the stability of the microwave generator implementation.

The microwave generator is realized by a phase-locked loop which consists of a voltage-controlled microwave oscillator and a fractional n-counter frequency divider. The generator provides a constant radio frequency power level and a modulation bandwidth up to 10 MHz. The time base for the microwave generator is an ad-

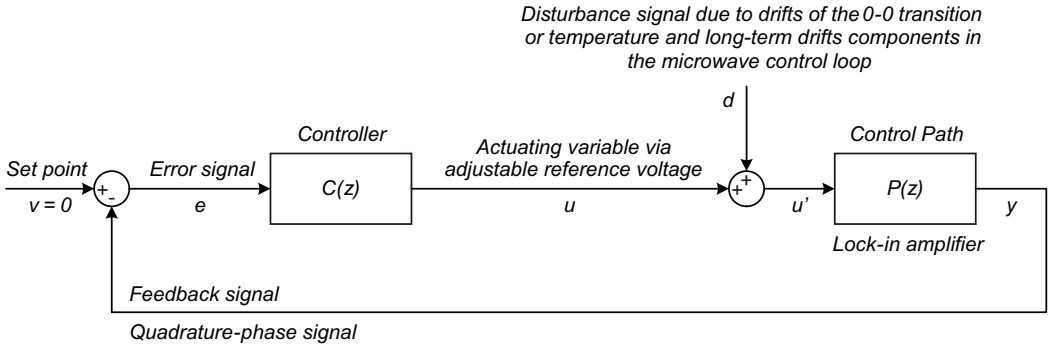

Figure 4.36: Block diagram of the microwave control loop.

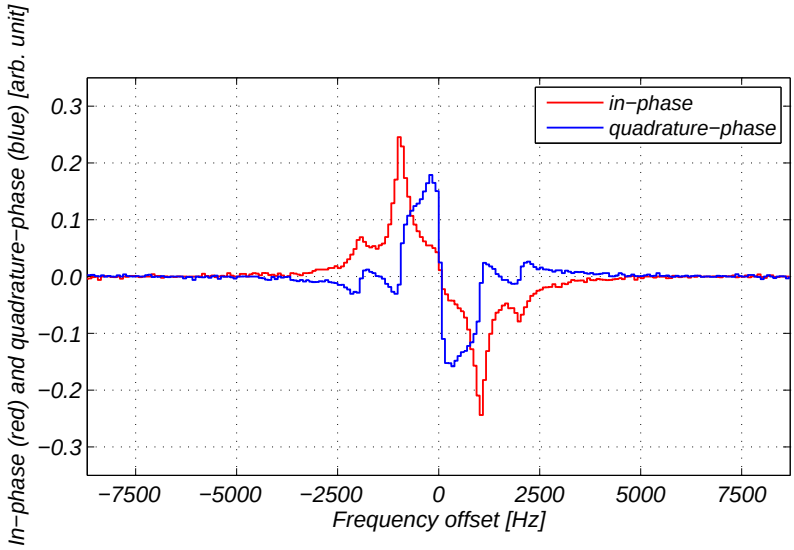

Figure 4.37: Frequency spectrum of the hyperfine structure transition.

justable temperature-compensated crystal reference oscillator which is tuned via a voltage input by the actuating variable of the microwave controller in Figure 4.1 and Figure 4.36. A sinusoidal signal with the frequency $f_{ref_2} \approx 1905.5\,\mathrm{Hz}$ is superposed to the actuating variable and enables an FM spectroscopy technique for stabilizing the microwave oscillator. The analogue output structure which superposes and buffers both signals is discussed in Section 4.3.2. The subsequent signal path and the interpretation of the demodulation outputs of the lock-in amplifier are similar to the magnetic field detection control loop in Section 4.1.

Figure 4.37 shows the in-phase and quadrature-phase signal of the lock-in amplifier

for a reference oscillator output frequency sweep with enabled FM spectroscopy. The hyperfine structure transition[20] $\mathrm{F}=1,\ \mathrm{m}_F=0 \rightarrow \mathrm{F}=2,\ \mathrm{m}_F=0$ with the frequency ν_{HFS} is probed by the microwave frequency f_{mw} and the frequency modulation spectroscopy sidebands at multiples of f_{ref_2}. The zero crossing appears in the quadrature-phase output (blue) which is fed to the control unit as feedback signal (see Figure 4.36).

The controller is identical to the implementation for the Zeeman control loop. Typically, the bandwidth of the microwave controller is set to $\tau_T < 1\,\mathrm{s}$ in order to reduce a possible interference with the magnetic field measurement.

Ideally, the hyperfine structure transition is permanently tracked in order to compensate the adverse systematic shifts mentioned above. However, the transition corresponds to $\mathrm{n}=0$ in Equation 2.3 and the amplitude of its spectral feature experiences the same dependence on the angle θ between the magnetic field direction and the optical axis of the sensor cell as the CPT resonances with $\mathrm{n}=\pm 2$ (see Equation 2.3. As consequence, the control loop cannot work reliable at wide angles (e.g. $70^\circ < \theta < 110^\circ$). For this alignment range a pre-recorded look-up table can adjust the reference oscillator according to the measured sensor temperature and magnetic field data. Another option is to apply periodically (e.g. for three seconds in every minute) an artificial magnetic field in direction of the optical axis in order to increase the strength of the CPT resonance $\mathrm{n}=0$ and to calibrate the microwave generator to the hyperfine structure transition.

The reference oscillator also serves as a time base for the signal processing in the FPGA and, therefore, influences the magnetic field measurement which is derived by the Breit-Rabi formula in Equation 2.1. Since the reference output frequency is adjusted in order to compensate the buffer gas pressure, the buffer gas temperature, the AC Stark light shift and the magnetic field dependences of the hyperfine structure transition, a systematic error is introduced to the magnetic field measurement. For instance, a reference oscillator with $\mathrm{f}_0 = 20\,\mathrm{MHz}$, the influence of a magnetic field of $50\,\mu\mathrm{T}$, a gas pressure of 4 kPa and a temperature change of 25 K cause accuracy errors of the magnetic field measurement of 1 pT, 86 pT and 1 pT, respectively [29] [27]. These errors can be removed entirely by pre-determination of the gas pressure and post-processing of the magnetic field and housekeeping data.

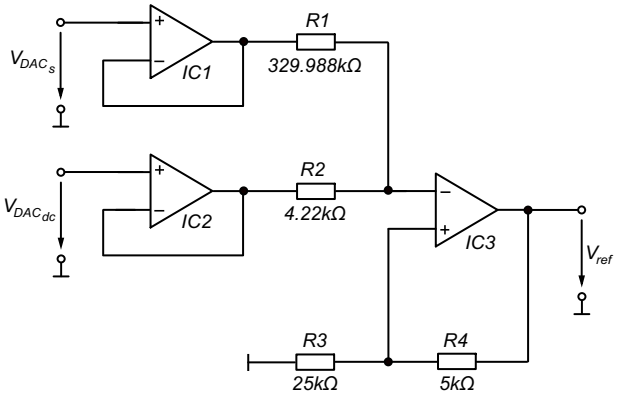

Figure 4.38: Schematics of the V_{ref} output circuit with calculated values.

4.3.2 Analogue Output Circuit

The circuit shown in Figure 4.38 consists of two adjustable voltage sources realized by two DACs[21], three operational amplifiers and 4 resistors. The output of the DAC voltage source $V_{DAC_{DC}}$ corresponds to the actuating variable of the microwave controller while the sinusoidal DAC output V_{DAC_s} enables frequency modulation spectroscopy. Both voltages are buffered, combined and scaled by two voltage followers and a non-inverting summer[22] in order to obtain the required adjustment voltage V_{ref} for the reference oscillator. The voltage can be expressed by

$$V_{ref} = \frac{R_2}{R_3} \cdot \frac{R_3 + R_4}{R_1 + R_2} \cdot V_{DAC_s} + \frac{R_1}{R_3} \cdot \frac{R_3 + R_4}{R_1 + R_2} \cdot V_{DAC_{DC}} \,. \tag{4.60}$$

The upper input limit of the selected reference oscillator[23] is

$$V_{ref_u} = 3\,V \,. \tag{4.61}$$

The signal V_{DAC_s} is digitally limited to and shifted by half of the DAC full-scale output voltage $V_{DAC}/2$ in order to avoid harmonics due to possible offset voltages of the operational amplifiers IC 1 and IC 3. For the modulation frequency $f_{ref_2} =$

[20] The hyperfine structure transition is also called 0-0 transition and is used for alkali-based optically pumped atomic clocks.
[21] E.g. Maxim MAX542 serial-input, voltage-output 16 bit DAC.
[22] The circuit is based on the design example in [52] page A-25.
[23] The adjustment voltage V_{ref} is limited to 0.3 and 3 V for a power supply of 3.3 V. Values are obtained from datasheet for the MtronPTI M611x series precision temperature-compensated voltage-controlled crystal oscillator (TCVCXO).

1905.5 Hz and the selected reference oscillator[24], the sinusoidal peak-peak component $V_{s_{pp}}$ of the reference voltage should be 0.0379 V in order to achieve a modulation index M = 0.5. This can be written as

$$V_{s_{pp}} = \frac{R_2}{R_3} \cdot \frac{R_3 + R_4}{R_1 + R_2} \cdot \frac{V_{DAC}}{2} = 0.0379\,V \tag{4.62}$$

where V_{DAC} = 2.5 V refers to the full-scale output voltage of the DAC. With Equations 4.60, 4.61 and 4.62, the DC component of the reference voltage can be expressed as

$$V_{DC} = \frac{R_1}{R_3} \cdot \frac{R_3 + R_4}{R_1 + R_2} \cdot V_{DAC} = 2.9621\,V\,. \tag{4.63}$$

Furthermore, the condition

$$\frac{R_1 \cdot R_2}{R_1 + R_2} = \frac{R_3 \cdot R_4}{R_3 + R_4} \tag{4.64}$$

should be fulfilled in order to cancel the input bias current of the operational amplifier IC 3 using the common-mode input voltage rejection technique [52]. With a selected resistor R_4 = 5 kΩ and Equations 4.62, 4.63 and 4.64, the resistors R_1, R_2 and R_3 can be defined as

$$R_1 = \frac{V_{DC}}{V_s} \cdot R_2 = 329.988\,k\Omega \tag{4.65}$$

$$R_2 = \frac{5}{6} \cdot (1 + \frac{V_s}{V_{DC}}) \cdot R_4 = 4.220\,k\Omega \tag{4.66}$$

$$R_3 = \frac{V_{DAC}}{V_{ref_u} - V_{DAC}} \cdot R_4 = 25\,k\Omega\,. \tag{4.67}$$

The resolution of the DAC which corresponds to the actuating variable sets the minimal frequency step possible to adjust microwave frequency to the hyperfine structure transition frequency ν_{HFS}. For ideal components, digital zero and full-scale words are mapped to V_{ref} = 0 V and V_{ref} = 2.9621 V, respectively. For the input limits of the selected reference oscillator, this results in a minimum step of the microwave frequency of 1.0676 Hz.

[24] The minimum frequency adjustment range of ±9.2 ppm leads to a range of 62879 Hz for the hyperfine structure transition frequency ν_{HFS}. Values are obtained from datasheet for the MtronPTI M611x series precision TCVCXO.

4.4 Control Loop to Set Rubidium Temperature

The sensor temperature control loop is established in order to set the temperature of the rubidium atoms in the sensor which significantly influences the strengths of CPT resonances. In Section 4.4.1, a general overview on the control loop design is given. Section 4.4.2 to Section 4.4.4 discuss in detail the function blocks which are part of the control unit.

4.4.1 Overview

The strengths of the CPT resonances depend, amongst other parameters, on the vapour pressure of the rubidium atoms in the glass cell and, consequently, on the temperature [27]. By increasing the temperature, more rubidium atoms are in the gaseous phase and available for the interaction with the light field. The strengths of CPT resonances increase while the FWHM narrows with the sensor temperature [15] [17] [23] [29]. Therefore, the noise density of the magnetic field detection decreases but starts to increase again at a certain temperature when the optical thickness effect gets dominant and reduces the CPT resonance line strength again [17]. For a reliable operation of the CDSM the sensor cell temperature must be between 15°C and 60°C. Hence, no temperature control is required for the operation at room temperature (25°C). In case of too low environmental temperatures, which for instance occur during space missions, a sensor temperature control loop is needed.

Similar to the laser temperature control loop, the temperature of the rubidium atoms is set by a bi-directional PWM AC current through a bifilar heating coil around the glass cell. The fundamental period of the PWM is synchronized to the modulation frequency f_{ref_1} of the FM spectroscopy which is used for the magnetic field detection in order to minimize the interference of the AC heating current on the magnetic field measurement. Section 4.4.2 outlines the synthesis process of the PWM heating signals A and B. The output structures for the heating current are identical to option 2 in Section 4.2.1.3.

The glass cell temperature is monitored by a non-magnetic Positive Temperature Coefficient (PTC) resistor[25] and quantized by an ADC. The measurement circuit is discussed in Section 4.4.3. The quantized thermistor signal is fed to the controller which calculates the required duty cycle to keep the actual temperature at the set temperature. The design and implementation of the controller is given in Section 4.4.4.

[25] E.g. Heraeus Sensor Technology PT1000 C 420 B 25AgPd 15.

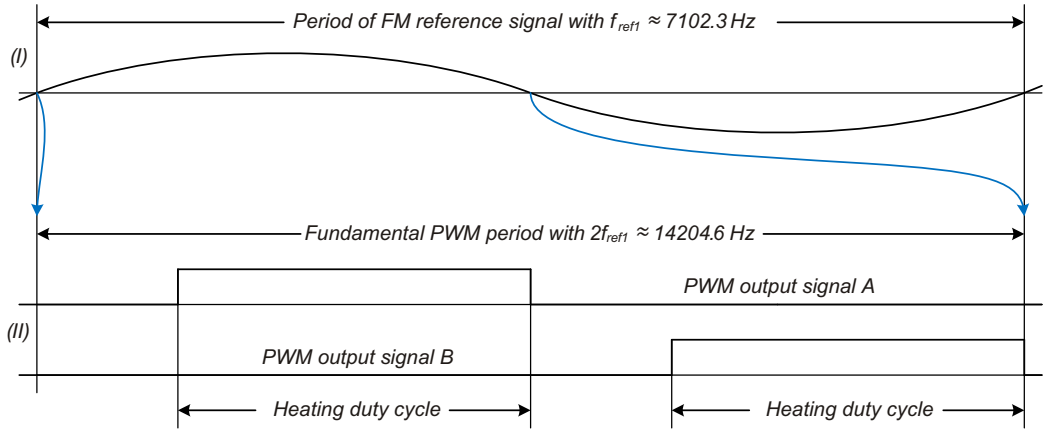

Figure 4.39: Sensor temperature heating waveforms.

4.4.2 Synthesis of Duty Cycle

A common technique in order to reduce the influence of the heating current on the magnetic field measurement to a large extent is the bifilar heating coil. Another technique is the proper selection of the waveform of the heating current (see Figure 4.39). As discussed in Section 4.1.5, the lock-in amplifier used for the magnetic field detection operates at the modulation frequency f_{ref_1} of approx. 7102.3 Hz (I). The moving average filter and the entire magnetic field measurement has spectral minima at frequency multiples of $2f_{ref_1}$ (see Figure 4.17). A PWM of the heating current with the fundamental frequency $2f_{ref_1}$ (II) would have frequency components identical to those spectral minima. Consequently, for an ideal implementation, the heating current should not have an influence on the magnetic field measurement.

If the output structures are realized by discrete components, both p-channel and both n-channel MOSFETs should be part of the same lot and thermally coupled. With this design, the resistances for both signal paths match to a high extent and the influence on the magnetic field measurement due to a parasitic DC field is minimized.

4.4.3 Temperature Measurement

The implementation for the sensor temperature measurement and quantization is similar to the circuit discussed for the laser temperature control loop in Section 4.2.1.4. The temperature of the sensor cell is measured with a PTC resistor which is magnetically clean and sufficient linear over the required temperature measurement range of -70°C to 80°C (see Table 1.2). The thermistor is thermally coupled to the rubidium-

Table 4.2: Parameters of the sensor temperature measurement.

	Temperature (°C)	R_{PTC} (Ω)	V_{PTC} (V)	V_{PTC} (V)
Lower limit	-70	723	0.337	0
Nominal	20	1078	0.487	3.28
Upper limit	80	1309	0.579	5

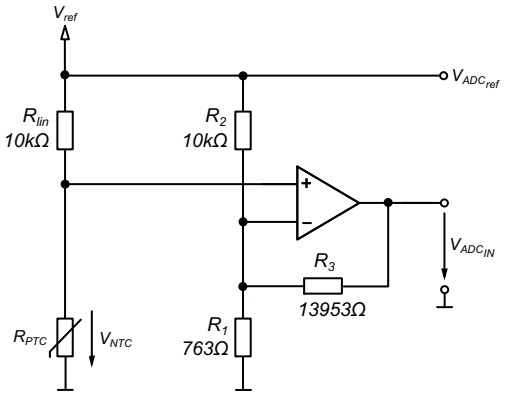

Figure 4.40: Sensor temperature measurement circuit.

filled glass cell and is part of a Wheatstone bridge whose voltage difference is buffered, scaled and offset by the non-inverting operational amplifier circuit in Figure 4.40.

With a temperature measurement range of 150 K and a 12 bit ADC, the digital temperature resolution is 0.0366 K. This resolution is sufficient in order to fulfil the temperature stabilization requirement of 1 K accuracy.

Table 4.2 shows the lower limit, the upper limit and the nominal set temperature of the sensor temperature measurement with the corresponding PTC resistances, the voltages at the PTC resistor and the voltages at the ADC input. The nominal operating temperature of the sensor cell is set to 20°C. The resistances of R_{lin} and R_2 in Figure 4.40 have been selected to 10 kΩ in order to limit the self-heating of the thermistor. The voltages V_{PTC_l} and V_{PTC_h} at the PTC resistor correspond to the lower and upper limit of the temperature measurement range, respectively, and can be calculated by

$$V_{PTC_l} = V_{ref} \frac{R_{PTC_{-70°C}}}{R_{lin} + R_{PTC_{-70°C}}} = 0.337\,V \tag{4.68}$$

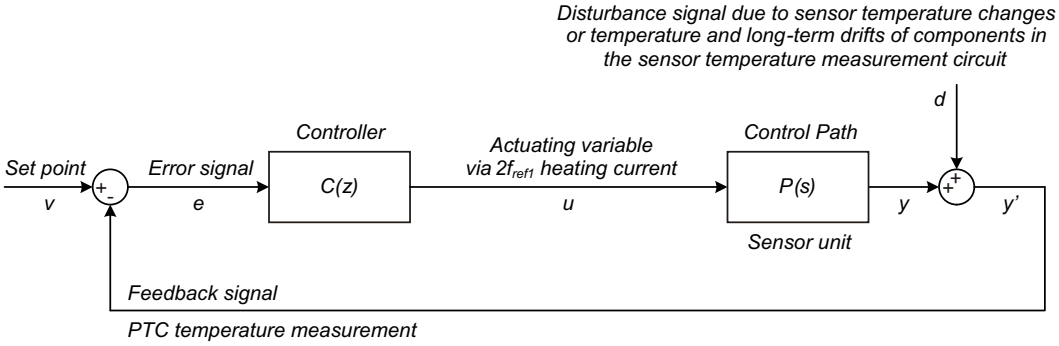

Figure 4.41: Block diagram of the sensor temperature control loop.

and

$$V_{PTC_h} = V_{ref} \frac{R_{PTC_{80°C}}}{R_{lin} + R_{PTC_{80°C}}} = 0.579\,V \tag{4.69}$$

where V_{ref} refers to the reference voltage of the Wheatstone bridge and the ADC. V_{PTC_l} and V_{PTC_h} are mapped to $V_{ADC_l} = 0\,V$ and $V_{ADC_h} = V_{ref} = 5\,V$, respectively, in order to fit the ADC input range. The required amplification factor can be calculated by

$$A = \frac{V_{ADC_h} - V_{ADC_l}}{V_{PTC_h} - V_{PTC_l}} = 20.7\,. \tag{4.70}$$

The amplification of the non-inverting amplifier circuit is given by Equation 4.41. With the condition

$$V_{PTC_l} = V_{ref} \frac{R_1 \parallel R_3}{R_1 \parallel R_3 + R_2} = 0.337\,V \tag{4.71}$$

R_3 and R_1 can be calculated to

$$R_3 = A \cdot R_2 \cdot \frac{V_{PTC_h}}{V_{ref}} = 13953\,\Omega \tag{4.72}$$

and

$$R_1 = -\frac{R_3}{1 + A(\frac{V_{PTC_h}}{V_{ref}} - 1)} = 763\,\Omega\,. \tag{4.73}$$

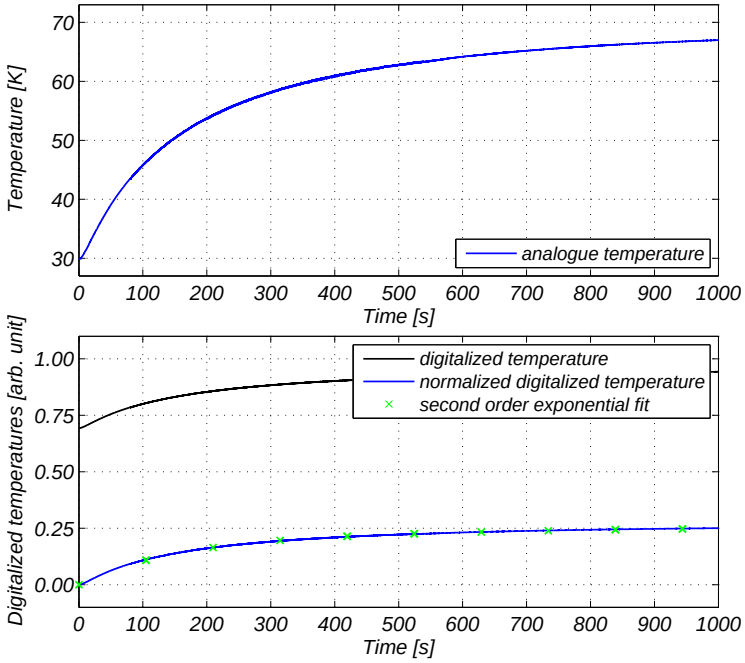

Figure 4.42: Step response of the sensor temperature control path.

4.4.4 Controller

Figure 4.41 shows the block diagram of the simplified sensor temperature control loop. The design and implementation of the sensor temperature controller is similar to the process outlined for the laser temperature controller in Section 4.2.1.5. In Figure 4.42, the step response of the sensor temperature control path in air is measured with a manual duty cycle step from 0 to 1. In the upper plot, the sensor temperature raises from approx. 29.8°C to 67.0°C within 1000 s. In the lower plot, the measured temperature in the FPGA is normalized to obtain the step response (blue) which is fitted by a second order exponential function. The response of the two-pole system can be expressed in the time domain by Equation 4.45 with the gain factors $G_1 = 0.081$ and $G_2 = 0.187$ and the time constants $\tau_1 = 672\,\text{s}$ and $\tau_2 = 143\,\text{s}$, respectively. The transfer function in the s-domain, P(s), is given by Equation 4.48 and can be ideally compensated by a controller C(s) with the structure as outlined in Equation 4.50. The transfer function of the controller R(s) compensates the gain, the zero and the poles of the control path. Additionally, an integrator leads to a steady state error $e_\infty = 0$. The transfer function in the z-domain, R(z), can be determined with bilinear transformation. Identical to Equation 4.52, it can be expressed by

$$C(z) = k_R \cdot \frac{b_2 z^2 + b_1 z + b_0}{a_2 z^2 + a_1 z + a_0} \tag{4.74}$$

with[26]

$$b^T = \begin{bmatrix} b_2 & b_1 & b_0 \end{bmatrix}^T = \begin{bmatrix} 1 \\ -1.999944419346114 \\ 0.999944419793047 \end{bmatrix} \tag{4.75}$$

and

$$a^T = \begin{bmatrix} a_2 & a_1 & a_0 \end{bmatrix}^T = \begin{bmatrix} 1 \\ -1.999987202973020 \\ 0.999987202973020 \end{bmatrix} . \tag{4.76}$$

For a "resource-friendly" implementation, the coefficients are approximated by functions of rounded powers of two, which can be implemented as shifting operations in the FPGA. The rounded coefficients b_r and a_r can be expressed as

$$b_r^T = \begin{bmatrix} b_2 & b_1 & b_0 \end{bmatrix}^T = \begin{bmatrix} 1 \\ -2 + 2^{-14} \\ 1 - 2^{-14} \end{bmatrix} \tag{4.77}$$

and

$$a_r^T = \begin{bmatrix} a_2 & a_1 & a_0 \end{bmatrix}^T = \begin{bmatrix} 1 \\ -2 + 2^{-16} \\ 1 - 2^{-16} \end{bmatrix} . \tag{4.78}$$

Figure 4.43 shows the frequency responses of the control path P(s) (black), the ideal controller C(s) (dashed green) and implemented controller C_r(z) (dashed blue) as well as of the ideal closed loop T(s) (solid green) and implemented closed loop T_r(s) (solid blue). Ideally, the gain factor of the controller is 700.2 in order to enable a hypothetical time constant of $\tau_T = 1\,\mathrm{s}$ of the closed control loop. The bandwidths of the implemented controller and closed control loop are slightly lower since the gain factor k_r is realized by a shift function of 9 which is equal to 512.

[26] The coefficients are calculated with MathWorks Matlab in the double precision format.

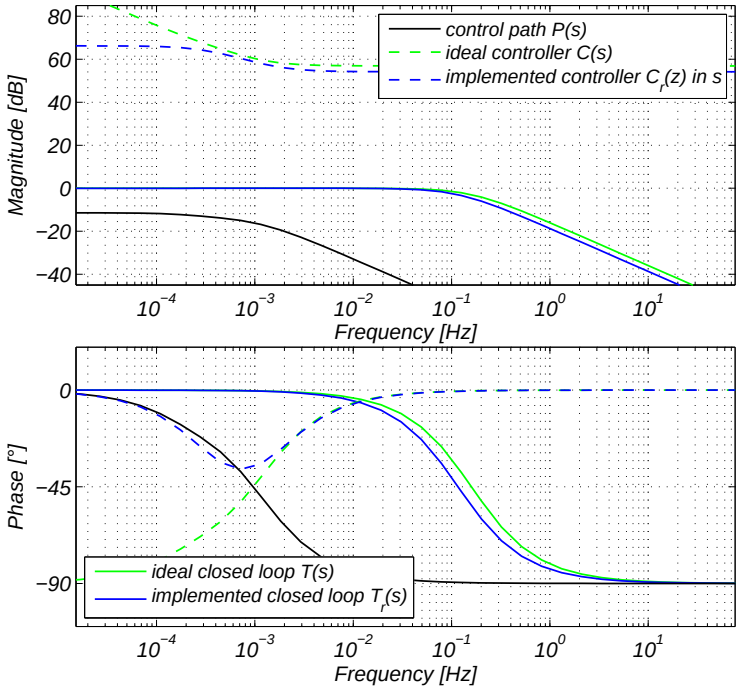

Figure 4.43: Bode diagram of the sensor temperature control loop.

5 Instrument Performance

The resource requirements of the existing prototype and for a power supply optimized implementation are outlined in Section 5.1. The key performance parameters of the CDSM prototype such as the accuracy, the characteristics of the power spectral density of detection noise, the temperature dependence and the dynamic range are discussed in Section 5.2.

5.1 Required Resources

The prototype of the CDSM shown in Figure 4.2 has been developed as EM for the Chinese low Earth orbit mission EMS, which will be launched in 2016. Table 5.1 shows the required mass and power consumption of the EM design for two different power supply configurations.

In columns denoted by *Prototype*, the values for mass and power in air and vacuum are measured using the existing prototype and are based on the power interface of $\pm$ 12 V and 5 V defined for the EMS mission. The interface is determined by the Chinese power supply system and available DC/DC converters. Nominal overall power consumption in air and vacuum are 5267 mW and 3498 mW, respectively. Significant power loss occurs in the line regulators. The instrument mass of 774 g includes a five meter long harness which connects the mixed signal electronics board and the sensor unit.

For columns denoted by *Optimized instrument*, the measured current consumptions of single components and functional blocks are re-calculated for a power supply interface of $\pm$5 V, 3.3 V and 1.2 V and take corresponding datasheets into account. The calculations show that an optimized instrument interface can significantly reduce the nominal overall power consumption to 2515 mW in air and 1427 mW in vacuum.

Table 5.1: Resources measured for EMS and estimated for optimized interface.

	EMS/Prototype [a]			Optimized instrument [b]	
	Mass (g)	Power air (mW)	Power vacuum (mW)	Power air (mW)	Power vacuum (mW)
Mixed signal electronics board	320				
Control unit		2061	2061	956	956
Microwave unit		836	836	309	309
Laser unit	90				
Laser temperature control [c]		1575 [d]	403 [d]	455 [e]	123 [e]
Sensor unit	278				
Sensor temperature control [f] (optional)		795 [g]	198 [g]	795 [g]	39 [h]
Harness [i]	86				
Overall	774	5267	3498	2515	1427

[a] Measured and based on power interface defined for the EMS mission: ±12V, 5V.
[b] EMS design re-calculated for optimized power supply: ±5V, 3.3V, 1.2V.
[c] Nominal EMS instrument box temperature and laser operating temperature are 0°C and 35°C, respectively.
[d] Power-to-temperature coefficients of the current laser unit measured for air (45 mW/K) and vacuum (11.5 mW/K) are linearized and averaged.
[e] Power-to-temperature coefficients for a miniaturized laser unit in air (13 mW/K) and vacuum (3.5 mW/K) are derived from thermal simulations.
[f] Nominal EMS boom interface temperature and sensor operating temperature are 0°C and 30°C, respectively.
[g] Power-to-temperature coefficients of the current sensor design measured for air (26.5 mW/K) and vacuum (6.6 mW/K) are linearized.
[h] Power-to-temperature coefficient for a miniaturized and Multi-Layer Insulation (MLI) covered sensor unit in vacuum (1.3 mW/K) is derived from thermal simulations.
[i] Calculated for five meter long harness consisting of two fibres (1.6 g/m) as well as two twisted pair cables (7 g/m) for optional sensor temperature control.

5.2 Measurement Characteristics

The instrument accuracy was experimentally compared to a geomagnetic standard[1] based on the Overhauser effect at the Conrad Observatory of the Central Institute for Meteorology and Geodynamics, Austria. In Figure 5.1, the magnetic flux densities

[1] The GEM GSM-90 is a high sensitivity Overhauser effect magnetometer and a secondary standard for measurement of the Earth's magnetic field.

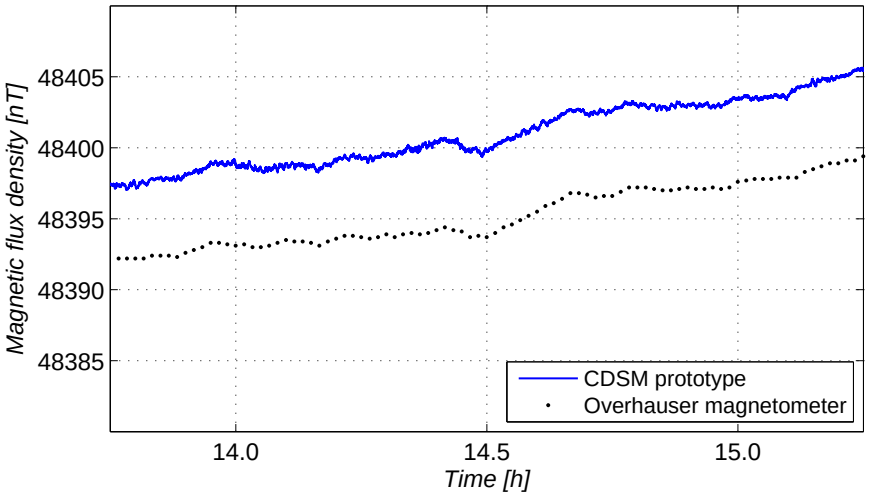

Figure 5.1: Accuracy of magnetic field measurement.

shown were derived by tracking the resonance superposition $n = \pm 2$ (blue) and by a simultaneous measurement with the observatory standard (black). For scientific space missions such as EMS, an absolute error of the magnetic field measurement of less than 0.2 nT is required. The CDSM is expected to meet this goal. However, the measurement shows a constant difference of approximately 5 nT compared to the reference magnetometer. This can be explained by the spatial separation of the two magnetometers of about 150 m and the residual stray field of an already identified sensor component.

Figure 5.2 discusses the frequency characteristics of the CDSM prototype. The blue coloured power spectral density was derived from measurement of the Earth's field based on the resonance superposition $n = \pm 2$ shown in Figure 5.1. The selected corner frequency of approximately 1 Hz and the measured power spectral density of approximately $70\text{pT}/\sqrt{Hz}$ of the CDSM prototype can be clearly separated from the influence of the Earth's magnetic field.

All subsequent measurements were carried out with the sensor unit located in a three-layer μ-metal cylindrical shielding can[2] which in combination with a single coil system[3] for artificial fields leads to a minimum inhomogeneity of 80 nT/m in a cube with side length of 0.05 meters.

In principle, the CDSM should not have a 1/f noise characteristic for frequencies

[2]The μ-metal cylindric shielding can has a height of 1 m and a diameter of 0.5 m.
[3]The system has a coil factor of approx. 1.25 nT/mA.

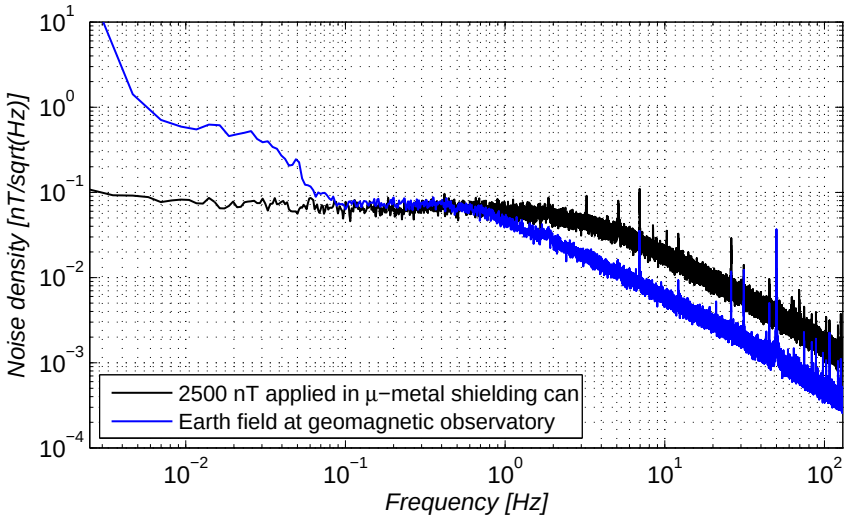

Figure 5.2: Power spectral density of the magnetic field detection noise.

below the selected corner frequency of the instrument. Figure 5.2 also shows the power spectral density of a noise measurement carried out in the shielding can at a constant applied field of approximately 2500 nT and a chosen corner frequency of approximately 3 Hz (black). The power spectral density of approximately 60 $\mathrm{pT}/\sqrt{Hz}$ increases below 10^{-1} Hz which cannot be separated from the temperature drift of the permeability of the μ-metal shielding can or the noise of the constant current source which was needed to drive the artificial field.

At the current stage of development, the power spectral density of the CDSM prototype varies between 40 and 80 $\mathrm{pT}/\sqrt{Hz}$ which needs to be further investigated. However, this is sufficient for scientific space missions where the main purpose of the scalar magnetometer is to improve the long-term stability of the vector magnetometers.

In Figure 5.3, the influence of the sensor temperature on the detected magnetic flux density was measured for two different instrument configurations. The microwave control loop can compensate drifts of the microwave generator and systematic errors of the transition frequency caused by the magnetic field, the gas pressure, the gas temperature and the AC Stark light shift. The temperature dependence of 368 pT/K in a non-tracking microwave generator configuration (black) can be reduced to less than 7 pT/K for a measurement with an active hyperfine structure control loop (blue). The remaining drift cannot be distinguished from drifts of the shielding can or the constant current source which was used to drive the artificial field.

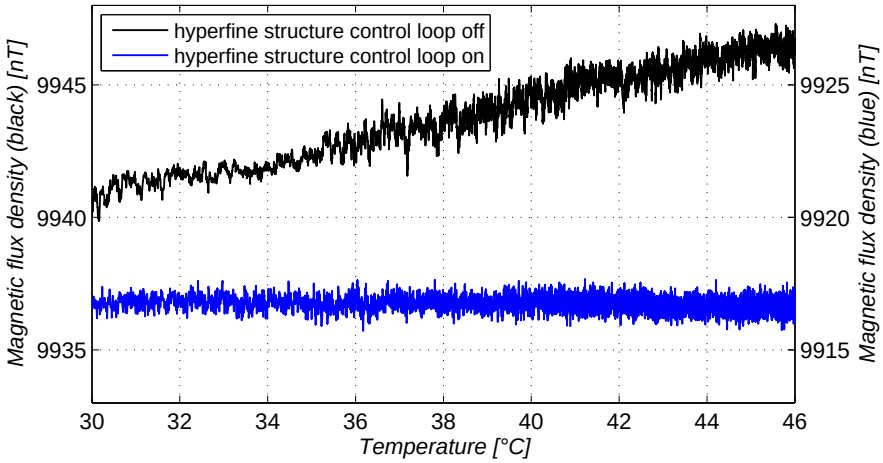

Figure 5.3: Sensor temperature dependence of the magnetic field measurement.

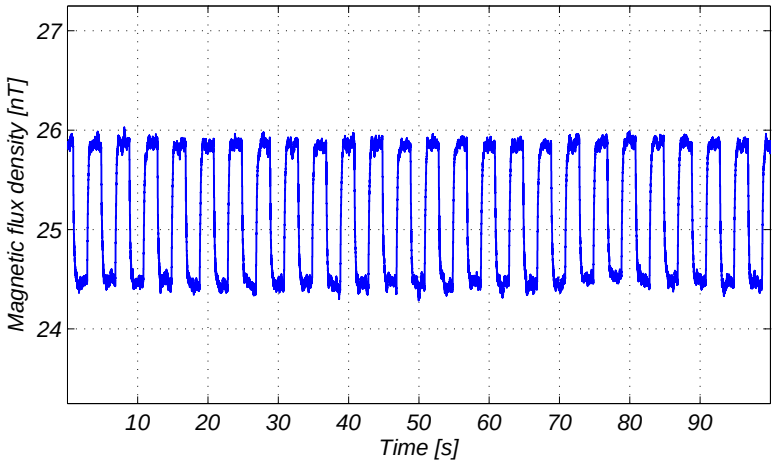

Figure 5.4: Demonstration of the low field performance.

The dynamic range of the CDSM with no change of the hardware configuration is demonstrated in Figure 5.2 and Figure 5.4. In principle, the CDSM is expected to detect magnetic flux densities from the measured value of 25 nT up to an extrapolated value of 1 mT [15] with identical performance [14] [15]. Figure 5.4 shows a rectangular AC field of 1.5 nT_{pp} which can be detected on a 25 nT DC field. The upper limit could not be verified experimentally due to limitations in the test equipment. However, the noise measurements in Figure 5.2 show that similar performances can be achieved for magnetic flux densities of approximately 2500 nT and 48400 nT.

6 Conclusion and Outlook

In total five control loops were identified as necessary for a reliable implementation of the CDSM principle and subsequently designed. All identified control loops were implemented in a single Printed Circuit Board (PCB) in order to enable measurements outside of the laboratory environment, e.g. absolute measurements at a geomagnetic observatory. Furthermore, the control unit is entirely implementable with space grade components and compliant with the resource and interface requirements of the Electro-Magnetic Satellite (EMS) mission. The Chinese low Earth orbit EMS mission is the first flight opportunity for the CDSM aboard a spacecraft. This development is equivalent to raising the Technology Readiness Level (TRL) of the CDSM instrument for the EMS mission from 1 (basic principles observed and reported) to 5 (component and/or breadboard validation in relevant environment).

The accuracy of the CDSM prototype was experimentally compared to a geomagnetic observatory standard (see Figure 5.1). In a first measurement, a constant difference of 5 nT was observed. This can be explained by the spatial separation of the two magnetometers and the residual stray field of an already identified sensor component. The measured power spectral densities of 40 to 80 $\mathrm{pT}/\sqrt{Hz}$ shown in Figure 5.2 do not depend on the instrument bandwidth. The noise performance is sufficient for scientific space missions such as EMS, where the main purpose of the scalar magnetometer is the calibration of the low AC measurement range of the fluxgate magnetometers. As shown in Figure 5.3, the magnetic field measurement depends on the sensor temperature with less than 7 pT/K. The remaining drift cannot be distinguished from the temperature drifts of the μ-metal can, the coil system or the constant current source which were needed for shielding and for driving the artificial field. The magnetic field measurement was demonstrated for a magnetic flux density of 25 nT (see Figure 5.4) and the dynamic range spans up to a calculated value of 1 mT with identical performance.

The instrument has a mass of 774 g. The measured high power consumptions of 5267 mW in air and 3498 mW in vacuum are caused by the power interface requirements which are defined for the EMS mission. For an identical hardware but with an optimized power interface, the calculated power consumption is 2515 mW in air and 1427 mW in vacuum (see Table 5.1).

Upcoming development and evaluation steps include replacing the magnetic parts of the current sensor unit, characterizing the CDSM sensor location at the observatory with a reference magnetometer and carrying out further accuracy tests. Two CDSM sensor units will be mounted close together for a further test; the sensors should not interfere with each other due to the all optical sensor design. This will give information on the accuracy and reproducibility of the CDSM measurements.

Additionally, a set of qualification tests will be carried out by the end of 2013. For the sensor unit this includes a sine and random vibration test, a Thermal-Vacuum (TV) test in the operating temperature range of $-170°C$ to $+60°C$ and a survival temperature test down to $-196°C$. For the electronics board and the laser unit which includes the laser, the coupler and the mounting frame, a sine and random vibration test and a TV test in the operating temperature range of $-20°C$ to $+50°C$ will be carried out. The noise and accuracy of the instrument will be tested at magnetic flux densities below 100 nT. The instrument will be calibrated at the Conrad Observatory of the Central Institute for Meteorology and Geodynamics in Austria and at the Technische Universität Braunschweig (TUB) in Germany. Furthermore, the sensor unit will undergo electron irradiation tests at Graz University of Technology and at the Physikalisch-Technische Bundesanstalt (PTB) Braunschweig in Germany. These tests will evaluate the readiness of the CDSM instrument for the EMS and in particular for the JUpiter ICy Moon Explorer (JUICE) mission.

List of Figures

1.1 Cross section of CDSM sensor and pictures of implemented components 1

2.1 D_1 spectral line excitation scheme within the hyperfine structure of ^{87}Rb 6
2.2 Dependence of the CPT resonance superpositions on the angle θ . . . 9

3.1 Block diagram to enable frequency modulation spectroscopy 11
3.2 Spectra for frequencies ω_{ref} larger than the probed resonance linewidth 14
3.3 Spectra for frequencies ω_{ref} smaller than the resonance linewidth . . . 15
3.4 Signal flow of the direct digital synthesizer 16

4.1 Block diagram of instrument design 19
4.2 Picture of CDSM prototype equivalent to the EM for the EMS mission 20
4.3 Demonstration of the CPT resonance superposition switching 23
4.4 DDS block diagram to generate a frequency modulated signal 25
4.5 FPGA output structure and equivalent circuit 27
4.6 Schematic of R-2R DAC network with $Q = 12$ and inverting amplifier . 27
4.7 Schematic of R-2R DAC FPGA output compensation 28
4.8 Signal-to-interference ratio of the R-2R DAC 29
4.9 Equivalent circuit of a photodiode 30
4.10 Schematics of a single stage transimpedance amplifier circuit 31
4.11 Schematics of a two-stage photodiode amplification circuit 32
4.12 Schematics of a transimpedance amplifier with feedback 33
4.13 Noise performance of circuit designs which contain two amplifiers . . . 34
4.14 Block diagram of the dual-phase lock-in amplifier 36
4.15 Block diagram of the highpass filter implementation 37
4.16 Bode diagram of the highpass filter for different K_{HP} 38
4.17 Bode diagram of the moving average filter for different $N_{2f_{ref}}$ 40
4.18 Block diagram of the lowpass filter implementation 41
4.19 Bode diagram of the lowpass filter for different K_{LP} 41
4.20 Block diagram of the Zeeman control loop 42
4.21 Block diagram of the Zeeman controller 43

4.22 Bode diagram of the closed Zeeman control loop 44
4.23 Transformation of Cartesian to the spherical coordinate system 45
4.24 Different stages of the PWM pattern generation 49
4.25 Simple laser temperature output structure (option 1) 51
4.26 Advanced laser temperature output structure (option 2) 52
4.27 Laser temperature output structure power consumption and efficiency 53
4.28 Laser temperature measurement circuit with calculated values 55
4.29 Block diagram of the laser temperature control loop 56
4.30 Step response of the laser temperature control path P(s) in air 57
4.31 Bode diagram of the laser temperature control loop 60
4.32 Block diagram of the laser current control loop 61
4.33 Laser frequency spectrum derived by current sweep 61
4.34 Mapping of the actuating variable onto two DAC words 62
4.35 Schematics of laser current generator 64
4.36 Block diagram of the microwave control loop 67
4.37 Frequency spectrum of the hyperfine structure transition 67
4.38 Schematics of the V_{ref} output circuit with calculated values 69
4.39 Sensor temperature heating waveforms 72
4.40 Sensor temperature measurement circuit 73
4.41 Block diagram of the sensor temperature control loop 74
4.42 Step response of the sensor temperature control path 75
4.43 Bode diagram of the sensor temperature control loop 77

5.1 Accuracy of magnetic field measurement 80
5.2 Power spectral density of the magnetic field detection noise 81
5.3 Sensor temperature dependence of the magnetic field measurement . . 82
5.4 Demonstration of the low field performance 82

List of Tables

1.1 Main orbit parameters of the EMS satellite 2
1.2 CDSM interface and performance requirements for the EMS mission . 3

2.1 Zeeman-shifting factors determined by calculation 10

4.1 Parameters of the laser temperature measurement 54
4.2 Parameters of the sensor temperature measurement 73

5.1 Resources measured for EMS and estimated for optimized interface . . 79

List of Abbreviations

A/D	Analogue-to-Digital Converter
ADC	Analogue-to-Digital Converter
CDSM	Coupled Dark State Magnetometer
CMOS	Complementary Metal-Oxide-Semiconductor
CORDIC	COordinate Rotation DIgital Computer
CPT	Coherent Population Trapping
D/A	Digital-to-Analogue Converter
DAC	Digital-to-Analogue Converter
DDS	Direct Digital Synthesis
DSM	Dark State Magnetometer
EM	Engineering Model
EMI	Electro-Magnetic Interferences
EMS	Electro-Magnetic Satellite
ESA	European Space Agency
ESD	Electro-Static Discharge
FIR	Finite Impulse Response
FM	Frequency Modulation
FPGA	Field Programmable Gate Array
FS	Fine Structure
FWHM	Full Width at Half Maximum

H/K	House-Keeping
HFS	Hyperfine Structure
HP	Highpass
IEP	Institute of Experimental Physics, Graz University of Technology
IIR	Infinite Impulse Response
IWF	Space Research Institute, Austrian Academy of Sciences
JUICE	JUpiter ICy Moon Explorer
LEO	Low Earth Orbit
LP	Lowpass
LSB	Least Significant Bit
LUT	Look-Up Table
MOSFET	Metal-Oxide-Semiconductor Field-Effect Transistor
MSB	Most Significant Bits
NIR	Near Infra-Red
NSSC	National Space Science Center, Chinese Academy of Sciences
NTC	Negative Temperature Coefficient
PCB	Printed Circuit Board
PEEK	Polyether Ether Ketone
PIN	Positive Intrinsic Negative
PM	Phase Modulation
PTC	Positive Temperature Coefficient
PWM	Pulse Width Modulation
SFDR	Spurious Free Dynamic Range
SNR	Signal-to-Noise Ratio

TEC	Thermo-Electric Cooling
TP	Totem Pole
TRL	Technology Readiness Level
VCSEL	Vertical-Cavity Surface-Emitting Laser

References

[1] M. H. Acuña, "Space-based magnetometers," *Review of Scientific Instruments*, vol. 73, no. 11, pp. 3717–3736, Nov. 2002.

[2] A. Balogh, "Planetary magnetic field measurements: Missions and instrumentation," *Space Science Reviews*, vol. 152, no. 1-4, pp. 23–97, May 2010.

[3] P. Ripka, Ed., *Magnetic sensors and magnetometers*, ser. Artech House Remote Sensing Library. Artech House Inc, Dec. 2000.

[4] D. Duret, J. Bonzom, M. Bronchier, M. Francès, J.-M. Léger, R. Odru, C. Salvi, T. Thomas, and A. Perret, "Overhauser magnetometer for the Danish Oersted satellite," *IEEE Transactions on Magnetics*, vol. 31, no. 6, pp. 3197–3199, Nov. 1995.

[5] N. Olsen, L. Tøffner-Clausen, T. J. Sabaka, P. Brauer, J. M. G. Merayo, J. L. Jörgensen, J.-M. Léger, O. V. Nielsen, F. Primdahl, and T. Risbo, "Calibration of the Ørsted vector magnetometer," *Earth, Planets and Space*, vol. 55, no. 1, pp. 11–18, Jan. 2003.

[6] M. W. Dunlop, M. K. Dougherty, S. Kellock, and D. J. Southwood, "Operation of the dual magnetometer on Cassini: science performance," *Planetary and Space Science*, vol. 47, no. 10-11, pp. 1389–1405, Oct. 1999.

[7] "Swarm - the Earth's magnetic field and environment explorers," European Space Agency, Technical and Programmatic Annex, 2004.

[8] R. Lammegger, "Method and device for measuring magnetic fields," WIPO, Patent WO/2008/151344, Jun. 2008. [Online]. Available: http://patentscope.wipo.int/search/en/WO2008151344

[9] G. Alzetta, A. Gozzini, L. Moi, and G. Orriols, "An experimental method for the observation of r.f. transitions and laser beat resonances in oriented Na vapor," *Il Nouvo Cimento B*, vol. 36, no. 1, pp. 5–20, Nov. 1976.

[10] E. Arimondo, "Coherent population trapping in laser spectroscopy," *Progress in Optics*, vol. 35, pp. 257–354, Jun. 1996.

[11] G. Orriols, "Nonabsorption resonances by nonlinear coherent effects in a three-level system," *Il Nouvo Cimento B*, vol. 53, no. 1, pp. 1–24, Sep. 1979.

[12] R. Wynands and A. Nagel, "Precision spectroscopy with coherent dark states," *Applied Physics B*, vol. 68, no. 1, pp. 1–25, Jan. 1999.

[13] A. Nagel, L. Graf, A. Naumov, E. Mariotti, V. Biancalana, D. Meschede, and R. Wynands, "Experimental realization of coherent dark-state magnetometers," *Europhysics Letters*, vol. 44, no. 1, pp. 31–36, Oct. 1998.

[14] M. Stähler, S. Knappe, C. Affolderbach, W. Kemp, and R. Wynands, "Picotesla magnetometry with coherent dark states," *Europhysics Letters*, vol. 54, no. 3, pp. 323–328, May 2001.

[15] R. Lammegger, "Coherent Population Trapping - ein Quanteninterferenzeffekt als Basis optischer Magnetometer," PhD thesis, University of Technology, Graz, Austria, Mar. 2006.

[16] R. Wynands, A. Nagel, S. Brandt, D. Meschede, and A. Weis, "Selection rules and line strengths of Zeeman-split dark resonances," *Physical Review A*, vol. 58, no. 1, pp. 196–203, Jul. 1998.

[17] S. Knappe, J. Kitching, L. Hollberg, and R. Wynands, "Temperature dependence of coherent population trapping resonances," *Applied Physics B*, vol. 74, no. 3, pp. 217–222, Mar. 2002.

[18] X. Shen, X. Jia, L. Wang, H. Chen, Y. Wu, S. Yuan, J. Shen, S. Zhao, J. Qian, and J. Ding, "The earthquake-related disturbances in ionosphere and project of the first china seismo-electromagnetic satellite," *Earthquake Science*, vol. 24, no. 6, pp. 639–650, Dec. 2011.

[19] Science Programme Commitee, "Selection of the L1 mission," European Space Agency, Paris, France, ESA/SPC(2012)12, Apr. 2012.

[20] M. O. Scully and M. Fleischhauer, "High-sensitivity magnetometer based on index-enhanced media," *Physical Review Letters*, vol. 69, no. 9, pp. 1360–1363, Aug. 1992.

[21] M. Fleischhauer and M. Scully, "Quantum sensitivity limits of an optical magnetometer based on atomic phase coherence," *Physical Review A*, vol. 49, no. 3, pp. 1973–1986, Mar. 1994.

[22] R. Wynands, "Precision spectroscopy with coherently coupled lasers," Habilitationsschrift, University of Bonn, Germany, Mar. 1998.

[23] S. Knappe, "Dark resonance magnetometers and atomic clocks," PhD thesis, University of Bonn, Germany, Apr. 2001.

[24] C. Affolderbach, M. Stähler, S. Knappe, and R. Wynands, "An all-optical, high-sensitivity magnetic gradiometer," *Applied Physics B*, vol. 75, no. 6-7, pp. 605–612, Nov. 2002.

[25] P. D. D. Schwindt, S. Knappe, V. Shah, J. Kitching, J. Belfi, L.-A. Liew, and J. Moreland, "Chip-scale atomic magnetometer," *Applied Physics Letters*, vol. 85, no. 26, pp. 6409–6411, Dec. 2004.

[26] G. Breit and I. I. Rabi, "Measurement of nuclear spin," *Physical Review*, vol. 38, no. 11, pp. 2082–2083, Dec. 1931.

[27] D. A. Steck, "Rubidium 87 D line data," 2008.

[28] A. Godone, F. Levi, and S. Micalizio, *Coherent population trapping maser*. Turin: CLUT, 2002.

[29] J. Vanier and C. Audoin, *The Quantum Physics of Atomic Frequency Standards*. Bristol, Philadelphia: Adam Hilger, 1989, vol. 1.

[30] A. Pollinger, M. Ellmeier, W. Magnes, C. Hagen, W. Baumjohann, E. Leitgeb, and R. Lammegger, "Enable the inherent omni-directionality of an absolute coupled dark state magnetometer for e.g. scientific space applications," in *Instrumentation and Measurement Technology Conference (I2MTC)*, Graz, Austria, May 2012, pp. 33–36.

[31] S. Knappe, W. Kemp, C. Affolderbach, A. Nagel, and R. Wynands, "Splitting of coherent population-trapping resonances by the nuclear magnetic moment," *Physical Review A*, vol. 61, no. 1, p. 012508, Dec. 1999.

[32] G. C. Bjorklund, M. D. Levenson, W. Lenth, and C. Ortiz, "Frequency modulation (FM) spectroscopy," *Applied Physics B*, vol. 32, no. 3, pp. 145–152, Nov. 1983.

[33] U. Tietze, C. Schenk, and E. Gamm, *Halbleiter-Schaltungstechnik*, 12th ed. Berlin; Heidelberg; New York: Springer, 2002.

[34] J. Tierney, C. Rader, and B. Gold, "A digital frequency synthesizer," *IEEE Transactions on Audio and Electroacoustics*, vol. 19, no. 1, pp. 48–57, Mar. 1971.

[35] "A technical tutorial on digital signal synthesis," Analog Devices, Tutorial, Feb. 1999.

[36] L. Cordesses, "Direct digital synthesis: a tool for periodic wave generation (part 1)," *IEEE Signal Processing Magazine*, vol. 21, no. 4, pp. 50–54, Jul. 2004.

[37] H. T. Nicholas and H. Samueli, "An analysis of the output spectrum of direct digital frequency synthesizers in the presence of phase-accumulator truncation," in *41st Annual Symposium on Frequency Control - 1987*, Philadelphia, USA, May 1987, pp. 495–502.

[38] V. F. Kroupa, V. Cizek, J. Stursa, and H. Svandova, "Spurious signals in direct digital frequency synthesizers due to the phase truncation," *IEEE Transactions on Ultrasonics, Ferroelectrics and Frequency Control*, vol. 47, no. 5, pp. 1166–1172, Sep. 2000.

[39] E. Curticapean and J. Niittylahti, "Exact analysis of spurious signals in direct digital frequency synthesisers due to phase truncation," *Electronics Letters*, vol. 39, no. 6, pp. 499–501, Mar. 2003.

[40] D. H. Guest, "Simplified data-transmission channel measurements," *Hewlett-Packard Journal*, vol. 26, no. 3, pp. 15–24, Nov. 1974.

[41] H. T. Nicholas, H. Samueli, and B. Kim, "The optimization of direct digital frequency synthesizer performance in the presence of finite word length effects," in *Proceedings of the 42nd Annual Frequency Control Symposium*, Baltimore, USA, Jun. 1988, pp. 357–363.

[42] J. A. Crawford, *Frequency synthesizer design handbook.* Artech House, Jun. 1994.

[43] D. Brandon, "DDS design," *EDN*, pp. 71–84, May 2004. [Online]. Available: http://www.edn.com/design/test-and-measurement/4332832/DDS-design

[44] J. E. Volder, "The CORDIC trigonometric computing technique," *IRE Transactions on Electronic Computers*, vol. EC-8, no. 3, pp. 330–334, Sep. 1959.

[45] M. Stitt and W. Meinel, "OPT201 photodiode-amplifier rejects ambient light," Burr-Brown, Application Bulletin 61, Nov. 1993.

[46] M. Ellmeier, "Influence of characteristic parameters on the performance of a coupled dark state magnetometer," Diploma thesis, University of Graz, Austria, Oct. 2011.

[47] "About lock-in amplifiers," Stanford Research Systems, Application Note 3, Jan. 2004.

[48] C. Affolderbach, A. Nagel, S. Knappe, C. Jung, D. Wiedenmann, and R. Wynands, "Nonlinear spectroscopy with a vertical-cavity surface-emitting laser (VCSEL)," *Applied Physics B*, vol. 70, no. 3, pp. 407–413, Mar. 2000.

[49] S. Knappe, M. Stähler, C. Affolderbach, A. V. Taichenachev, V. I. Yudin, and R. Wynands, "Simple parameterization of dark-resonance line shapes," *Applied Physics B*, vol. 76, no. 1, pp. 57–63, Jan. 2003.

[50] H. P. Geering, *Regelungstechnik: Mathematische Grundlagen, Entwurfsmethoden, Beispiele*, 5th ed. Berlin; Heidelberg; New York: Springer, 2001.

[51] W. Demtröder, *Laserspektroskopie: Grundlagen und Techniken*, 5th ed. Berlin; Heidelberg; New York: Springer, Jul. 2007.

[52] "Op amps for everyone," Texas Instruments, Design Reference SLOD006B, Aug. 2002.

Author's Publications

Referred Articles and Conference Proceedings

A. Pollinger, R. Lammegger, W. Magnes, M. Ellmeier, C. Hagen, I. Jernej, W. Baumjohann and E. Leitgeb, "Prototype of a Coupled Dark State Magnetometer," submitted as journal paper to *Measurement, Science and Technology*, Apr. 12, 2013.

> *The paper introduces the measurement principle, the instrument design, the required resources and the performance measurements of the first CDSM prototype.*

A. Pollinger, M. Ellmeier, W. Magnes, C. Hagen, W. Baumjohann, E. Leitgeb, and R. Lammegger, "Enable the inherent omni-directionality of an absolute coupled dark state magnetometer for e.g. scientific space applications," in *Instrumentation and Measurement Technology Conference (I2MTC)*, Graz, Austria, May 2012, pp. 33–36.

> *The paper discusses the technical realization of the CPT resonance switching, investigates the influence of this transition on the magnetic field measurement and proposes a method to detect the angle of the magnetic field direction in relation to the optical axis.*

R. Duffard, K. Kumar, S. Pirrotta, M. Salatti, M. Kubínyi, U. Derz, R. M. G. Armytage, S. Arloth, L. Donati, A. Duricic, J. Flahaut, S. Hempel, A. Pollinger, and S. Poulsen, "A multiple-rendezvous, sample-return mission to two near-Earth asteroids," *Advances in Space Research*, vol. 48, no. 1, pp. 120–132, Jul. 2011.

> *The paper presents the work developed at the 2008 Summer School Alpbach,"Sample return from the Moon, asteroids and comets" organized by the Aeronautics and Space Agency of the Austrian Research Promotion Agency.*

A. Pollinger, W. Magnes, A. Valavanoglou, and H. Ottacher, "Design of a communication and power supply system providing the spaceborne magnetometer front-end ASIC at remote locations," in *6th International Symposium on Communication Systems, Networks and Digital Signal Processing (CSNDSP)*, Graz, Austria, Jul. 2008, pp. 722–725.

The paper investigates future interface options to locate the magnetometer front-end ASIC (MFA) close to the sensor in order to minimize the effort of cabling and to reduce overall weight. The MFA reads out magnetic field sensors based on the fluxgate principle.

Conference Proceedings

A. Pollinger, R. Lammegger, W. Magnes, M. Ellmeier, W. Baumjohann, and L. Windholz, "Control loops for a coupled dark state magnetometer," in *IEEE Sensors 2010*, Kona, USA, Nov. 2010, pp. 779–784.

The paper discusses the first two control loops which are developed for tracking the magnetic field dependent CPT resonances and for avoiding drifts of the carrier frequency of the laser diode. It is the first time that a magnetometer of this type is operated in a control loop and that measurement results are presented.

Oral and Poster Presentations

A. Pollinger, M. Ellmeier, W. Magnes, C. Hagen, W. Baumjohann, E. Leitgeb, and R. Lammegger, "Instrument design of the coupled dark state magnetomter (CDSM)," International Scientific CNRS Fall School 2012 High Sensitivity Magnetometers "Sensors & Applications", Branville, France, Oct. 2012.

M. Ellmeier, R. Lammegger, A. Pollinger, W. Magnes, and L. Windholz, "Measurement principle of the coupled dark state magnetometer (CDSM)," International Scientific CNRS Fall School 2012 High Sensitivity Magnetometers "Sensors & Applications", Branville, France, Oct. 2012.

M. Ellmeier, R. Lammegger, A. Pollinger, W. Magnes, and L. Windholz, "Omnidirectional magnetic field measurement by means of the coupled dark state magnetometer (CDSM)," Jahrestagung Österreichische Physikalische Gesellschaft (ÖPG), Graz, Austria, Sep. 2012.

A. Pollinger, M. Ellmeier, W. Magnes, C. Hagen, W. Baumjohann, E. Leitgeb, and R. Lammegger, "Enable the inherent omni-directionality of an absolute coupled dark state magnetometer for e.g. scientific space applications," Instrumentation and Measurement Technology Conference (I2MTC), Graz, Austria, May 2012.

A. Pollinger, R. Lammegger, W. Magnes, M. Ellmeier, C. Hagen, I. Jernej, and W. Baumjohann, "CDSM roadmap and instrument design for EMS," 4th Magnetometer Workshop, Sigüenza, Spain, Jul. 2011.

A. Pollinger, R. Lammegger, W. Magnes, M. Ellmeier, C. Hagen, I. Jernej, and W. Baumjohann, "CDSM LF electronics and control loops," 4th Magnetometer Workshop, Sigüenza, Spain, Jul. 2011.

M. Ellmeier, R. Lammegger, A. Pollinger, W. Magnes, and L. Windholz, "Investigation on a coupled dark state magnetometer," 43rd Congress of the European Group on Atomic Systems (EGAS), Fribourg, Switzerland, Jun. 2011.

A. Pollinger, R. Lammegger, W. Magnes, M. Ellmeier, W. Baumjohann, and L. Windholz, "Control loops for a coupled dark state magnetometer," IEEE Sensors Conference, Kona, USA, Nov. 2010.

A. Pollinger, R. Lammegger, W. Magnes, M. Ellmeier, W. Baumjohann, and L. Windholz, "CDSM - A new scalar magnetometer," EGU General Assembly 2010, Vienna, Austria, May 2010.

A. Pollinger, R. Lammegger, W. Magnes, M. Ellmeier, W. Baumjohann, M. Volwerk, L. Windholz, and M. Dougherty, "CDSM - A new scalar magnetometer," 3rd instrument workshop for the Europa Jupiter System Mission, European Space Research and Technology Centre (ESTEC) in Noordwijk, the Netherlands, Jan. 2010.

L. Windholz, W. Magnes, A. Pollinger, M. Ellmeier, and R. Lammegger, "A coupled dark state magnetometer," 41st European Group on Atomic Systems Conference, Gdansk, Poland, Jul. 2009.

W. Magnes, A. Pollinger, A. Valavanoglou, and H. Ottacher, "Design of a communication and power supply system providing the spaceborne magnetometer front-end ASIC at remote locations," 6th International Symposium on Communication Systems, Networks and Digital Signal Processing (CSNDSP), Graz, Austria, Jul. 2008.